MICROMAGNETIC STUDY OF PERPENDICULAR MAGNETIC RECORDING MEDIA

A DISSERTATION
SUBMITTED TO THE FACULTY OF THE GRADUATE SCHOOL
OF THE UNIVERSITY OF MINNESOTA
BY

YAN DONG

IN PARTIAL FULFILLMENT OF THE REQUIREMENTS
FOR THE DEGREE OF
DOCTOR OF PHILOSOPHY

RANDALL VICTORA, ADVISOR

JANUARY, 2012

Acknowledgements

First of all, I would like to thank my advisor, Professor Randall Victora, for introducing me to the field of magnetic recording and supervising me to do these exciting projects. This would be impossible without his guidance and encouragement in my scientific pursuit. I would like to thank him for his valuable comments and helpful discussions on my research. His academic insights, profound understanding of magnetic materials and micromagnetic theory always guided me to go deeper and be more active. I learned a lot from him.

I would also like to acknowledge the input and advice from Professor Jian-ping Wang, Beth Stadler and Jack Judy during my work and stay in MINT center.

I am thankful to my dissertation committee members Prof. Jian-ping Wang, Prof. Beth Stadler and Prof. Dan Dahlberg, for their time, help and efforts of serving in my committee.

It has been an enjoyable experience with the past and current members of Professor Victora's group and the MINT center. I would like to thank Xiao Shen, Stephanie Hernandez, Xi Chen, Hweerin Sohn, Eunkyung Cho, Tao Qu, Pin-wei Huang, Sean Morgan, Yao Wang, Yisong Zhang, Nian Ji, Liang Tu, Ying Jing, Todd Klein, Yuanpeng Li, Xiaofeng Yao and many other friends for their valuable discussion and friendly feedback. I enjoyed the time I spent with them.

I would also like to acknowledge Seagate Technology, INSIC EHDR and IDEMA/ASTC for funding and the supercomputing institute of the University of Minnesota for computer time.

Finally, I would like to express my love and thanks to my parents, my grandparents and my boyfriend. Without their love, support and advice, I would have never gone so far.

Dedication

With gratitude to my parents.

Abstract

With increasing areal density in magnetic recording systems, perpendicular recording has successfully replaced longitudinal recording to mitigate the superparamagnetic limit. The extensive theoretical and experimental research associated with perpendicular magnetic recording media has contributed significantly to improving magnetic recording performance. Micromagnetic studies on perpendicular recording media, including aspects of the design of hybrid soft underlayers, media noise properties, inter-grain exchange characterization and ultra-high density bit patterned media recording, are presented in this dissertation.

To improve the writability of recording media, one needs to reduce the head-to-keeper spacing while maintaining a good texture growth for the recording layer. A hybrid soft underlayer, consisting of a thin crystalline soft underlayer stacked above a non-magnetic seed layer and a conventional amorphous soft underlayer, provides an alternative approach for reducing the effective head-to-keeper spacing in perpendicular recording. Micromagnetic simulations indicate that the media using a hybrid soft underlayer helps enhance the effective field and the field gradient in comparison with conventional media that uses only an amorphous soft underlayer. The hybrid soft underlayer can support a thicker non-magnetic seed layer yet achieve an equivalent or better effective field and field gradient.

A noise plateau for intermediate recording densities is observed for a recording layer of typical magnetization. Medium noise characteristics and transition jitter in perpendicular magnetic recording are explored using micromagnetic simulation. The plateau is replaced by a normal linear dependence of noise on recording density for a low magnetization recording layer. We show analytically that a source of the plateau is similar to that producing the Non-Linear-Transition-Shift of signal. In particular, magnetostatic effects are predicted to produce positive correlation of jitter and thus negative correlation of noise at the densities associated with the plateau.

One focus for developing perpendicular recording media is on how to extract intergranular exchange coupling and intrinsic anisotropy field dispersion. A

micromagnetic numerical technique is developed to effectively separate the effects of intergranular exchange coupling and anisotropy dispersion by finding their correlation to differentiated M-H curves with different initial magnetization states, even in the presence of thermal fluctuation. The validity of this method is investigated with a series of intergranular exchange couplings and anisotropy dispersions for different media thickness. This characterization method allows for an experimental measurement employing a vibrating sample magnetometer (VSM).

Bit patterned media have been suggested to extend areal density beyond 1 Tbit/in^2. The feasibility of 4 Tit/in^2 bit patterned recording is determined by aspects of write head design and media fabrication, and is estimated by the bit error rate. Micromagnetic specifications including 2.3:1 BAR bit patterned exchange coupled composite media, trailing shield, and side shields are proposed to meet the requirement of 3×10^{-4} bit error rate, 4 nm fly height, 5% switching field distribution, 5% timing and 5% jitter errors for 4 Tbit/in^2 bit patterned recording. Demagnetizing field distribution is examined by studying the shielding effect of the side shields on the stray field from the neighboring dots. For recording self-assembled bit-patterned media, the head design writes two staggered tracks in a single pass and has maximum perpendicular field gradients of 580 Oe/nm along the down-track direction and 476 Oe/nm along the cross-track direction. The geometry demanded by self-assembly reduces recording density to 2.9 Tbits/in^2.

Table of Contents

List of Figures

List of Tables

Chapter 1 Introduction

1. 1 Overview of data storage technology

The evolutionary path of magnetic data storage has experienced substantial progress in recording areal density and data rate ever since its invention. In 1956, IBM built the first commercially available hard disk drive which was leased as part of the random access method of accounting and control (RAMAC) system. It had an areal density of 2 kbit/in^2, a data rate of 70 kbit/s, and stored 5 Mbytes of information on fifty 24-in disks. The material used in the magnetic disks was aluminum coated with particulate γ–iron oxide in an epoxy base. The NRZI (non return to zero) code and amplitude detector combination was utilized for the signal process method. The invention of the RAMAC system marked the beginning of a long history of new technologies and applications for providing the nonvolatile and inexpensive data storage. Meanwhile, research efforts were underway for the development of new magnetic recording physics, new magnetic materials, advanced signal process methods and head-media interface techniques, which led to a steady increase in storage density. As of 2010, the commercial hard disk drive has an areal density above 500 Gbit/in^2, a burst data rate of 3.0 Gbits/s, and stored up to 3 Tbytes of information on five 3.5-in disks. This represents a radical increase in the disk capacity by a factor of about 600,000. Fig. 1.1 shows how areal density has increased from when magnetic storage was first developed (1956 RAMAC) through the present time 2010 [1.1]. The overall growth rate has been around 41% per annum from 1956 to 2010. Thanks to new technologies such as Giant magneto-resistive head (GMR head) and perpendicular recording technology, the areal density achieved for products grew at the rate of 91% per annum from 1995 to 2001. During 2000's, the increase in areal density tended to slow down to 37% per annum but the progress is still substantial.

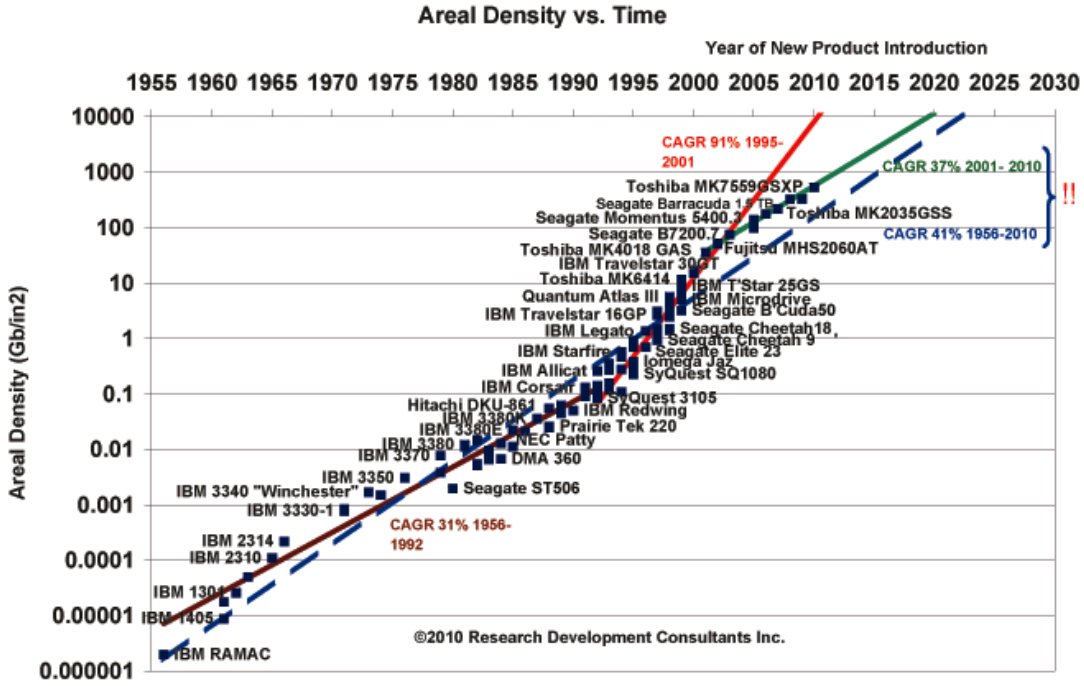

Figure 1. 1 Evolution of areal density in magnetic hard disk drive industry (source: http://rondennison.com/services.htm)

Fig. 1.2 shows all the basic components of a modern hard disk drive [1.2]. The hard disk uses round, flat platters to store information. The platters are coated with special magnetic layers on both sides. All the platters are held by a hole cut in the center and stacked into a spindle. The platters are spun at a high speed of several thousand RPM by a spindle motor. Every platter has one head assembly on each side. The head assembly has the read and write heads integrated together. The head assembly is mounted on a slider, aerodynamically floating over the platter. The head is held in close proximity (spacing between head and media is as small as 5 nm) with the recording layer through a self-pressuring air bearing mechanism. The sliders are mounted into arms, all of which are connected to a single assembly (also known as head stack assembly). The position of the head over the desired track is controlled by another

motor known as an actuator. Hard drives come in different sizes or form factors and the most popular sizes are 3.5-inch and 2.5-inch diameters.

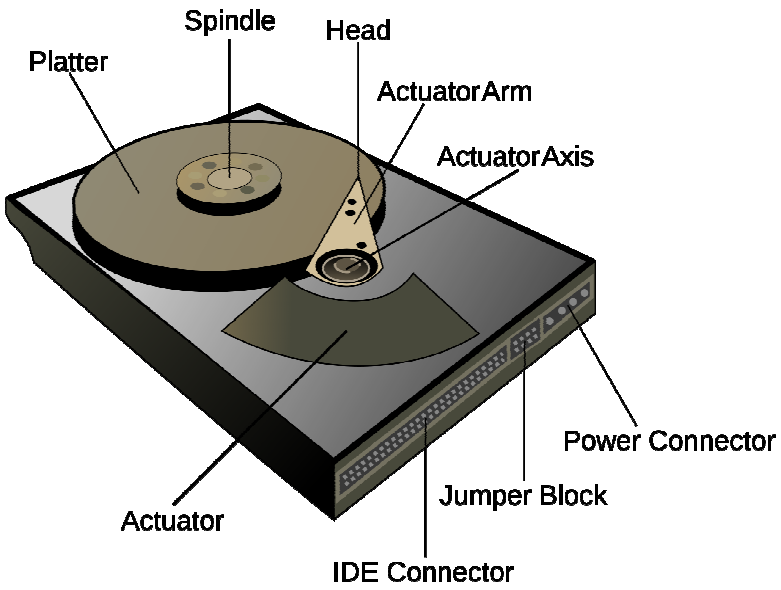

Figure 1. 2 The basic component of hard disk drive (source: http://en.wikipedia.org/wiki/hard_disk_drive)

The hard disk drive system can be classified into longitudinal and perpendicular recording. By the end of 1990s, all magnetic recording devices used longitudinal recording where the magnetization prefers to lie in the plane of recording medium. As early as 2000, however, longitudinal recording technology became harder and crossed its recording density limit owing to the onset of superparamagnetism. The bottleneck for longitudinal recording technology at higher density comes primarily from finding the balance among thermal stability, signal-to-noise ratio and availability of write materials. No areal density demonstration was made beyond the 130 Gbits/in^2 for longitudinal recording [1.3].

Perpendicular recording, where the magnetic anisotropy is aligned perpendicular to the medium plane, has been successfully introduced to the current conventional magnetic recording applications [1.4] and the future ultra-high density recording technologies [1.8]-[1.12]. Perpendicular recording helped achieve areal density of over 500 Gbits/in^2 on the current commercial hard disk drive. It is expected that the areal

density can be extended to 1 Tbits/in^2 for perpendicular recording [1.13][1.14]. To achieve ultra-high density recording beyond 1 Tbits/in^2, several advanced magnetic recording structures, such as bit-patterned media recording [1.8][1.15], head-assisted magnetic recording (HAMR) [1.16][1.17], two-dimensional magnetic recording (TDMR) and shingled recording [1.12][1.18], etc., have been proposed as candidates. While these advanced methods would also make use of perpendicular recording, significant changes in media fabrication and head designs will be expected.

1. 2 The challenges of ultra-high density recording

To achieve the highest areal densities, it is necessary to use a magnetic recording configuration capable of writing very small grains and a signal processing system capable of recovering the data reliably from each bit that is recorded on these small grains. Simple scaling argument shows that thermal stability of the medium will become the primary physical concern at very high areal densities. Thermal stability indicates the lower limit of the grain size in the recording system. Grains' sizes smaller than this limit are unstable and likely to switch the magnetization within a shorter time than the desired time-scale for data storage.

1.2.1 Superparamagnetic effect

In general, the change of magnetization in a hysteresis loop consists of reversible and irreversible portions, the latter occurring as the energy barrier ΔE in some part of the particle configuration is overcome. The crossing of an energy barrier can be substantially aided by thermal energy. To examine this thermal induced phenomenon, we can consider an assembly of weakly interacting, uniaxial and single-domain particles, each with an anisotropy energy density of $E= K_u \sin^2\theta$, where K_u is the anisotropy constant of the material and θ is the angle between $\mathbf{M}_s$ and the easy axis. The magnetization of the particle is assumed to be a coherently rotating vector with magnitude of $\mathbf{M_s}$. It is easily shown that for fields below the anisotropy field H_k

$=2K_u/M_s$, there are two energy minima at $\theta=0, \pi$ with energy densities $E= \pm HM$ and two energy maxima with $\theta=\cos^{-1}(HM/2K_u)$ with energy densities $E= K_u[1+(HM/2K_u)^2]$. Therefore, the energy barrier which prevents the particle switching from its local minima has the magnitude $\Delta E= K_u V [1- (H/H_k)^2]$ where V is the volume of the particle. It is worth noting that if the volume of the single particles V becomes small enough, $K_u V$ will also become so small that the thermal energy fluctuation could overcome anisotropy forces and spontaneously reverse the magnetization from one easy axis to another, even in the absence of an applied field. The term superparamagentism is used to describe the magnetic behavior of such particles.

The energy barrier that prevents the magnetization of a single grain from flipping via thermal agitation (or superparamagentism) is proportional to its anisotropy energy, $K_u V$. In the recording system, most of the six orders of magnitude in areal density increment have been achieved by scaling the recording process, which implies that all the relevant physical dimensions (bit size, head geometry, magnetic fly height, media thickness, etc.) have been reduced by the same linear scaling factor. Furthermore, increasing to higher areal density while maintaining the accepted SNR requires reducing the grain size and grain size distribution. As the areal density further increases, however, the continued scaling to a smaller bit and grain size may prompt spontaneous magnetization reversal via thermal agitation when the energy barrier per single grain $K_u V$ starts competing with the thermal energy $k_B T$.

Grains in real recording thin film experience magnetostatics forces and a small amount of exchange coupling from their neighboring grains. In addition, different bit sizes will have different effects. Essentially, exchange can counter a portion of the magnetostatic field and prevent the thermal decay of a grain at the bit center. The energy barrier is approximately modified as [1.14]:

$$\Delta \mathrm{E} = \frac{1}{2} \times H_c M_s V \left(1 - 0.1 \times \frac{4\pi M_s}{H_c} \right)^2 = k_B T \ln\left(2 f \tau\right) \tag{1}$$

where k_B is the Boltzmann constant, f (attempting frequency) $=10^{11}$ or 10^{11} Hz for today's media and τ is the time scale for the magnetization reversal to occur.

To minimize the grain size, it is very important to increase the anisotropy energy density K_u so that thermal stability is maintained. However, increasing K_u generally goes along with an increase in anisotropy field H_k and higher magnetic field is required to switch the magnetization. It is well known that the write field produced by a pole head with soft underlayer is essentially limited by the magnetic moment of head, because the highest saturation moment B_s ($=4\pi M_s$) for the head material is around 2.4 Tesla. Such disadvantageous writability therefore constrains the selection of high crystalline anisotropy energy and small volume of the grains. With the increase in areal density, a novel head design is needed to have smaller dimensions, yet capable of generating higher recording field. The optimized writer design is proposed for 10 nm thick exchange coupled composite media recording at 1.0 Tbit/in^2. The head design has field gradient peak at 310 Oe/nm where the effective field is 9900 Oe. [1.14]. So, the media coercivity is 9.9 kOe, and the grain size is chosen as 6.1 nm using the 10 years storage at room temperature. Because of the thermal stability criterion, the maximum attainable H_k limits the minimum grain size and thus the highest achievable areal density.

1.2.2 Signal-to-noise ratio and other engineering factors

The reduction of noise in recording system is necessary to achieve higher areal densities. The signal to medium noise, adopting the grain-countering method [1.19], is approximately given by the number of grain in a bit: $SNR_{media} \sim V_{bt}/V_g$, where V_{bt} is the bit volume and V_g is the grain volume. It is worth noting that a small number of grains per bit will produce bad signal to medium noise performance so that the system will greatly rely on the read head sensitivity and the signal processing.

A more significant concern about the noise limited recording performance at ultra-high density is the magnetic fluctuation arising from the recording medium itself. Variable physical and material features of the medium create irregularities in the

magnetization patterns that ultimately transfer into noise on the signal when it is read by the readback head. Medium noise, which strongly depends on the local granular structure of the medium [1.20][1.21], is one of the crucial impediments to obtaining high areal density. Medium noise can be considered a statistically random fluctuation associated with the random component of the magnetization pattern recorded on the medium as caused by a spatially random property of the medium [1.22]. Transition noise refers to the medium noise concentrated at the center of transitions. As recording density increases, transition noise becomes more dominant since the reduction in bit size reduces the area of low noise region. Another medium noise source is the modulation noise which arises from the fluctuations of medium magnetization or flux level directly resulting from the granularity of the medium itself [1.22]. The magnetic irregularity of the medium is caused by, for example, distribution in magnetic grain sizes, grain boundaries, intergranular exchange coupling, intrinsic switching field, thermal fluctuations, etc.. The challenge is to characterize, understand and control most of them in order to recover the desired signals.

In addition to these physical effects, there are a number of practical engineering factors that must be considered: tolerance to the head geometry, reliability of the head-media interface, writing synchronization and electronic channel noise.

1. 3 Basics of perpendicular magnetic recording

There is a general agreement that perpendicular recording is an option to maintain the balance among the proper signal-to-noise ratio, thermal stability and writability and allows continued advances in recording density.

Demagnetizing fields are experienced in any magnetic recording scheme and are expressed as $\mathbf{H}_d = -\mathbf{N}\bullet\mathbf{M}$, where **N** is the demagnetization tensor and **M** is the magnetization vector. N depends on the shape and the direction of the magnet. It is understood that the demagnetizing field is stronger when the magnetic charges are closer. In longitudinal recording, the charged domain walls that form between the bits produces large magnetostatic fields that destabilize the magnetization towards undesired

directions. Increasing the medium thickness is one alternative to increase thermal stability. However, this unfavorable magnetostatic field will become larger at transitions and again reduce thermal stability. Demagnetizing field is therefore found to broaden transitions, cause transition jitter and non-linear transition shift, deteriorate the signal-to-noise ratio and generally inhibit higher recording densities.

Figure 1.3 shows the basic diagrams of perpendicular and longitudinal recording, contrasting how the recording media, the write head and the read head are configured for these two recording systems. Unlike in longitudinal recording, the either up or down magnetization of each bit produces magnetostatic fields that stabilize the recorded magnetization, thus favoring sharp transitions. Furthermore, thicker media and higher recording density exhibit more favorable magnetostatics and thus provide more thermal stability. Edge writing is well defined and erase bands becomes small which is important at a low bit aspect ratio. Another important aspect is the strong uniaxial orientation of the media to generate higher signals and signal-to-noise ratio. In general, to achieve lower noise recording performance, it is necessary to make the grains in the recording layer as small and uniform in size, and magnetically decoupled from each other, as possible.

The unique and the key feature found in perpendicular recording is the utilization of a single pole head and a medium comprised of a recording layer and a soft underlayer (the so-called double-layer perpendicular recording media). The soft underlayer offers a magnetic image of the head which can ideally double the head field. The magnetic flux is efficiently concentrated towards the media in the presence of the soft underlayer located underneath the recording layer. The head fields and field gradients can be well maintained along the depth of the medium. Higher field allows the use of media with not only higher crystalline anisotropy energy, but also larger media thickness. Both of them can generate larger thermal energy density in the media at high recording density, which benefits thermal stability. The presence of a soft underlayer also strengthens the readback signals (only at low density) and helps to decrease the adjacent track interference.

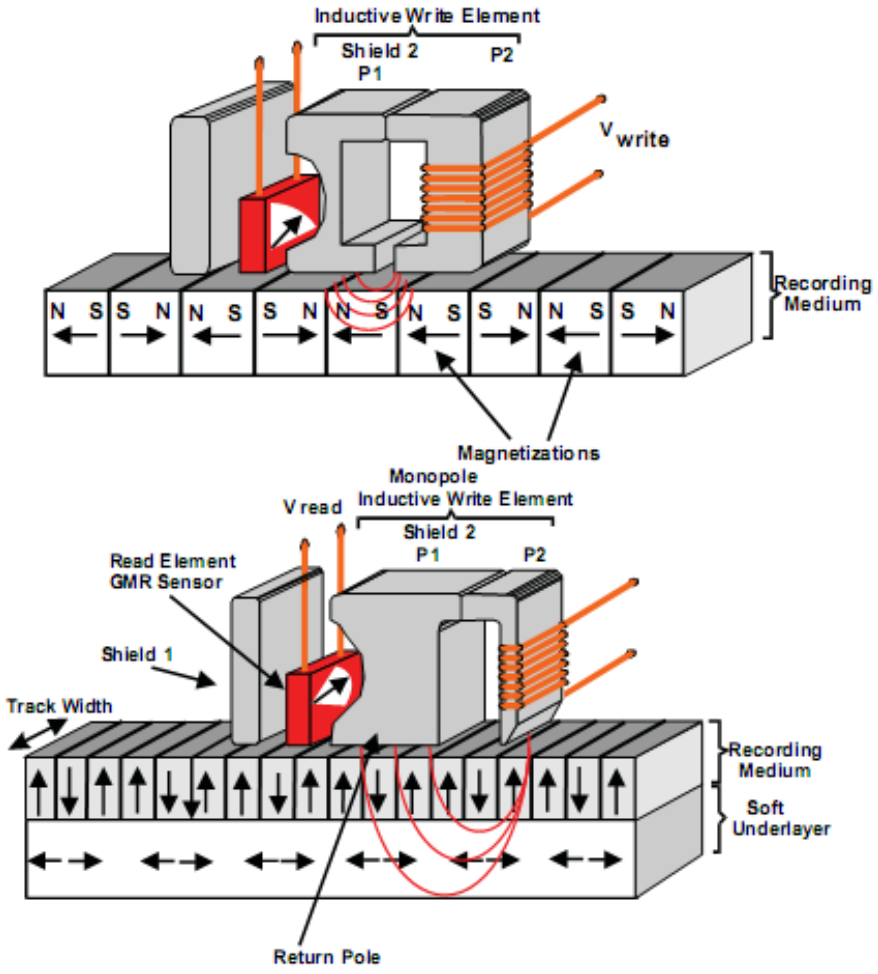

Figure 1. 3 Longitudinal recording diagram (top) and perpendicular recording diagram (bottom). (Courtesy of Hitachi Global Storage Technologies)

1.3.1 Perpendicular magnetic recording media

The promise of perpendicular media can only be realized if it meets several stringent requirements in terms of its macromagnetic properties, such as high coercivity (H_c), perfect remanence magnetization (M_r) or unit squareness ($S=M_r/M_s$) as well as micromagnetic properties, such as small and uniform grain size, well isolated fine granular structures, and sufficiently small head to keeper spacing (HKS).

The basic requirement for thin film recording media is to achieve high coercivity to insure a sharp transition with low noise, while at the same time maintaining adequate

signal strength, proportional to the remanence-thickness product $M_r\delta$. In thin film media, the anisotropy for the high coercivity relies on intrinsic crystalline anisotropy. Single domain particles are required to eliminate the domain walls, which lowers coercivity. Early perpendicular recording media were mainly RF sputtered Co-Cr based alloys. In the alloy films, cobalt's large magnetocrystalline uniaxial anisotropy energy is utilized. With a proper process and the addition of different elements, hexagonal-close-packed (hcp) perpendicular oriented columnar structures can be achieved. Clearly, in perpendicular recording media, the crystalline anisotropy energy must be large enough to surpass the demagnetization energy. Defining the perpendicular magnetic anisotropy energy density as $K_\perp$ and crystalline anisotropy energy density as K_u, $K_\perp=K_u-2\pi M_s^2$ should always be positive. To satisfy this requirement, other metals have to be added to Co to reduce the volume average M_s. Chromium was first tried as an additive [1.23]. Other addition elements such as Mo, W, Ti, V, Mn were also evaluated [1.24]. It was found that the addition of Cr causes high orientation of the c-axis to film normal, which largely improve the perpendicular crystalline anisotropy, and therefore the anisotropy field $H_k(=2K_u/M_s)$. There is a complex interplay between the thin-film processing conditions, microstructures and magnetic properties for RF-sputtered Co-Cr. Increasing the magnetization by increasing the Co/Cr ratio leads to more domain walls and hence lowers the coercivity. Increasing the film thickness results in larger, multi-domain particles, also lowering the coercivity. Optimal coercivity is therefore obtained by choosing the proper ratio of Co/Cr ratio and film thickness so that single-domain particles result with coherent rotation as the dominant magnetization process.

The disadvantage of Co-Cr based alloys is the lower perpendicular crystalline anisotropy since Co by itself, provides much too low coercivity required for today's recording densities. An example hysteresis loop for the CoCr perpendicular alloys [1.25] in Fig. 1.4 clearly shows the low M_r and lower H_c. The relatively strong demagnetization field ($4\pi M_s$) produces a positive nucleation field that is seen in the first quadrant of the hysteresis loop. The shape of the hysteresis loop indicates that the reversed domains appear in the media even when there is a positive applied field. The alloys will have larger media noise and may be thermally unstable.

By forming alloys with large diameter transition elements such as Pt, Ta, Ir and Sm, coercivity values can be increased. It is also considered that the addition of SiO_2 or other oxide is very effective to realize well isolated fine granular structure without disturbing the epitaxial growth of CoPtCr grains on a Ru interlayer. Fig. 1.5 shows the hysteresis loop of 12-nm thick CoCrPt-SiO_2 medium. A typical sheared loop for a perpendicular medium is observed and M_r/M_s of 0.93 is realized. The perpendicular anisotropy after subtracting the demagnetization energy $2\pi M_s^2$ is about 4×10^6 erg/cm^3 and the high coercivity of about 4.2 kOe is obtained [1.26]. The CoCrPt-SiO_2 medium shows much higher readback signal, recording resolution and signal to noise ratio than those of CoCrPtB medium, especially in the high density region larger than 200 kFCI. The advantageous recording performance of CoCrPt-SiO_2 medium is likely owing to a combination of squareness, coercivity and grain size.

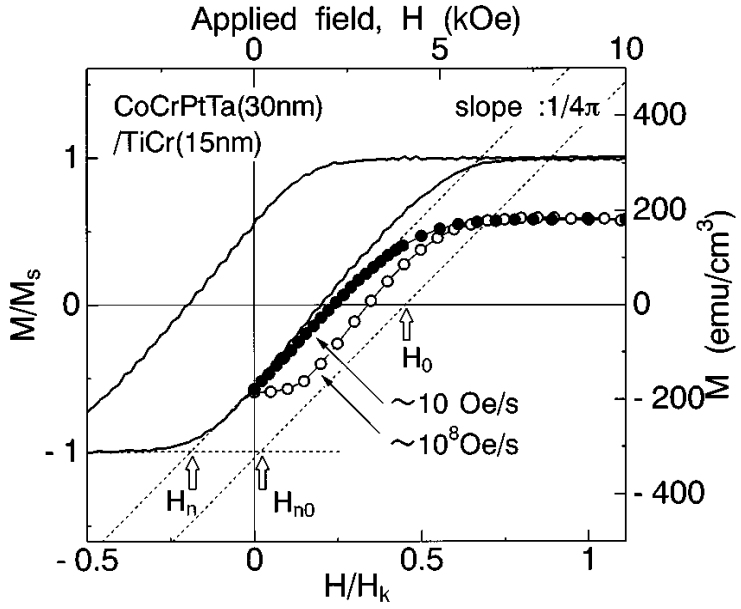

Figure 1. 4 Typical remanence curve (the solid line) of CoCr alloy perpendicular media with positive nucleation field and lower remanent moment. [1.25]

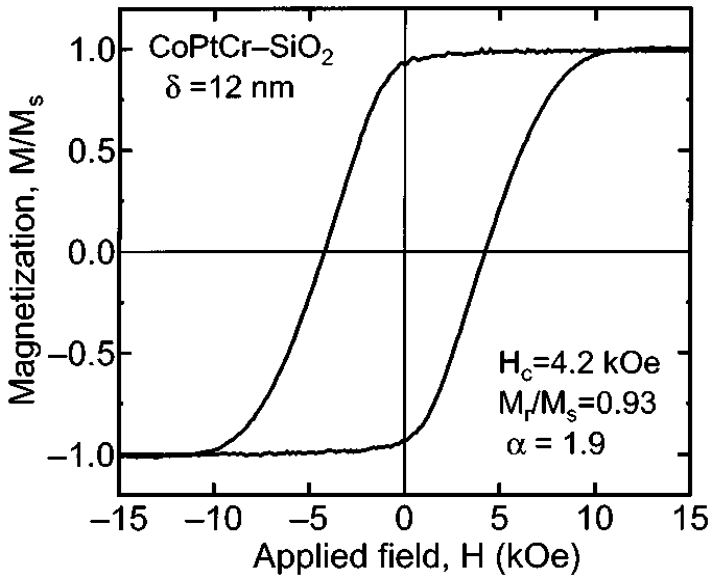

Figure 1. 5 Hysteresis loop of 12-nm-thick CoCrPt-SiO_2 medium. [1.26]

High anisotropy materials such as FePt, CoPd and CoPt alloys were developed as candidates of perpendicular recording media for high-density recording [1.27][1.28]. Previous work shows that the well-separated crystallites and the well-ordered fct structure were achieved in CoPt thin films. Coercivity can be enhanced as high as 37 kOe. However, the application of such thin film will be constrained by (1) limited writability of currently available write heads; (2) High deposition or annealing temperature (~750 °C); (3) typically large grain size that will cause large media noise and thus degrade SNR.

Smaller grain size is necessary to insure adequate signal to noise ratio and good bit error rate performance in perpendicular recording media. The grain size decreases with the addition of more SiO_2 or oxygen. In CoCrPt-oxide based medium, for example, oxygen doping in the intermediate layer such as Ru has helped in significantly reducing the grain size. A grain pitch (center-to-center distance between the grains including the grain boundary) of 6.5 nm has been reported in CoCrPt:SiO_2 media with RuCr:oxide intermediate layer [1.29].

The final requirement for good recording performance is the small head-to-keeper spacing, i.e., the distance between the air bearing surface to the soft underlayer. The

magnetic spacing is required to be small in order to reduce the spacing loss. Writability can be greatly enhanced by reducing the “effective magnetic spacing” in the perpendicular recording multilayer. For example, reducing HKS from 45 nm to 35 nm can reduce the pulse width by 20% and enhance the head field from 11.0 kOe to 13.9 kOe [1.30]. Reducing the effective magnetic spacing requires the seed layer to be only a few nanometers while still maintaining small c-axis dispersion and small and exchange-decoupled grains.

Fig. 1.6 shows the different functional layers of a typical double-layered perpendicular recording medium. In practical designs, there may be more than one layer involved for every function. For example, the soft underlayer may be composed of many layers or it may be an antiferromagnetically coupled soft underlayer [1.31]. Similarly, the non magnetic seed layer may consist of many layers including an initial Ta layer and Ru seed layer [1.32]. Current design of perpendicular media involve the use of an amorphous soft underlayer, non magnetic seed layer about 15 nm to 20 nm thick and recording layer about 15 nm thick. Typically, non magnetic seed layer are used to decouple the soft underlayer and recording layer and are sometimes called exchange-breaking layers. In addition, the seed layer is expected to provide a template for a good perpendicular c-axis orientation and to achieve good grain isolation of the recording layer. For perpendicular media with Co-based recording layers, it is essential to obtain grains with a Co [0002] orientation perpendicular to the film plane. Therefore, the seed layer should have the fcc (111) or hcp (002) texture. Usually, another seed layer (Ta) is deposited below the intermediate layer to enhance a preferred growth direction.

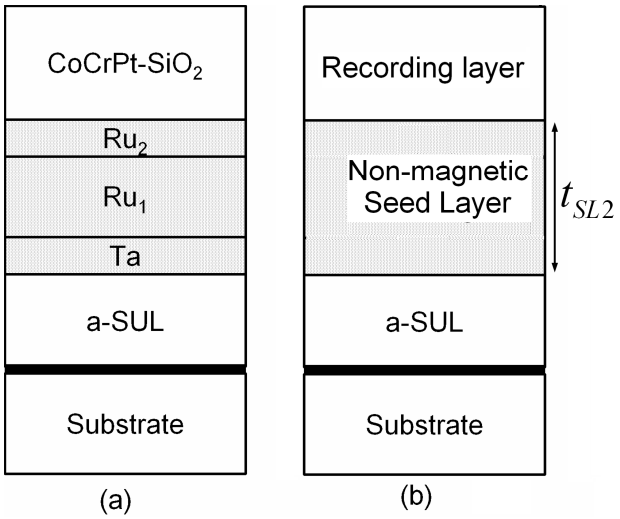

Figure 1. 6 In conventional media (a) and (b), a non-magnetic seed layer of 15- 20 nm decouples the amorphous soft underlayer and the recording layer, and provides a template for inducing a good c-axis orientation and grain isolation in the recording layer.

The presence of a soft underlayer provides a significant advantage for perpendicular recording technology. With a soft underlayer and a single pole head, higher writing fields can be achieved. However, the fact that the soft underlayer is too thick compared to the recording layer and is also made of materials with a larger magnetization than that of the recording layer will lead to a noise problem from the soft underlayer. One major cause of noise from the soft underlayer is called spike noise due to the presence of domain walls [1.33]. If the domain walls formed in the soft underlayer are pinned in some spots, it would be possible to mark the corresponding sections in the recording layer and be removed by the signal processing. However, the domains can move from one place to another, which becomes a serious concern. One approach to reduce the spike noise is to use new materials that can show fewer domains and hence a lower noise. It has been observed that [1.34] the amorphous material CoTaZr exhibits low noise property and is one of the candidates for soft underlayer. Another approach is to do laminations of soft underlayer such as using FeAlSi/C multilayers [1.35]. In addition to the new materials and lamination of soft underlayer, one design involves using an in-plane hard magnetic layer such as SmCo beneath a soft CoZeNb soft underlayer to induce cross track orientation [1.36]. It is observed that the

recording medium with SmCo layer showed lower noise due to the domain wall pinning effect. Such pinning of the soft underlayer can also be achieved by using antiferromagnetic layers, such as IrMn, FeMn and NiMn [1.37].

1.3.2 Magnetic write head

The criteria for a perpendicular write head include high peak field, high field gradient, low adjacent track erasure field, low return pole field and low remnant field.

As previously illustrated, a single pole perpendicular magnetic recording head combined with a soft underlayer offers a strong perpendicular write field while the longitudinal component is greatly reduced. Rather than generating the head by the gap in the ring head, the field for a perpendicular head is generated by the surface of the pole tip and concentrated along the medium depth. The presence of the soft underlayer is very important as it ideally doubles the perpendicular field due to the image effects. Using the 3D micromagnetic simulation, a tapered neck single-pole head design gives a maximum write field of 0.8•Bs (Bs: saturation flux density) for parameters corresponding to 200 Gbits/in^2. Utilizing the overwrite criterion of How=Hc+4πMs for perpendicular yields a maximum anisotropy field of approximately 0.63•Bs [1.38]. Such limitation puts constraint on the coercivity of the media so that improvement in the design of the recording head is necessary to generate a greater field than the limited value reported above.

The single-pole head is modified by replacing a trailing shield spaced close to the trailing edge of the tip where the bit is recorded, as in Fig. 1.7. The trailing shield head has intricate controls on the shield thickness, tapered angle and the gap between the trailing shield and the mail pole to tailor the field strength and field gradient, which indicate optimizing the field gradient without substantially degrading the field strength. The enhanced field gradient shows rapid decay in field strength as the head moves down track so that much sharper transitions are written. As a result, a better bit error rate performance and a better recording reliability can be delivered.

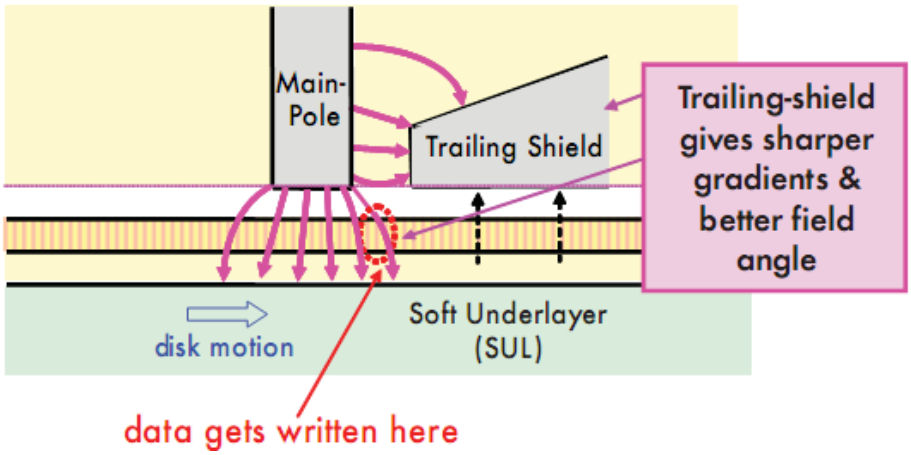

Figure 1. 7 Cross track view of a trailing-shield head. A thin magnetic shield is placed in the proximity of the trailing edge of the writing pole.

As shown in Fig. 1.3, the field in the return pole should be low to make sure it does not cause any undesired erasure. The energy barrier of the thermal assisted magnetic reversal is very sensitive to the presence of this erasure field since it can induce the side track erasure if the head passes the same location for significant amount of time.

As the areal density decreases, the side track width and the bit aspect ratio decrease. Obtaining low adjacent track erasure field is a very challenging design problem. Even if the resulting adjacent track erasure field is far below the nucleation field of the medium, significant field strength could make the grains thermally unstable and cause partial or complete erasure after experiencing many passes by the head.

After the coil current is switched off, it usually takes time for the writer to relax back to its remnant state. During this relaxation process, the head could be locked in a meta-stable state in which the fields from the write pole are high enough to partially or completely erasure the previously written data. This is called erasure after write [1.39] which is different from thermally assisted reversal in adjacent track erasure. It is very important that the erasure after write does not happen during the life of the hard drive.

An efficient write head design should also involve several important considerations unique for perpendicular recording. They are skew effect, neighborhood induced transition shift (NITS) and stray field sensitivity.

Fig. 1.8 shows that the corners of a rectangular pole will protrudes over the edge of the track and write a wide track or erase the neighboring tracks when the head is operating at a skew angle. The skew angles can be as high as 20˚. The head can be formed into a narrow trapezoidal shape with a well-controlled bevel angle to contain the side wall writing and essentially prevent the field from erasing the data in neighboring tracks.

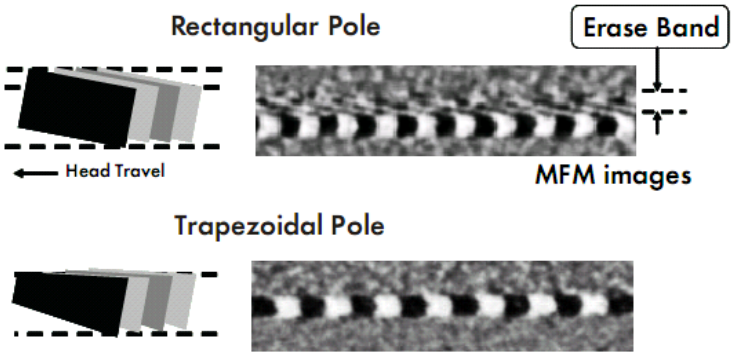

Figure 1. 8 Trapezoidal pole shape in a perpendicular magnetic write head to avoid data erasure in neighboring tracks when the head is operated at a skew angle.

The write pole tip is sensitive to the stray field from adjacent tracks. This field can change the writability by either adding or subtracting from the write field generated from the head tip surface and induce nonlinear transition shift. Since the neighborhood induced transition shift is the results of direct coupling of the flux from adjacent tracks or indirect coupling from the soft underlayer and the return pole, this problem can be dealt with by shielding the head.

1.3.3 Magnetic read head

In 1988, the giant magnetoresistive effect was discovered in ultrathin Fe/Cr multilayers, consisting of alternate layers of a magnetic metal separated by layers of a

non-magnetic metal [1.40]. This structure exhibits a large change in resistance when switched from the low resistance state where the FM layers are parallel to each other to a high resistance state where the layers are antiparallel. In the application of magnetic readback by an MR sensor, the recorded magnetization on the medium applies magnetic applied field to the MR sensor element, and thus causes the change of orientation of local moment in the element. The magnetoresistive heads sense the magnetic flux, not the time rate change of flux. Head sensitivity is therefore independent of the linear speed of the recorded data.

The shielded longitudinal read head works well for a perpendicular read head with minor modifications. However, the wave shape is different. A Hilbert transformation will transform an ideal perpendicular waveform to longitudinal waveform and one direct observation is that the perpendicular read back waveform is similar to the integral of the longitudinal waveform. Therefore the perpendicular readback signal tends to have a large low frequency or DC component in the flux, especially for large bit spacing. This means the free layer can experience the maximum rotation between transitions if the bit length is long. The main effect of the read head switching from longitudinal to perpendicular is a change in the flux the head sees.

There are two types of architectures of potential use in read head geometry, current in plane (CIP) and current perpendicular to the plane (CPP) as shown in Figure 1.9. The GMR sensor, as shown in Fig. 1.10, consists of many layers. In the bottom spin valve, there is a seed layer, an antiferromagnetic (AF) pinning layer that holds the pinned magnetization through exchange coupling with the pinning layer which has no net moment. Between the pinned layer and the free layer is a thin spacer of Cu. The free layer is free to rotate under an applied field.

The sensing structures described above are placed between two soft magnetic layers called shields. As shown in Fig. 1.11, these shields prevent the sensor from absorbing the flux from bits both down track and up track and limit the flux flowing back to bits immediately under the device. The sensor must be insulated from the shields.

These heads require longitudinal stabilization to keep the magnetization in these devices more coherent and to prevent breaking up into smaller domains. Insufficient stabilization bias field will cause unstable heads in which the output voltage can fluctuate as the magnetic state of the sensor changes. The longitudinal bias is provided by attaching a permanent magnetic (PM)/lead structure placed adjacent to the sides of the GMR sensor. The PM is magnetized in a direction across the track and combined with a lead structure to bring the sense current to the device. The change in resistance is then typically read out as a change in voltage with a constant sense current.

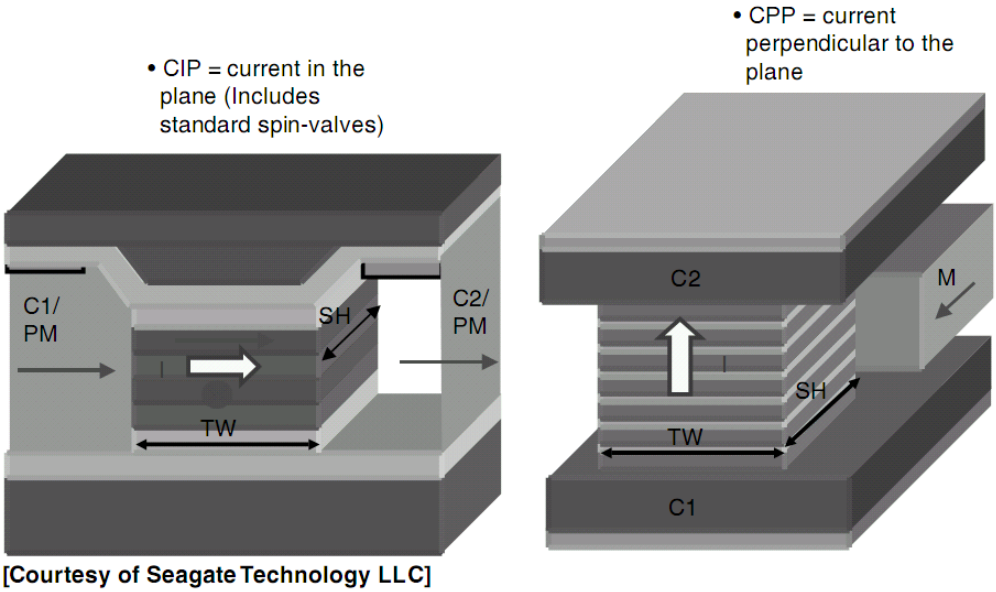

Figure 1. 9 ABS views of CIP and CPP sensor.

The concept of a head architecture using the shields as leads on the top and bottom of a sensor in the CPP mode was first proposed in 1995 [1.42]. Several main CPP designs are under development at present to replace the CIP spin valves. There are the CPP spin valve, the magnetic tunnel junction (MTJ) and the CPP-multilayer. The MTJ uses the tunneling of polarized electrons between the two layers to create the magnetoresistance.

The MTJ device can be made by sandwiching a thin insulating layer of alumina between two ferromagnetic metal (FM) layers, such as CoFe, one of which is pinned as shown in Fig. 1.11. Electrons can tunnel through the thin (<1 nm) barrier if a bias

voltage is applied between the two metal electrodes. Since the tunneling current is spin polarized, it depends on the relative orientation of magnetization of the two FM layer, giving rise to tunneling magnetoresistance (TMR) which is typically defined as $(R_{AP}-R_P)/R_P$, where R_{AP} and R_P are the resistances for anti-parallel (AP) and parallel (P) alignment of the magnetic moments, respectively [1.43][1.44]. Note that TMR and tunneling spin polarization (TSP) are related in Julliere's formula [1.43], TMR= $2P_T^1P_T^2(1- P_T^1P_T^2)$, where P_T^1 and P_T^2 are the TSP values of the current tunneling from the two ferromagnetic electrodes. The magnitude of TMR is directly related to the spin polarization of the tunneling electrons, which is determined by the spin dependence of the density of state near the Fermi energy of each of the ferromagnetic electrodes. Nowadays, MTJs using highly oriented (100) MgO as a barrier material has shown giant TMR ratios in excess of 200% at room temperature and ~300% at low temperature [1.45], providing more opportunity for extending TMR recording head applications [1.46] Moreover, these devices show remarkable thermal stability providing more opportunity for integration with CMOS circuits for MRAM applications [1.45].

It is anticipated that CPP devices will replace CIP devices because of the fabrication advantages. It is much easier to control physical track width with the stack etch used in CPP sensors. In addition, the MTJs have no magnetic material on the sides allowing for better control of side reading. Both the MTJ and CPP multilayer have higher MR ratios than today's spin valves. However, both devices exhibit additional noise, especially at low frequencies, which is a big concern. Although problems remain to be solved, the CPP sensor shows great promise in delivering manufacturability and high sensitivity for advanced areal densities and data rates.

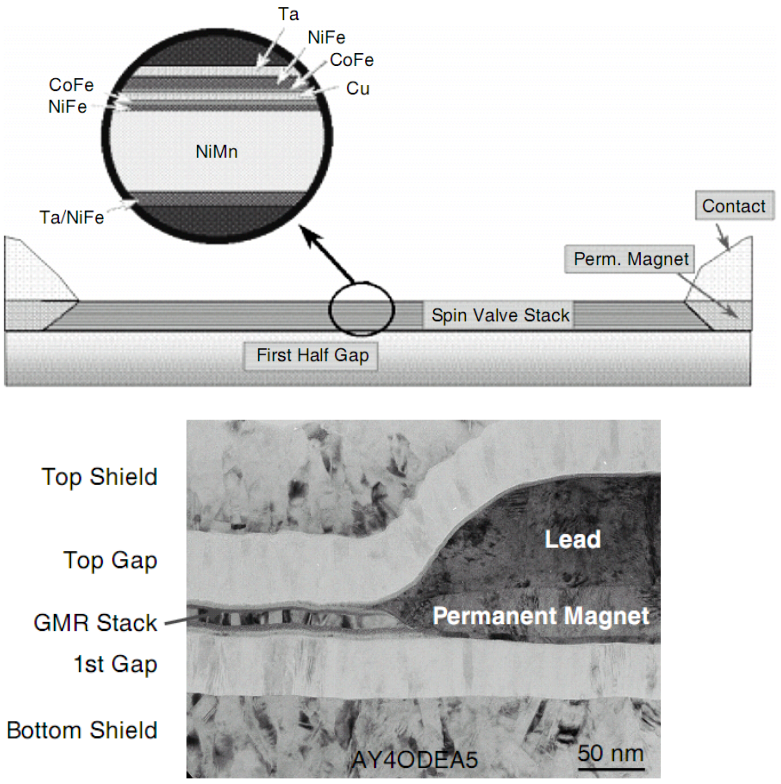

[Courtesy of Seagate Technology LLC]

Figure 1. 10 Cross section of a GMR reader.

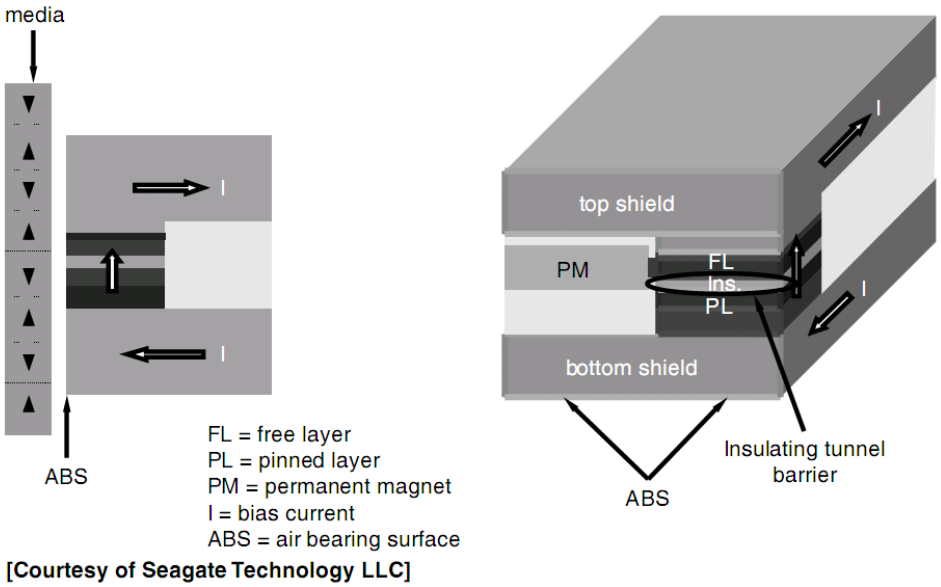

[Courtesy of Seagate Technology LLC]

Figure 1. 11 Magnetic tunnel junction read head.

1. 4 Current progress in perpendicular magnetic recording

The extensive theoretical and experimental research work associated with perpendicular magnetic recording media have contributed significantly to the good understanding of relationship between magnetic media properties and recording performance.

The progress of research on CoCrPt-oxide based media will be decided by SNR, thermal stability and writability. SNR improvement will be decided by c-axis dispersion, grain size and grain size distribution. Thermal stability is essentially decided by the materials. Writability is determined by the media design, such as the stacking of layers or through design of thinner intermediate layer.

To improve writability determined by the media structure, novel approaches have been proposed by researchers in the recent past [1.47][1.48]. One approach proposed by Piramanayagam *et al.* involves replacing the amorphous SUL by a crystalline soft underlayer to obtain the hcp (002) texture for the recording layer. However, the reduction of noise associated with a crystalline SUL for high-density perpendicular recording media is a key challenge for this idea [1.49]. In an effort to use the best features of both a-SUL and c-SUL and further reduce the effective magnetic thickness, an alternative approach is proposed. The novel structure is a hybrid soft underlayer media, which consists [1.50] of an amorphous SUL, non-magnetic seed layer and crystalline SUL, such as FeCoTaCr. The crystalline SUL can contribute to the writing process as an SUL but also provide a growth template for the layer above.

To overcome the writability problem for media with high anisotropy, Victora and Shen [1.51] proposed the exchange coupled composite media. In this media, a soft magnetic grain and a hard magnetic grain are exchange coupled to each other. It exhibits approximately half the switching field of conventional perpendicular media at the same level of thermal stability. Wang et. al [1.52] have carried out experimental work on such media with Co/Pd recording layer and FeSi soft layer. In addition, synthetic antiferromagnetic exchange coupled composite media can reduce the

switching field by 60% [1.53], compared to its conventional counterpart at the same level of thermal stability. Recording at 1 Tbits/in^2 using a composite media with this synthetic antiferromagnet hard layer has been proposed with several realistic constraints [1.54].

To achieve areal density beyond 1 Tbits/in^2, there is an evident conflict between the writability and the coercivity of the media, as was discussed. Higher *K*u can be achieved if we used FePt media instead of conventional CoCrPt-oxide granular media. However, the switching field of FePt can be as high as 50 kOe, but write field exceeding 17 kOe is difficult to achieve. Thermally assisted magnetic recording (HAMR) overcomes this problem by heating the medium above its Curie temperature during recording to reduce its coercivity [1.10][1.55]. Optical energy must be efficiently delivered and confined to a spot in the medium this is much smaller than the diffraction limit so that the neighboring tracks are not heated. Heating and cooling of the medium must occur within 1 ns in order to achieve the necessary date rates, to generate a large themal gradient for sharp transition shape, and to ensure thermal stability of the recorded bits during cooling to ambient.

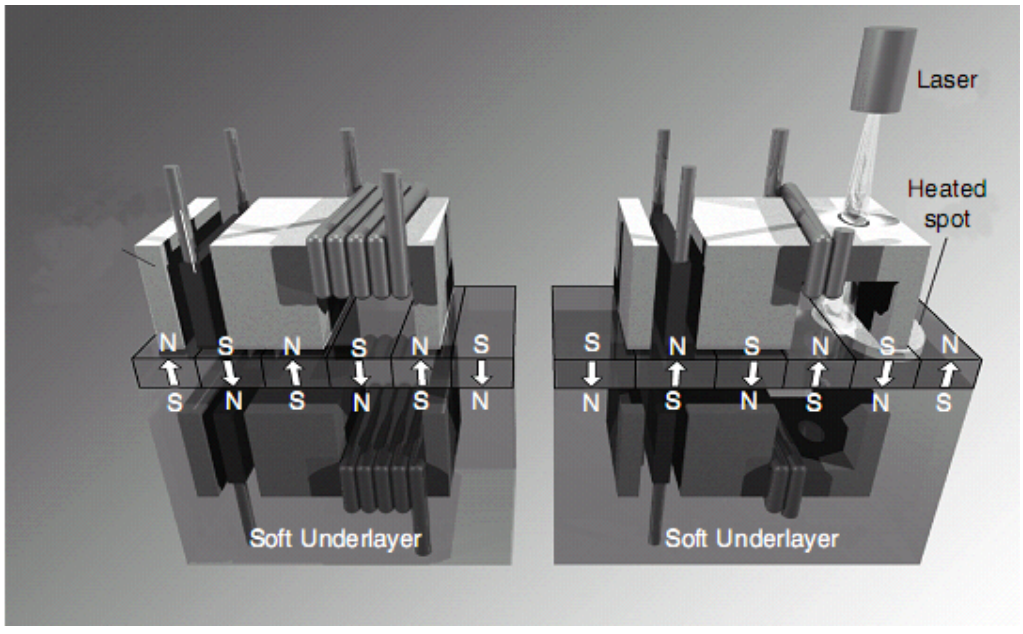

Figure 1. 12 Conventional perpendicular recording and heat assisted magnetic recording (Courtesy of Seagate Technology LLC)

There are three major challenges for the HAMR head design and process: (1) Application of a large magnetic field confined to a spatially small area. This can be addressed with a magnetic field delivery system very similar to current magnetic recording write heads [1.55]-[1.57], as see Figure 1.13; (2) Formation of an intense and spatially small optical spot on the media, This can be addressed using a planar solid immersion mirror (PSIM) to form a diffraction limited focal spot [1.56]; (3) Proper alignment of the optical and magnetic fields. This can be addressed by a novel head design with advanced nanofabrication and thin film processing.

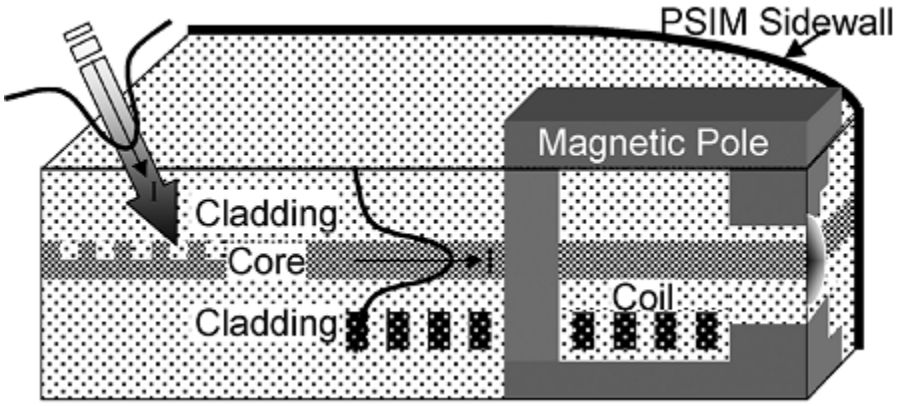

Figure 1. 13 Cross-sectional diagram of a conventional magnetic recording write head with a parabolic shaped planar waveguide passing between the write pole and the return pole. [1.52]

It has been argued that the difficulty of extending the magnetic recording areal density up to 1 Tbit/in^2 is due to the limitations of perpendicular recording media itself. In conventional media, the magnetic thin film is composed of small and single-domain grains which neither have ordered pattern, nor identical sizes. The irregularity and the strong interaction of the grains cause transition noise and thus deteriorates the signal-to-noise ratio at ultra-high areal densities. Moreover, grain size cannot be shrunk significantly without the magnetization becoming unstable or superparamagnetic. Bit patterned media, in which each bit is stored in a single-domain magnetic island, have been suggested to extend areal density beyond 1 Tbit/in^2 [1.58]. The lithographically separated islands can reduce or eliminate transition noise and non-linear bit shift, simplify track edges, and provide a solution for thermal instability because the stability

criterion refers to the anisotropy and the whole volume of a single island, not to the individual grain mentioned above.

The problems associated with bit patterned media recording arise from the fluctuations of the dots. Specifically, variations in island size and island spacing, statistical fluctuations in switching field and variance in writing synchronization and magnetic fly height can deteriorate the recording performance and lead to writing errors. The write head field strength and field gradient becomes very important for achieving satisfactory bit error rate performance.

Bit patterned media at 1 Tbit/in^2 and beyond will require fabrication of sub-10 nm discrete magnetic islands covering a full disk with tight spacing and size distributions and a narrow switching field distribution. Lithographic techniques in combination with nano-imprint are being discussed as one potential way to manufacture bit patterned media. Self organization is also a viable route to produce ordered arrays of very small particles and the combination of lithographic techniques as a guide pattern for self-organized arrays has been successfully demonstrated [1.59]. Directed block copolymer assembly lithography [1.60] and other self assembly techniques are considered to be a promising cost-effective approach to achieve higher density and dimensional uniformity.

Perpendicular recording is subjected to the trilemma and the thermal effects will ultimately limit the achievable areal density. However, there is a general agreement that it should be physically possible to achieve an areal density of 1Tbits/in^2 with perpendicular recording. Magnetic recording will remain an area of fascinating physics and commercial importance.

1. 5 The scope of this thesis

The research work of this thesis is mainly focused on using micromagnetic simulation to study various perpendicular recording media. Micromagnetic simulation studies were performed to verify the writability improvement in media using a hybrid soft underlayer and to compare to conventional media with an amorphous soft

underlayer. A micromagnetic writing process and reciprocal read back process are included for calculating the transition noise power and position jitter for different medium magnetizations with various linear densities. A realistic grain configuration (Voronoi cell) is used to describe the irregularity of grains and grain size distribution, which is indispensable for the study of medium noise and transition jitter. A notable result for medium noise obtained from micromagnetic simulation is consistent with our analytical argument. Furthermore, a micromagnetic numerical technique has been used to demonstrate how intergranular exchange coupling and intrinsic anisotropy field dispersion can be extracted from measuring two types of M-H curves. A scaling theory is utilized for dealing with thermal fluctuation effects over long time scales. The effects of intergranular exchange coupling and anisotropy dispersion are examined by finding their correlation to differentiated M-H curves with different initial magnetization states, even in the presence of thermal fluctuation. To study the feasibility of recording at 4Tbits/in^2, micromagnetically optimized specifications including 3D write head and exchange coupled composite (ECC) based bit pattern media are proposed. A 3D write head including main pole, side shields and trailing shield are optimized to obtain a sufficiently large field and gradient. The shielding effect of the head and the demagnetizing field distribution are studied. The bit error rate is then evaluated based on the demagnetizing field distribution and other field fluctuations arising from the jitter noise and writing synchronization error unique to bit patterned recording.

The organization of the thesis is as follows: In Chapter 2, the theoretical principle of micromagnetic models is presented. Thermal fluctuations are included in the gyromagnetic dynamic LLG equations. In Chapter 3, the design and writability improvement of CoCrPt-oxide based perpendicular recording media with hybrid soft underlayer is presented. In Chapter 4, a puzzling noise plateau property for perpendicular recording media is studied. The causes of the noise plateau similar to those causing the non-linear-transition-shift of signal are presented. In Chapter 5, we present micromagnetic simulation to show how intergranular exchange coupling and intrinsic anisotropy field dispersion can be extracted. The validity of this method is investigated with a series of intergranular exchange couplings and anisotropy

dispersions for different media thickness. In Chapter 6, micromagnetically optimized specifications including a 3-D write head and ECC based bit pattern media are proposed for 4 Tbit/in^2 recording. We summarize the dependence of bit error rate and bit aspect ratio on magnetic fly height, media thickness and thermal stability ratio of the media.

Chapter 2 Micromagnetic Modeling

Micromagnetic theory was first proposed by Landau Lifshitz in 1935 and was extensively reviewed and developed by William Fuller Brown, Jr. [2.1]. Micromagnetics is "*the study of ferromagnetic materials on the scale small enough to reveal details of the transition region between domains yet large enough to permit the use of a continuous magnetization vector rather than of individual atomic spins*" [2.1]. It assumes locally conserved magnetic moments that are exchange coupled over short ranges and interact magnetostatically over long ranges. In particular, this method accounts for the exchange interaction and the shape anisotropy effect. This facilitates understanding that the response of ferromagnetic devices to external fields is very different from what one might be expected based on the intrinsic properties of the bulk materials.

2.1 The Landau-Lifshitz-Gilbert Equation

To study the dynamic properties and time evolution or the transient state of the magnetization switching, the gyromagnetic precession of motion and damping should be considered. The dynamic motion of the magnetization is generally described by the Landau-Lifshitz-Gilbert (LLG) equation:

$$\frac{d\mathbf{M}}{dt} = \frac{\gamma}{1+\alpha^2}\mathbf{M}\times\mathbf{H}_{eff} - \frac{\alpha\gamma}{(1+\alpha^2)M_s}\mathbf{M}\times(\mathbf{M}\times\mathbf{H}_{eff}) \tag{2.1}$$

In this equation, γ is the gyromagnetic ratio of the free electron spin that can be calculated by $\gamma=\mu_0 g|e|/2m_e$, where g is the Landé factor and m_e is the electron's mass. **M** is the magnetization vector at a location and $\mathbf{H}_{\text{eff}}$ is the total effective field acting on the magnetization. α is damping constant. The first term on the right hand side of the equation, a direct result of the torque equation, describes the gyromagnetic precession of the magnetization that can continue forever. It is known as Larmor precession with angular frequency of $\omega = \gamma H$ when α=0. The second term is a phenomenological damping term that cannot be theoretically derived from basic principles. The damping term, introduced by Gilbert, describes the dissipation of magnetic energy. It causes the

magnetization to be aligned to the direction of the total effective field as the system proceeds towards the equilibrium state. The dynamic relations of the two terms with respect to the magnetization are illustrated in Figure 2.1.

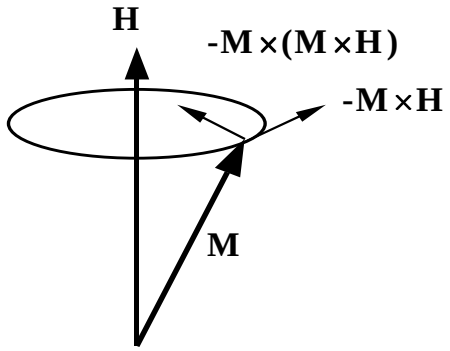

Figure 2. 1 Damped gyromagnetic precession of a magnetization vector.

The dimensionless damping constant α is usually hard to determine for magnetic materials. This is because strictly speaking α is not a constant. It depends nonlinearly on the magnetization owing to the interaction of the magnetization with phonons, conducting electrons etc, and has strong correlation with the microstructure of the material. In numerical simulation, α is usually taken to be an unchanged value for a specific material. For example, for hard magnetic materials such as recording media, α is taken to be 0.1 or larger. For thin film soft magnetic materials such as CoFe and NiFe, α is usually less than 0.05.

Using spherical coordinate system, the LLG equation can be written in θ and ϕ as:

$$\frac{d\theta}{dt} = \frac{\gamma}{1+\alpha^2}(H_x \sin\varphi - H_y \cos\varphi) - \frac{\alpha\gamma}{1+\alpha^2}(-H_x \cos\theta\cos\varphi - H_y \cos\theta\sin\varphi + H_z \sin\theta)$$
$$\frac{d\varphi}{dt} = \frac{\gamma}{1+\alpha^2}(H_x \frac{\cos\theta\cos\varphi}{\sin\theta} + H_y \frac{\cos\theta\sin\varphi}{\sin\theta} - H_z) - \frac{\alpha\gamma}{1+\alpha^2}(H_x \frac{\sin\varphi}{\sin\theta} - H_y \frac{\cos\varphi}{\sin\theta})$$

(2.2)

The LLG differential equations are usually solved by using integration methods. In this thesis, the high precision forth-order Runge-Kutta method is employed to calculate the time evolution of the magnetization.

The classical micromagnetic theory was for solving a continuous distribution of magnetizations, which can be obtained in some special cases. For some more complex materials, however, discretization is needed to break the continuum of magnetization distribution into small units on the scale small enough to assume a constant magnetization distribution. For magnetic soft materials, it is reasonable to discretize the specimen into an array of cubic cells. For magnetic hard materials such as recording media, on the other hand, the magnetic properties are not uniform and the granularity in hard material usually cause irregular shape of magnetic domains and therefore it is reasonable to use an array of non-uniform cells.

2.2 Geometric configuration

In this thesis, we used a micromagnetic model to study various properties of perpendicular recording media in a perpendicular recording system, which consists of both hard magnetic recording layer and soft magnetic materials, as shown in Figure 2.2. The soft materials are used for the recording head and the soft underlayer, which can be represented by rigid cubic arrays. The magnetic recording layer, which is hard material, is represented by non-uniform Voronoi cells.

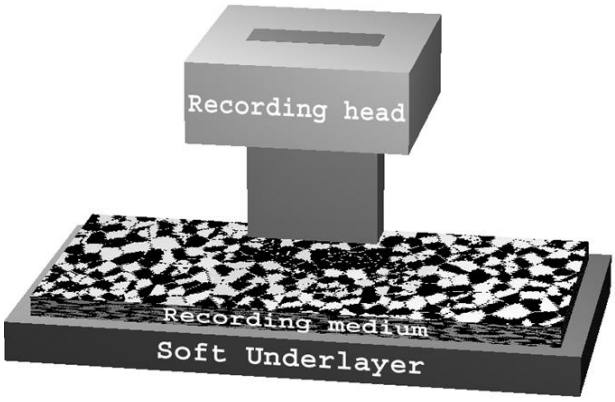

Figure 2. 2 Illustration of a perpendicular recording system using a single pole head and a perpendicular medium with soft underlayer. [2.2]

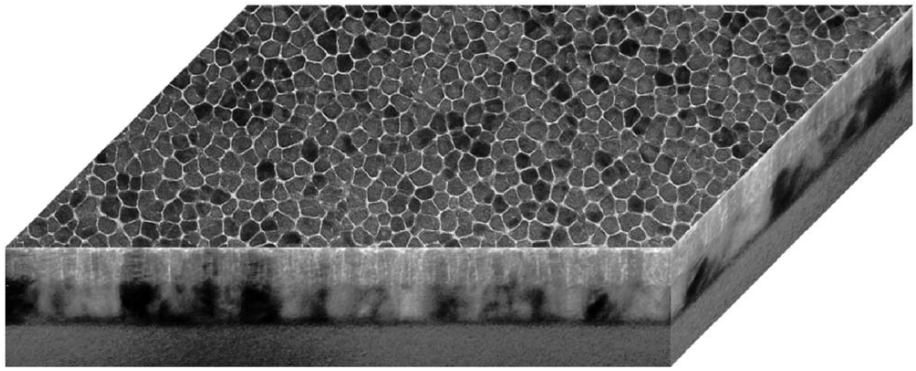

Figure 2. 3 3-D construction of TEM images of a CoCrPt-SiO2 granular thin film, which is constructed with plane-view and cross section images. [2.3]

From the 3-D construction of transmission electron microscopy (TEM) images of perpendicular thin films given in Fig. 2.3, it is clear that the films have a complicated morphology. This cannot be well represented by the assumption of regular grains such as spherical grains, hexagonal grains, etc. It is important to accurately describe the real grain system in a mathematically feasible approach, especially when the thermal fluctuation effect is taken into account. Regular grains may not correctly describe the thermally activated magnetization reversal occurring in real films. This may reduce the media noise level because media noise is mainly determined by the non-uniformity of magnetic moment such as the reversed domain or the magnetic cluster whose formation relies on inter-granular interaction. Voronoi construction that consists of randomly distributed polygons in two-dimensional space was used to represent the grain morphology [2.4]. The advantages of using this scheme are that, based on micromagnetic theory, it can better simulate the interaction between real grains and make it possible to account for the effect of grain size distribution on film characteristics, such as thermal fluctuations. Statistically, it is easy to control average grain size and the grain size distribution. It will be shown that the grain size distribution generated by the Voronoi scheme basically follows a log-normal function, similar to the actual grain size distribution.

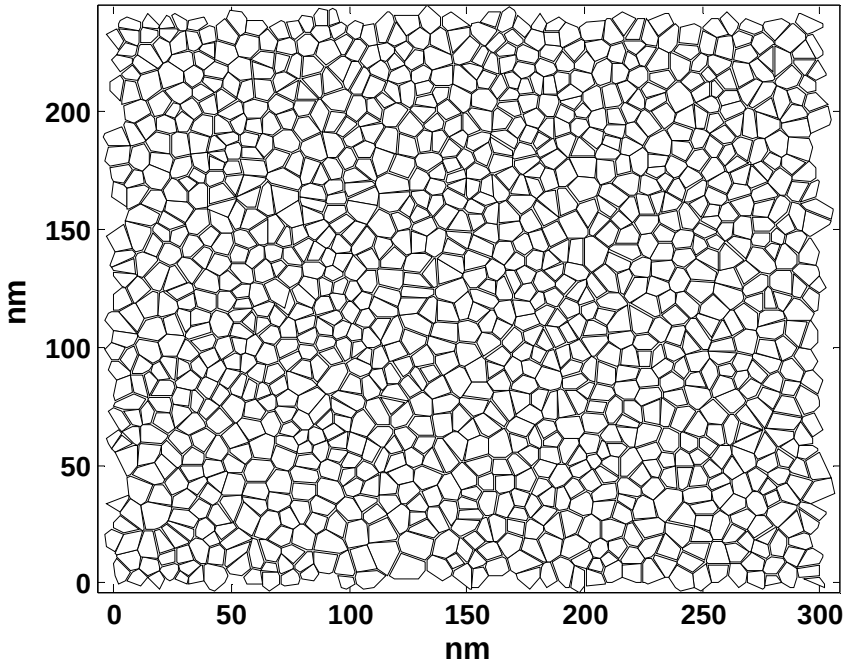

Figure 2. 4 Schematic Diagram of an array of 1200 grains generated by Voronoi cells.

Voronoi cells are generated by first defining uniformly distributed random seed points within a two-dimensional space. Given a set of seed points $P = \{p_0, p_1, p_2, \ldots\}$ in a plane, one can partition the plane into Voronoi cells (polygons) such that a Voronoi cell about a point p in P consists of all points in the plane which are closer to p than any other point in P. The edge of a polygon Voronoi Cell is a subset of the perpendicular bisector of the line segment connecting two points, say p_0 and p_1. The smallest area enclosed by the bisecting lines is the Voronoi cell. The polygonal grains generated by this procedure are very similar to the growth of real grains where random islands are generated during sputtering, and the polycrystalline structure is formed after crystals grow along the islands. An example of an array of 1200 Voronoi cells is given in Fig. 2.4. A uniform grain boundary of 1 nm is added between the neighboring grains. To reduce the abrupt edge effect, periodic boundary conditions are applied to the array of grains.

The parameters used to define a piece of thin film include average grain diameter <D>, standard deviation of diameter σ_D, grain boundary spacing d, and film thickness δ. Adjusting the minimum distance between seed points can easily change grain irregularity or the variance of the grain size [2.4]. A grain size distribution for grain configuration in Fig. 2.4 is shown in Fig. 2.5 where the average grain diameter is ~8.1 nm and the standard deviation equals ~15% of the average grain diameter. A logarithmic normal curve is also plotted, which is found to be in compliance with the distribution.

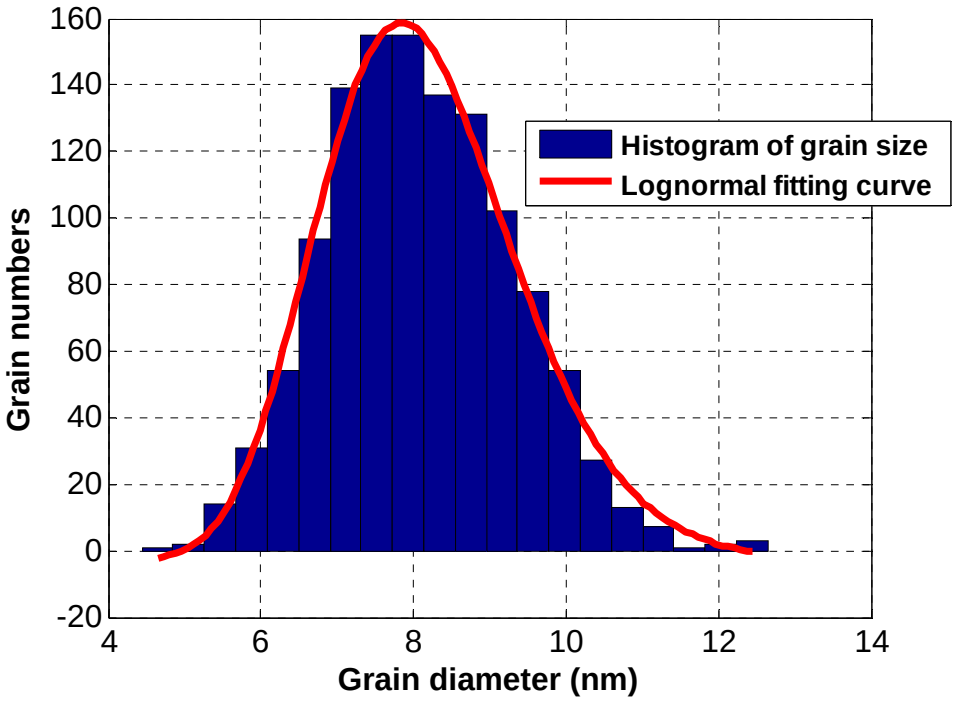

Figure 2. 5 An example of grain distribution (1200 grains, mean size=80.9 Å, standard deviation=12.1 Å) generated by Voronoi configuration. A logarithmic normal curve is also showed (solid line).

2.3 Magnetic Energies in Grains and Cubic cells

As mentioned in Chapter 2.1, the micromagnetic method is essentially a continuum method that assumes the magnetization to be a continuous function of

position in a material. In a Cartesian coordinate system, the magnetization vector is expressed as

$$\mathbf{M} = M_x\mathbf{i} + M_y\mathbf{j} + M_z\mathbf{k} \qquad (2.3) \quad \text{and} \quad \sqrt{M_x^2 + M_y^2 + M_z^2} = M_s \qquad (2.4)$$

or expressed in spherical coordinates using the polar angle ϕ and the azimuthal angle θ to automatically satisfy the condition of constant magnitude $|\mathbf{M}| = M_s$.

Without taking into account magnetoelastic and surface anisotropy effects (the magnetoelastic energy is at least partially included in the magnetocrystalline anisotropy if the anisotropy constant is obtained from experiment), the total magnetic Gibb's free energy of a single domain grain subjected to an external field can be expressed as [2.1]:

$$E_t = E_{ani} + E_{mag} + E_{exch} + E_{Zeeman} \qquad (2.5)$$

where E_{ani} is the magnetocrystalline anisotropy energy, E_{mag} is the magnetostatic interaction energy, E_{Zeeman} is Zeeman energy and E_{exch} is the intergranular exchange coupling energy. Each energy term is a function of magnetization **M**.

The basic goal of micromagnetic simulation is to study the dynamic behavior of the magnetization process and the magnetic energy dissipation or to calculate the final magnetization orientation when the magnetic system achieves a stable equilibrium state. In term of magnetization equilibrium distribution, there are generally many states a magnetic-particle system can have on its energy surface. When its environment is changed, such as the applied field is changed, the magnetization orientations will accordingly change to seek the new local minimum of the particle system. A dynamic study is essential for a low damping system such as magnetic write head where the magnetization switching time and the head field rise time are crucial in high data rate.

The LLG equation has to be solved for magnetization in a time domain. For both dynamic and static (equilibrium state) micromagnetic calculations using LLG equation, the effective field of a grain is generally required during each iteration of integrating calculation. It is the sum of the magnetostatic interaction field, the exchange coupling

field, the crystalline anisotropy field, and the applied field, and can be calculated from the energy densities:

$$\mathbf{H}_{eff} = -\frac{\partial E_t}{\partial \mathbf{M}} = -(\frac{\partial E_{ani}}{\partial \mathbf{M}} + \frac{\partial E_{mag}}{\partial \mathbf{M}} + \frac{\partial E_{exch}}{\partial \mathbf{M}}) + \mathbf{H}_{app} \tag{2.6}$$

where $\mathbf{H}_{app}$ is applied field. In general, the effective field can be also classified into local fields, such as anisotropy field and exchange coupling field, and long-range interaction fields, such as magnetostatic interaction field and external field. Each of them will be discussed in the following sections.

2.3.1 Magnetostatic Interaction Energy

Magnetostatic energy is the interaction between the magnetization and the magnetic field. This in nature reflects the long-range dipole-dipole interaction between spins at atomic lattice sites within magnetic bodies. Practically, the energy includes magnetostatic self-energy in a volume where the magnetic field is generated by the magnetization itself, and the interaction energy between different magnetic volumes where the field is generated by the surrounding magnetizations. The total magnetostatic energy in a volume *V* can be written as

$$E_{mag} = -\frac{1}{2}\int_V (\mathbf{H}_{mag} \cdot \mathbf{M}) dv \tag{2.7}$$

where $\mathbf{H}_{mag}$ is the interaction field created by **M**, and the factor of ½ is to remove energy double counting when summing up the energy in *V*. In most micromagnetic models, almost all computer time is spent on the calculation of magnetostatic interaction energy. Meanwhile, this calculation is not only time consuming, but also the most difficult part to get accurate result. Therefore, we will discuss the magnetostatic calculation in more detail for the Voronoi grains.

The magnetic field can be calculated either by directly applying Maxwell equations through a scalar potential calculation or from the calculation of magnetostatic

interaction energy. In using Maxwell equations, since $\nabla \cdot \mathbf{B} = 0$ and $\mathbf{B} = \mathbf{H} + 4\pi\mathbf{M}$, we can obtain

$$\nabla \cdot \mathbf{H} = -4\pi \nabla \cdot \mathbf{M} \tag{2.8}$$

by combining the two equations. For convenience, by introducing a scalar potential to let $\mathbf{H} = -\nabla\varphi$, a Poisson equation inside the material can be obtained:

$$\nabla^2 \varphi_{in} = 4\pi \nabla \cdot \mathbf{M} \tag{2.9}$$

Outside of the material, the potential follows Laplace's equation:

$$\nabla^2 \varphi_{out} = 0 \tag{2.10}$$

With flux continuity, two boundary conditions for the potential are:

$$\varphi_{in} = \varphi_{out} \tag{2.11}$$

$$\frac{\partial \varphi_{in}}{\partial n} - \frac{\partial \varphi_{out}}{\partial n} = 4\pi \mathbf{M} \cdot \mathbf{n} \tag{2.12}$$

The solution can be calculated by :

$$\varphi(\mathbf{r}) = -\int_{V'} \frac{(\nabla \cdot \mathbf{M}(\mathbf{r}'))dv'}{|\mathbf{r} - \mathbf{r}'|} + \int_{S'} \frac{(\mathbf{M}(\mathbf{r}') \cdot \mathbf{n})ds'}{|\mathbf{r} - \mathbf{r}'|} \tag{2.13}$$

where $\nabla \cdot \mathbf{M}$ is volume magnetic charge density and $\mathbf{M} \cdot \mathbf{n}$ is surface magnetic charge density. The integrations are taken over the magnetic body and all its surfaces. The field at point **r** is then obtained as:

$$\mathbf{H}(\mathbf{r}) = -\int_{V'} \frac{(\nabla \cdot \mathbf{M}(\mathbf{r}'))dv'}{|\mathbf{r} - \mathbf{r}'|^3}(\mathbf{r} - \mathbf{r}') + \int_{S'} \frac{(\mathbf{M}(\mathbf{r}') \cdot \mathbf{n})ds'}{|\mathbf{r} - \mathbf{r}'|^3}(\mathbf{r} - \mathbf{r}') \tag{2.14}$$

The point field is appropriate to use for distant grains away from the integrated magnetic charges. For the interactions between grains close to each other, the effect of grain's shape has to be taken into account. The above field is to be integrated over grain's volume, and a volume-averaged field will be applied into LLG equation. Instead of using the direct volume integration for Eq. (2.14), in most numerical applications, the

magnetostatic interaction energy is preferable for magnetic field calculation to lower numerical errors such as higher order singularity problems. The expression for the interaction energy between grain *i* and *j* is given as:

$$E_{mag}^{ij} = \frac{1}{2}[\int_{V_i} dv_i \int_{V_j} \frac{\rho_i \rho_j}{r_{ij}} dv_j + \int_{S_i} ds_i \int_{S_j} \frac{\sigma_i \sigma_j}{r_{ij}} ds_j + \int_{V_i} dv_i \int_{S_j} \frac{\rho_i \sigma_j}{r_{ij}} ds_j + \int_{S_i} ds_i \int_{V_j} \frac{\sigma_i \rho_j}{r_{ij}} dv_j] \tag{2.15}$$

where ρ and σ are volume and surface charge densities. For single-domain particles (ρ=0), only the four-fold surface charge integration is performed. The Voronoi grains have top and bottom polygonal surfaces and rectangular side surfaces. The interaction energy between grain *i* and *j* is calculated over three kinds of surface-pair integrations: (1) side surface of grain *i* to side surface of grain *j*; (2) side surface of grain *i* to top (or bottom) surface of grain *j*; (3) top (or bottom) surface of grain *i* to top (or bottom) surface of grain *j*. The energy is written as:

$$E_{i,j} = \sum_l \sum_m (\mathbf{M}_i \cdot \mathbf{n}_{il})(\mathbf{M}_j \cdot \mathbf{n}_{im}) \overset{\smile}{T}{}^{e}_{il,jm} \tag{2.16}$$

where *l* and *m* are grain surface numbers, and $\overset{\smile}{T}{}^{e}_{il,jm}$ is the energy tensor between surface *l* of grain *i* and surface *m* of grain *j*. The total magnetostatic interaction energy of the thin film is the summation of the energy between every pair of grains:

$$E_{mag} = \frac{1}{2} \sum_{i,j} E_{i,j} \tag{2.17}$$

The effective magnetostatic interaction fields in grain *i* are calculated by:

$$\begin{aligned} H_{ix} &= -\frac{1}{v_i} \frac{\partial E_{mag}}{\partial M_{ix}} \\ H_{iy} &= -\frac{1}{v_i} \frac{\partial E_{mag}}{\partial M_{iy}} \\ H_{iz} &= -\frac{1}{v_i} \frac{\partial E_{mag}}{\partial M_{iz}} \end{aligned} \tag{2.18}$$

where v_i is grain's volume, and M_{ix}, M_{iy}, M_{iz} are the magnetization components in the grain. In our application, the interaction fields are calculated using an interaction tensor

$$\mathbf{H}_{mag}(\mathbf{r}_i) = \sum_{j=1}^{NG} \overset{\tau}{T}_{ij} \mathbf{M}(\mathbf{r}_j) \tag{2.19}$$

The tensor between grain i and j consists of elements in a matrix as:

$$\overset{\tau}{T}_{ij} = \begin{bmatrix} T_{ij}^{xx} & T_{ij}^{xy} & T_{ij}^{xz} \\ T_{ij}^{yx} & T_{ij}^{yy} & T_{ij}^{yz} \\ T_{ij}^{zx} & T_{ij}^{zy} & T_{ij}^{zz} \end{bmatrix} \tag{2.20}$$

Because of the straight-line geometric extension of Voronoi grains along the z direction (the film normal), the cross elements that include z in the above matrix, T_{ij}^{xz}, T_{ij}^{yz}, T_{ij}^{zx} and T_{ij}^{zy} essentially equal zero. For the case when $j \neq i$, geometric mapping techniques are used to numerically integrate the top and bottom polygonal surfaces. For example, for a 5-side polygonal surface in Figure 2.6, we can consider it to be two quadrangles (triangle is a special quadrangle). An arbitrary quadrangle can be mapped to a square by the following translation of coordinate systems, from x-y system to ξ-η system [2.6]:

$$\begin{aligned} x(\xi,\eta) &= \sum_{i=1}^{4} N_i(\xi,\eta) x_i \\ y(\xi,\eta) &= \sum_{i=1}^{4} N_i(\xi,\eta) y_i \end{aligned} \tag{2.21}$$

where x_i and y_i are the corner coordinates of a quadrangle in x-y, the shape function is defined as :

$$\left.\begin{aligned} \boldsymbol{N}_1(\xi,\eta) &= (1-\xi)(1-\eta)/4 \\ \boldsymbol{N}_2(\xi,\eta) &= (1+\xi)(1-\eta)/4 \\ \boldsymbol{N}_3(\xi,\eta) &= (1+\xi)(1+\eta)/4 \\ \boldsymbol{N}_4(\xi,\eta) &= (1-\xi)(1+\eta)/4 \end{aligned}\right\} \tag{2.22}$$

The Gaussian quadrature technique [2.7] is employed to effectively carry out the integration. The relation between areas in the two coordinate systems is:

$$dxdy = \det J d\zeta d\eta \tag{2.23}$$

where the Jacobian can be calculated by the derivative of coordinates in *x*-*y* with respect to the coordinates in ξ-η:

$$\det J = x_{,\zeta} y_{,\eta} - x_{,\eta} y_{,\zeta} \tag{2.24}$$

In each direction, 5-8 Gaussian points are used to calculate the integration.

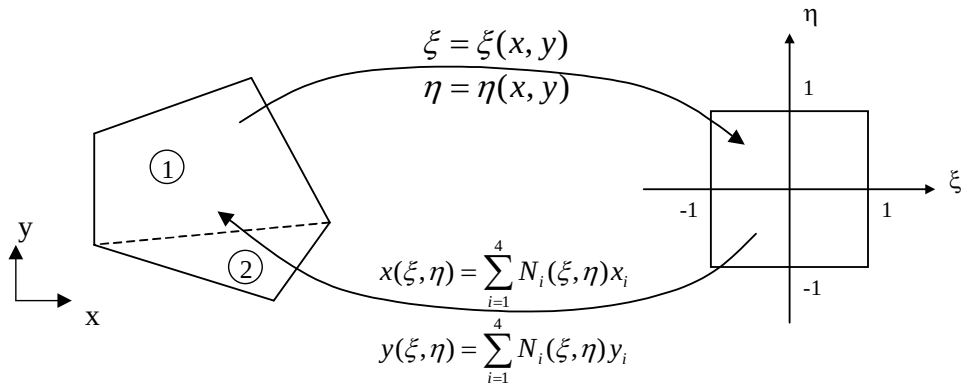

Figure 2. 6 Geometrical mapping an arbitrary quadrangle into a square for surface integration calculation.

For the case when *j*=*i*, the tensor elements actually represent the self-demagnetization factors of the grain. The calculation of the in-plane element T_{ii}^{xx} or T_{ii}^{yy} includes two integrations: (1) numerical integration for the magnetostatic interaction energy between different side surfaces; (2) an analytical integration for the self-magnetostatic energy of a single side surface. This analytical integration avoids the singularity raised if the integration was performed numerically. Following is the expression for the self-interaction energy in a side surface [2.8]:

$$\begin{aligned} E_{self} &= \int_{-\frac{e}{2}}^{\frac{e}{2}} dx \int_{-\frac{h}{2}}^{\frac{h}{2}} dy \int_{-\frac{e}{2}}^{\frac{e}{2}} dx' \int_{-\frac{h}{2}}^{\frac{h}{2}} dy' \frac{\sigma^2}{[(x-x')^2 + (y-y')^2]^{1/2}} \\ &= \frac{\sigma^2}{3}[-2(e^2+h^2)^{3/2} + 2e^3 + 2h^3 + 6e^2 h \ln(\sqrt{e^2+h^2}+h) \\ &\quad - 6e^2 h \ln e + 6eh^2 \ln(\sqrt{e^2+h^2}+e) - 6eh^2 \ln h] \end{aligned} \tag{2.25}$$

In-plane cross elements T_{ii}^{xy} and T_{ii}^{yx} can be calculated using T_{ii}^{xx} and T_{ii}^{yy} together with the demagnetization factor for a 45° direction in the *x*-*y* plane:

$$T_{ii}^{45^\circ} = \frac{1}{2}T_{ii}^{xx} + \frac{1}{2}T_{ii}^{yy} + T_{ii}^{xy} \tag{2.26}$$

It is verified that the cross elements are negligible in comparison with T_{ii}^{xx} and T_{ii}^{yy} when the grain is more symmetric. Another element T_{ii}^{zz} is obtained using the relation that the sum of the three normalized orthogonal elements equals unity. This avoids a singular integration over an arbitrary polygonal surface.

2.3.2 Magnetocrystalline Anisotropy Energy

Hysteresis in magnetic materials stems from the anisotropy energy of the materials. In a typical micromagnetic calculation of recording media, the anisotropy energy mainly consists of shape anisotropy and magnetocrystalline anisotropy. Macroscopic shape anisotropy has its origin in the magnetostatic interaction of spins, which is already represented in term of the magnetostatic interaction calculation as mentioned earlier. Magnetocrystalline anisotropy is an intrinsic feature of a magnetic material. The physical origin of the crystalline anisotropy in magnetic material is the spin-orbit interaction of the electrons [2.5][2.9]. Owing to strong coupling between orbit and lattice (orbital moment *L* is almost entirely quenched), and weak coupling between spin and orbit, the spin prefers to align along special directions of the lattice (crystallographic axes). When an external field is applied, the spin of an electron tends to align perpendicularly to the orbit of the electron (or the lattice). The energy required to rotate the spin away from the easy direction, which we call the anisotropy energy, is just the energy required to overcome the spin-orbit coupling. The strength of the anisotropy in any particular crystal is measured by the magnitude of the anisotropy constant K_{u1}, K_{u2}, etc. Anisotropy energy is related to the local directions of magnetization with respect to the easy axes. For a hexagonal close-packed structure, for

example, the *c* axis is the easy direction of magnetization. The crystalline anisotropy energy (uniaxial anisotropy) is expressed as a power series of $\sin\theta$:

$$E_{ani} = K_{u0} + K_{u1}\sin^2\theta + K_{u2}\sin^4\theta + \Lambda \tag{2.27}$$

where K_{u0}, K_{u1}, K_{u2} … are energy constants, and θ is the angle between magnetization and easy direction. The uniaxial anisotropy energy is often simplified as

$$E_{ani} = K_u\sin^2\theta = K_u(1-\cos^2\theta) = K_u(1-|\mathbf{k}\cdot\mathbf{m}|^2) \tag{2.28}$$

after removing the constant term K_{u0} and combining the effect of K_{u1} and K_{u2} into K_u (for K_{u2} negligibly small), where **k** and **m** are easy axis direction and magnetization direction, respectively. The effective anisotropy field can be therefore calculated by:

$$\begin{aligned} H_{xani} &= H_k\alpha_{easyaxis}\alpha_m \\ H_{yani} &= H_k\beta_{easyaxis}\beta_m \\ H_{zani} &= H_k\gamma_{easyaxis}\gamma_m \end{aligned} \tag{2.29}$$

where $\alpha_{easyaxis}$, $\beta_{easyaxis}$, $\gamma_{easyaxis}$ and α_m, β_m, γ_m are the direction cosines of easy axis and magnetization, and H_k is the crystalline anisotropy field $2K_u/M_s$. Anisotropy constant is usually measured from experiment. For example, for normal perpendicular recording media, K_u is above 10^6 erg/cm^3. The experimentally measured K_u is obviously a volume-averaged value, but in a real magnetic specimen, the magnitude of K_u (or H_k) varies from grain to grain. However, the distribution of its variation is hard to measure. Also, the easy axes can be changed from grain to grain, following a specified distribution of angles.

2.3.3 Exchange Coupling Energy

One important characteristic of ferromagnetic materials is the strong interaction between spins. With the interaction, each spin tends to align other surrounding spins parallel or anti-parallel to its own direction. In quantum mechanics, this spin-spin

interaction, known as exchange coupling, is a consequence of the Pauli Exclusion Principle. It states that two electrons can have the same energy and location only if they have opposite spins, and that the electrons having smaller overlap of their wave functions will have parallel spins. In the Heisenberg Hamiltonian format, the exchange interaction of M atoms is expressed as

$$\mathrm{E}_{exch} = -\sum_{i,j=1}^{M} J_{i,j}\mathbf{S}_i \cdot \mathbf{S}_j \tag{2.30}$$

where $J_{i,j}$ is the exchange integral that involves the overlap of the eigenfunctions of electrons and depends on the distance between the atoms [2.10]. The $J_{i,j}$ value decreases rapidly with increasing distance, so the exchange interaction is usually taken into account only for the nearest neighbor spins. Eqn. (2.30) shows that the exchange energy is lower when the spins are parallel for positive $J_{i,j}$ that corresponds to ferromagnetic interaction, and when the spins are anti-parallel for negative $J_{i,j}$ that corresponds to anti-ferromagnetic interaction. The exchange coupling energy is strong and symmetric since $\mathbf{S}_\mathrm{i}$ and $\mathbf{S}_\mathrm{j}$ can be interchanged.

In the micromagnetic model, the exchange coupling energy between the nearest neighbor grains in the recording media is included based on the above quantum mechanical expression, and the energy density equals $E_{exch} = -J\sum \mathbf{M}_i \cdot \mathbf{M}_j$,where J is the exchange coupling constant. In a Voronoi configuration, each grain has varying grain boundaries with its different nearest neighbors. The effect of interfacial area variation between grains has to be included in the exchange energy calculation. One reasonable assumption is that the exchange energy between two grains is proportional to their interfacial area. This is because the number of pairs of spins between the grains' boundary is proportional to the interfacial area. Therefore, from the above equation, the total exchange energy density can be modified as

$$E_{exch} = -J\sum \mathbf{M}_i \cdot \mathbf{M}_j \frac{a_{ij}}{a_{ave}} \tag{2.31}$$

where a_{ij} is the interfacial area between grain i and j, and a_{ave} is average side area if grains were hexagons, used to normalize the interfacial area. The summation is taken over all the nearest neighboring grains. The effective exchange field at grain i is then calculated by

$$\mathbf{H}_{exch,i} = 2J \sum \mathbf{M}_j (a_{ij} / a_{ave}) \tag{2.32}$$

Another exchange energy expression is for continuous magnetization. It can be derived from a discrete system using Eqn. (2.30) when the angle difference between two spins is small so that the higher order Tayler expansion of $\cos\theta_{ij}$ in the dot product of S_i and S_j, can be omitting, where θ_{ij}. is the angle between S_i and S_j. The final exchange energy density is given as [2.9]

$$E_{exch} = \frac{1}{2} C \left[(\nabla m_x)^2 + (\nabla m_y)^2 + (\nabla m_z)^2 \right] \tag{2.33}$$

where $C = \frac{2JS^2}{a} c$, a is the edge of unit cell, c=1, 2 and 4 for a simple cubic, *bcc* and *fcc* crystal structure respectively.

2.3.4 Zeemann Energy

This energy indicates the interaction between an applied field and magnetization of a grain. It can be calculated as:

$$E_{Zeemann} = -\mathbf{H}_{app} \cdot \mathbf{M} \tag{2.34}$$

The energy minimum is reached when the magnetization direction is aligned with the external field.

2.4 Thermal Fluctuations

Under the agitation of thermal energy, the probability of magnetization switching per unit time (or the reciprocal of relaxation time τ) of a magnetic particle with energy barrier ΔE is $P= f_0\exp(-\Delta E/k_BT)$. This statistical result indicates that magnetization jumps between energy minima at a rate exponentially depending on ΔE and temperature. In a real material, the attempt frequency f_0 is temperature and applied field dependent. However, when the energy minima width is narrow and the energy barrier is higher in comparison with k_BT, this dependence on temperature and field will become weak and can be neglected. The jumping of magnetization around its energy minima with time can be usually described as a random walk. According to Brown [2.11], this thermal disordering effect to magnetization can be included by augmenting a random fluctuation field to the total effective magnetic field in the Landau-Lifshitz-Gilbert equation. The basic assumption required to deal with the thermal effect by a random process is that the random thermal forces have correlation time much shorter than the response time of the magnetic system. At room temperature, the thermal-agitation forces have frequency of order k_BT/h ($\approx 10^{13}$ sec^{-1}). This corresponds to correlation times of order 10^{-13} sec. The response frequency of a single-domain particle is of the order of the reciprocal of its gyromagnetic resonance frequency ($\approx 10^{10}$ sec^{-1}). Brownian motion therefore can be used to describe the magnetization. The Landau-Lifshitz-Gilbert equation is changed into a stochastic differential equation of the Langevin type. The stochastic LLG equation is given as following:

$$\frac{d\vec{M}}{dt} = \frac{\gamma}{1+\alpha^2}\vec{M}\times(\vec{H}_{eff}+\vec{h}(t)) - \frac{\alpha\gamma}{(1+\alpha^2)M_s}\vec{M}\times(\vec{M}\times(\vec{H}_{eff}+\vec{h}(t))) \tag{2.35}$$

where the fluctuation field is a Gaussian random process with mean equal to zero. The correlation function of the components of the fluctuation field can be written as:

$$\left\langle h_i(t)h_j(t+\tau)\right\rangle = \sigma^2\delta_{ij}\delta(\tau) \tag{2.36}$$

where i, j=1,2,3, and $\sigma^2 = \frac{2\boldsymbol{k_B T}\alpha}{\gamma \boldsymbol{M_s V}\Delta \boldsymbol{t}}$. The Kronecker δ expresses the assumption that the different components of the fluctuation field are not correlated with each other while the Dirac δ indicates that the autocorrelation time of the fluctuation field is much shorter than the rotational-response time of the system. Furthermore, it is also assumed that the fluctuation fields acting on different magnetic moments are independent. The stochastic LLG equation is solved also using the forth order Runge-Kutta method. A uniform random number generator that has a long period >$2x10^{18}$, is used to generate the white Gaussian thermal fluctuation fields.

Chapter 3 Micromagnetic Simulation of Hybrid Soft Underlayer

One of the main aspects of perpendicular magnetic recording that makes it superior to longitudinal recording is the utilization of a single pole head and a medium comprised of a recording layer and a soft underlayer (SUL). Improvement of areal density of CoCrPt-oxide media beyond 500 Gb/in^2 will be based on several factors, such as SNR and writability improvement. As far as writability is concerned, an important issue is to reduce the spacing between the writer pole and the SUL, also called head-to-keeper spacing (HKS) [3.1][3.2] while retaining an effective seed layer to promote good recording layer growth. Currently, perpendicular recording media products have a non-magnetic seed layer with a thickness of about 15- 20 nm, as shown in Fig. 3.1(a). The presence of a non-magnetic seed layer increases the reluctance of the media and divergence of the writing field flux. The significant decrease in writing field and field gradient makes the writing process inefficient [3.3][3.4]. Therefore, an optimized underlayer structure with thinner intermediate layer (5 nm or less) is needed to obtain higher writability, while maintaining good perpendicular c-axis dispersion and smooth surfaces in the recording media.

To improve writability determined by the media structure, novel approaches have been proposed by researchers in the recent past [3.5][3.6]. One approach proposed by Piramanayagam *et al.* involves replacing the amorphous SUL (a-SUL) by a crystalline SUL (c-SUL) to obtain texture for the recording layer. With this approach, the intermediate layer is needed only for grain isolation and exchange breaking functions. Therefore, the thickness of intermediate layer can be reduced. However, the reduction of noise, roughness and grain size in recording layer associated with using a crystalline SUL pose challenges for this idea [3.7]. In an effort to use the best features of both a-SUL and c-SUL and further reduce the effective magnetic thickness, an alternative approach is proposed. The novel structure is a hybrid SUL (H-SUL) media, which consists [3.8] of an a-SUL, non-magnetic seed layer and c-SUL, as shown in Fig. 3.1(b). In order to investigate and compare the writability, micromagnetic simulations are performed on media using an a-SUL and the proposed H-SUL. By comparing the

effective write fields and gradients along the down track and cross track directions in both structures, equivalent performance can be obtained with a suitable combination of non-magnetic layers and c-SULs. Our simulation indicates that the H-SUL structure can use a thicker non magnetic seed layer and a thin non-magnetic intermediate layer without degrading the write fields and gradients at the center of the recording layer, whereas it is difficult for media with a-SUL to reduce the non-magnetic intermediate layer thickness while retaining an adequate seed.

3.1 Design of Hybrid Soft Underlayer

Fig. 3.2(a) shows the design of conventional perpendicular media with a-SUL and non-magnetic seed layer of about 15-20 nm thickness, and recording layer of about 15 nm thick. Typically non-magnetic layers are used to decouple the a-SUL and the recording layer, and provide a template for inducing a good perpendicular c-axis orientation and grain isolation in the magnetic recording layer [3.9][3.10]. Due to these multiple functions, Ta/Ru seed layers are often used [3.11] in conventional media. It is usually observed that the increase of seed layer thickness leads to a reduction in the c-axis dispersion. However, the thickness of the seed layer will contribute to the HKS. Therefore, it is necessary to reduce the non-magnetic seed layer thickness to increase the write field and gradient. In this chapter, the H-SUL structures that can support a non-magnetic intermediate layer (non-MIL) thickness of 5 nm with optimized combination of a-SUL, seed layer and c-SUL are simulated. Figure 2(c) shows the H-SUL layer structure consisting (from bottom to top) of an a-SUL, non-magnetic seed layer, c-SUL, and non-magnetic interlayer. In the H-SUL design, an amorphous layer such as CoTaZr at the bottom would provide a smooth surface and help to achieve the low noise characteristics of conventional recording media. The c-SUL, which is at the top, would contribute in the writing process as a part of a-SUL, as well as provide a growth template for the layers above it. Therefore, only 5 nm Ru_2 is needed as an exchange decoupling layer between the c-SUL and the recording layer, thereby generating less reluctance in the magnetic flux circuit. In order to provide a growth template for the CoCrPt:oxide based RL with a hcp(002) texture, the C-SUL should

have a hcp(002) or fcc(111) texture. The major feature of the C-SUL studied here is a fcc(111) texture and an in-plane anisotropy. Another feature is that the C-SUL used here has a higher permeability than that of $Co_{78}Cr_{22}$ in the previous study, thereby having the potential to improve writability.

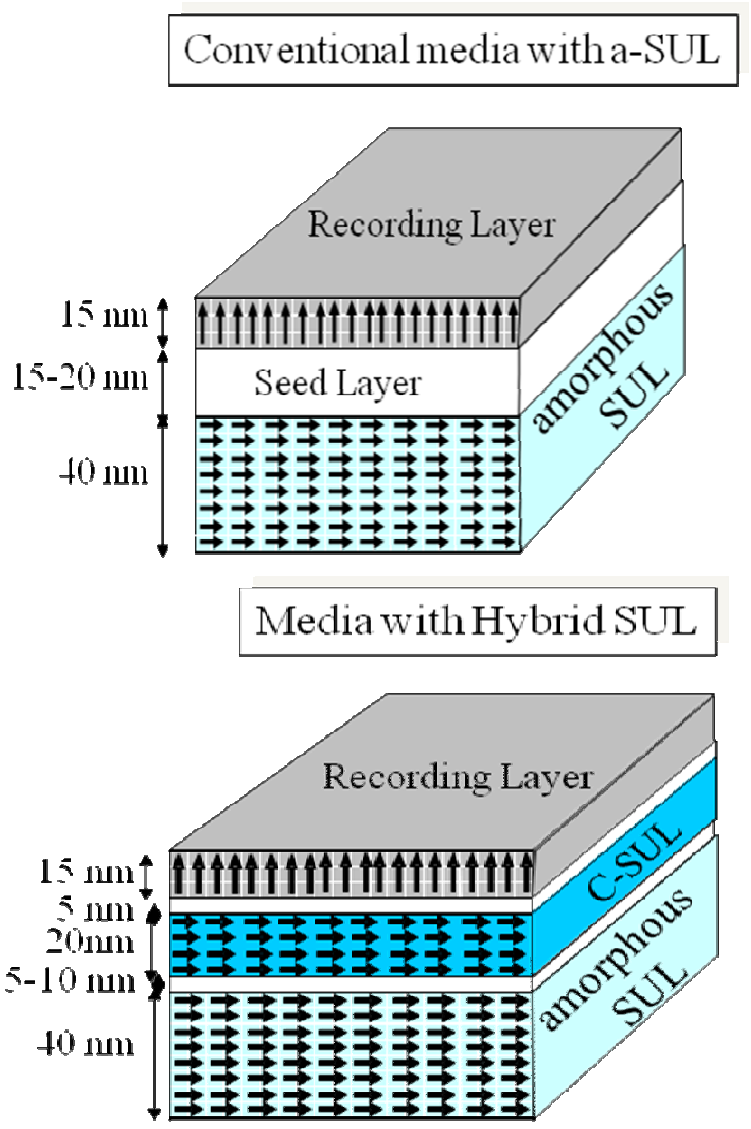

Figure 3. 1 Comparison of layer structure of perpendicular recording media using with (a) amorphous soft underlayer and (b) hybrid soft underlayer.

The simplified structures for media with a-SUL and H-SUL in the micromagnetic simulation are shown in Figs 3.2(b) and 3.2(d), respectively. For all cases, the recording

layer was 15 nm thick, and the head-media spacing was 5 nm. For media with an a-SUL, non-magnetic seed layers with thicknesses from 5 nm to 25 nm were included underneath the recording layer and above the 40 nm a-SUL. The media using H-SUL consisted of the following stack: 5 nm exchange-breaking layer underneath the recording layer, 20 nm c-SUL below it, and non-magnetic seed layers of different thickness between the c-SUL and 40 nm a-SUL. In all calculations, the recording head at the air bearing surface was 50 nm wide in the cross-track direction and 150 nm long in the down-track direction. It was centered above a section of SUL 400 nm long and 400 nm wide. In the model of the H-SUL, the saturation magnetizations of a-SUL and c-SUL were 1909.9 emu/cm^3 and 1169.8 emu/cm^3, respectively. This corresponds to a c-SUL composition of FeCoTaCr. We have assumed that the c-SUL has a single easy axis along the cross track direction with variable anisotropy field. The writer pole tip and a-SUL have uniaxial anisotropies in the cross track direction with anisotropy field of 10 Oe.

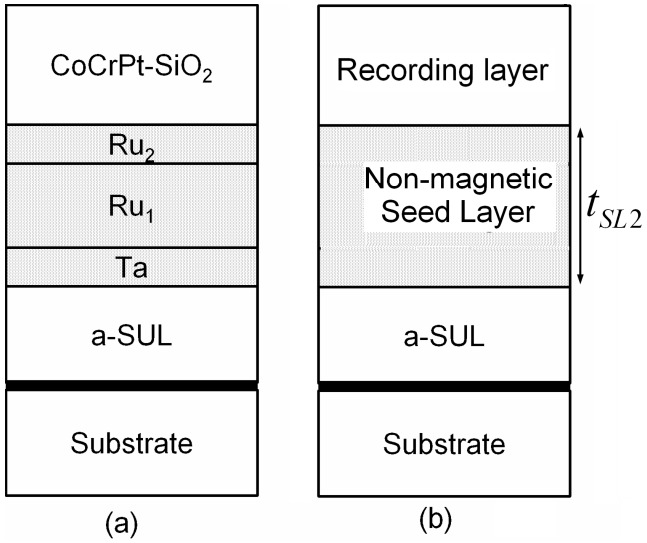

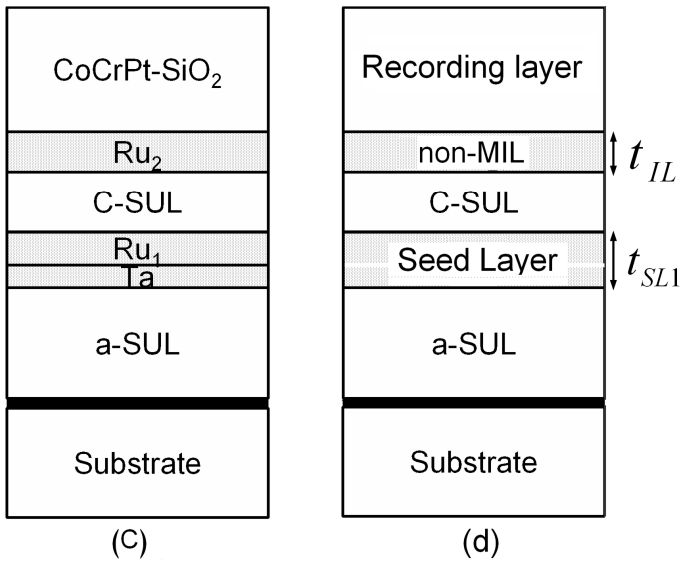

Figure 3. 2 Layer structures of perpendicular recording media with amorphous SUL (a), the model used in the micromagnetic simulation for the structure (b), the layer structure of media with hybrid SUL (c) and the model used in the micromagnetic simulation for the H-SUL (d).

3.2 Micromagnetic Simulation and Results

3.2.1 Micromagnetic modeling method

A three-dimensional micromagnetic model has been used to verify the writability improvement in the media using H-SUL in comparison with the conventional media with a-SUL. The cross-section of the layer structures in the simulation (except the single pole head) are shown in the Figs. 2(b) and 2(d), respectively. The whole structure is discretized into three dimensional cubic cells of side 20 nm and the total magnetostatic field due to the writer, a-SUL and c-SUL are calculated by solving the Landau-Lifshitz-Gilbert equation using a fourth-order Runge-Kutta method with $\Delta t = 10^{-13}$s. Each unit cell is assumed to be a single domain with coherently rotated magnetization. The total energy consists of crystalline anisotropy, magnetostatic interaction, and exchange coupling. The Stoner-Wohlfarth effective field H_{eff} and its gradient are also calculated within a reference plane (200 nm × 200 nm) at 12 nm below the air bearing surface of the head, i.e., the middle of the recording layer. For studying the effects of different underlayers on the writability, micromagnetic simulations were

performed without any recording layer.

3.2.2 Equivalent effective field and field gradient

One important task for simulation is to scan through a variety of underlayer designs to look for equivalent effective fields and field gradients. The effects of varying the seed layer thickness (t_{SL1}) and c-SUL relative permeability (μ_r) on H_{eff} and its gradient are investigated on the media with H-SUL. The relative permeability was changed by varying the anisotropic field H_k, where $\mu_r=1+4\pi M/H_k$. The conventional media with different non-magnetic seed layer thicknesses (t_{SL2}) are also analyzed and compared with the new media.

Using the micromagnetic model and media parameters in previous sections, comparative effective field and gradient in the down-track and cross-track directions are presented in Figure 3. When the μ_r is 24 and t_{SL1} is 6 nm, the effective field and field gradient in the hybrid SUL is equivalent to those in a conventional structure with non magnetic seed layer 13 nm thick. Table 2.1 shows a variety of conventional structures and H-SUL structures having equivalent effective fields and gradients with different parameters. It is noted that when t_{SL2} in conventional media is 15 nm, equivalent field and field gradient can be obtained in the hybrid SUL structure for t_{SL1} of 6 nm and 18 nm and μ_r value of 10 and 28, respectively. For t_{SL2} of 10 nm, magnetic equivalence requires a relative permeability of 38 if the thickness of a non magnetic seed layer is 18 nm. In other words, the hybrid structure can allow 43 nm of crystalline material to seed the recording layer yet be magnetically equivalent to conventional structure with 10 nm seed layer. Alternatively, if t_{SL1} is reduced to 6nm, a decreased μ_r of 30 is needed to maintain magnetic equivalence to the same conventional structure. From these results, it can be concluded that the H-SUL has more alternatives to improve the writability of perpendicular recording media. Table 2.2 shows a variety of conventional structures and H-SUL structures having equivalent perpendicular fields and gradients with different parameters. For 10 nm t_{SL2}, magnetic equivalence in terms of perpendicular field requires a μ_r of 24 if the t_{SL1} is 6 nm. The hybrid structure can allow 31 nm of crystalline material to seed the recording layer yet be magnetically equivalent to the

conventional structure with 10 nm seed layer. With a suitable combination of c-SUL permeability and seed layer thickness, the H-SUL structure can reduce the effective magnetic spacing between SUL and recording head, and maintain equivalent field and field gradient with even thicker seed layer.

3.2.3 Writability improvement

For the purpose of comparing, a relative permeability (μ_r) value of 40 and anisotropy field of 377 Oe in the cross track direction were used for the crystalline part of the H-SUL. For the media with a-SUL, a 25 nm non-magnetic seed layer underneath the recording layer was considered. For the media using H-SUL, the non-magnetic seed layer thickness was either 5 nm or 10 nm. Other parameters are listed in Section II. The calculated values of the effective field H_{eff}, and its gradient, from the different data sets, are plotted along the down-track direction in Figs. 4(a) and 4(b) respectively. H_{eff} and its gradient can be found to be enhanced along the down track length for the media using H-SUL and the maximum effective field is over 1 kOe larger at the center of the track, than that for media using only a-SUL. These results indicate the effectiveness of replacing a part of the non-magnetic intermediate layer with a magnetic material to improve writability. While it is difficult to reduce the seed layer thickness on a-SUL, H-SUL design provides more flexibility to improve textured growth and writability simultaneously. For the purpose of comparing writability in term of perpendicular field, we found that the maximum perpendicular fields along the down track and cross track direction are enhanced from 10kOe to 12kOe, i.e., about 20% increase, as shown in Fig. 5(a) and (b).

3.2.4 Effective field and gradient with different seed layer thickness

Results in Figure 4 also show that H_{eff} is different for the H-SUL structure using a 10 nm non-magnetic seed layer compared to the H-SUL structure using a 5 nm seed layer. The simulation results show that for the H-SUL with a 5 nm non-magnetic seed

layer, the perpendicular field H_z under the writing pole is about 3% larger than the field for a 10 nm seed layer. The reduction of H_z results from an increased magnetic reluctance of the H-SUL with an increased thickness of the non-magnetic seed layer. This result also means that the presence of a non-magnetic seed layer will reduce the overall permeability of the H-SUL which is no longer a perfectly permeable "keeper", thereby increasing the tangential components of the total field. While the total and perpendicular fields were larger for the H-SUL with 5 nm seed layer than 10 nm seed layer, the comparative results between these two cases in Fig. 4(a) indicate that the effective field with thinner non-magnetic seed layer is not always larger than that with thicker seed layer over the entire track. This is due to the angular dependence of the effective write field H_{eff}, which is given by

$$H_{\text{eff}} = \left[\left(H_{\text{x}}^2 + H_{\text{y}}^2 \right)^{1/3} + H_{\text{z}}^{2/3} \right]^{3/2} = H_{\text{tot}} \left[\left(\cos\theta \right)^{2/3} + \left(\sin\theta \right)^{2/3} \right]^{3/2} \tag{3.1}$$

where $H_{\text{tot}} = \left(H_x^2 + H_y^2 + H_z^2 \right)^{1/2}$, x and y are the down track and cross track directions, respectively, and θ is the angle of the total field with respect to the perpendicular direction. H_{tot} is a vector sum of all contributions in x, y and z directions. From Eqn.(3.1), the angular variation of the effective field is symmetric with respect to 45°where H_{eff} reaches its peak value. The larger H_{eff} for the 10 nm case in some regions represents the influence of the tangential field in advancing θ closer to a value of 45˚, where the effective field is enhanced.

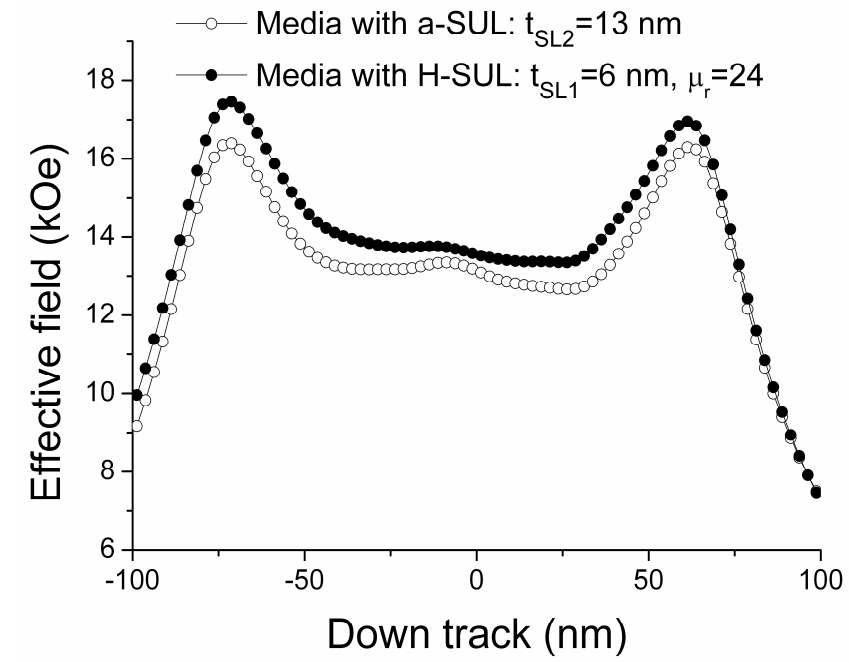
Media with a-SUL: t_{SL2}=13 nm
Media with H-SUL: t_{SL1}=6 nm, μ_r=24
Effective field (kOe)
18
16
14
12
10
8
6
-100
-50
0
50
100
Down track (nm)

(a)

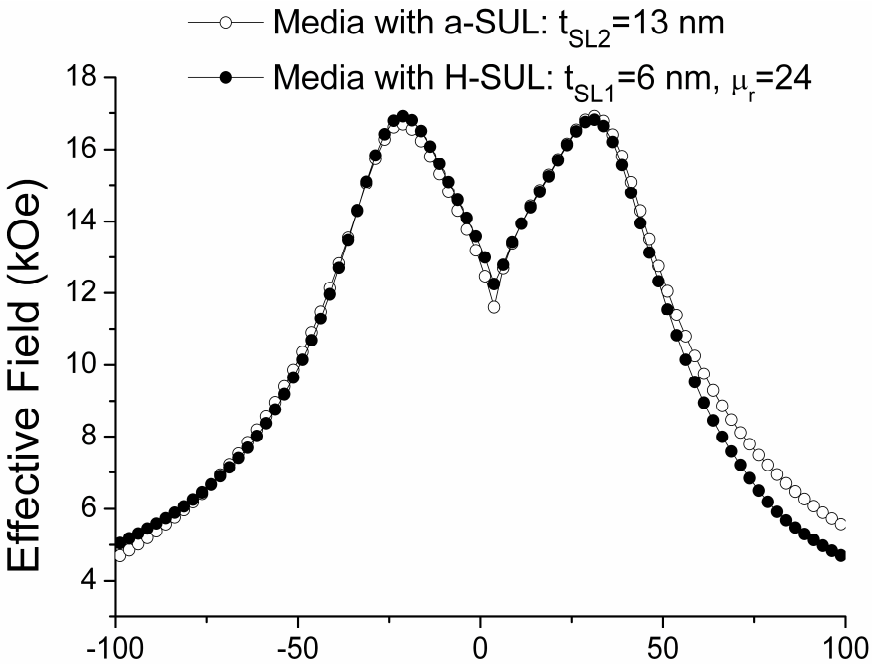
Media with a-SUL: t_{SL2}=13 nm
Media with H-SUL: t_{SL1}=6 nm, μ_r=24
Effective Field (kOe)
18
16
14
12
10
8
6
4
-100
-50
0
50
100
Cross-track (nm)

(b)

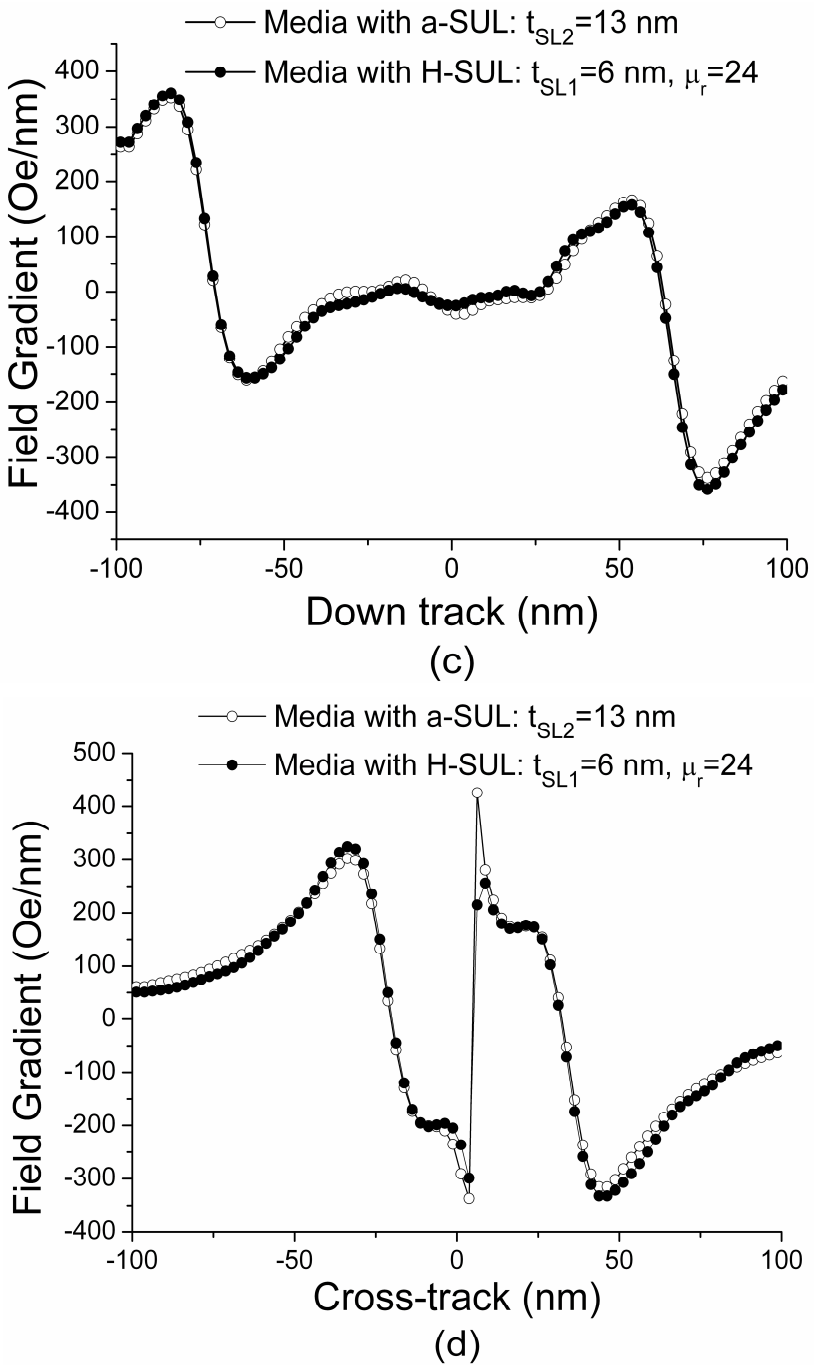

Figure 3. 3 Comparison of effective fields in (a) down track and (b) cross track directions and effective field gradients in (c) down track and (d) cross track directions for conventional media with a-SUL and the media with H-SUL. The thickness of amorphous SUL in both media is 40 nm, and the crystalline SUL thickness is 20 nm.

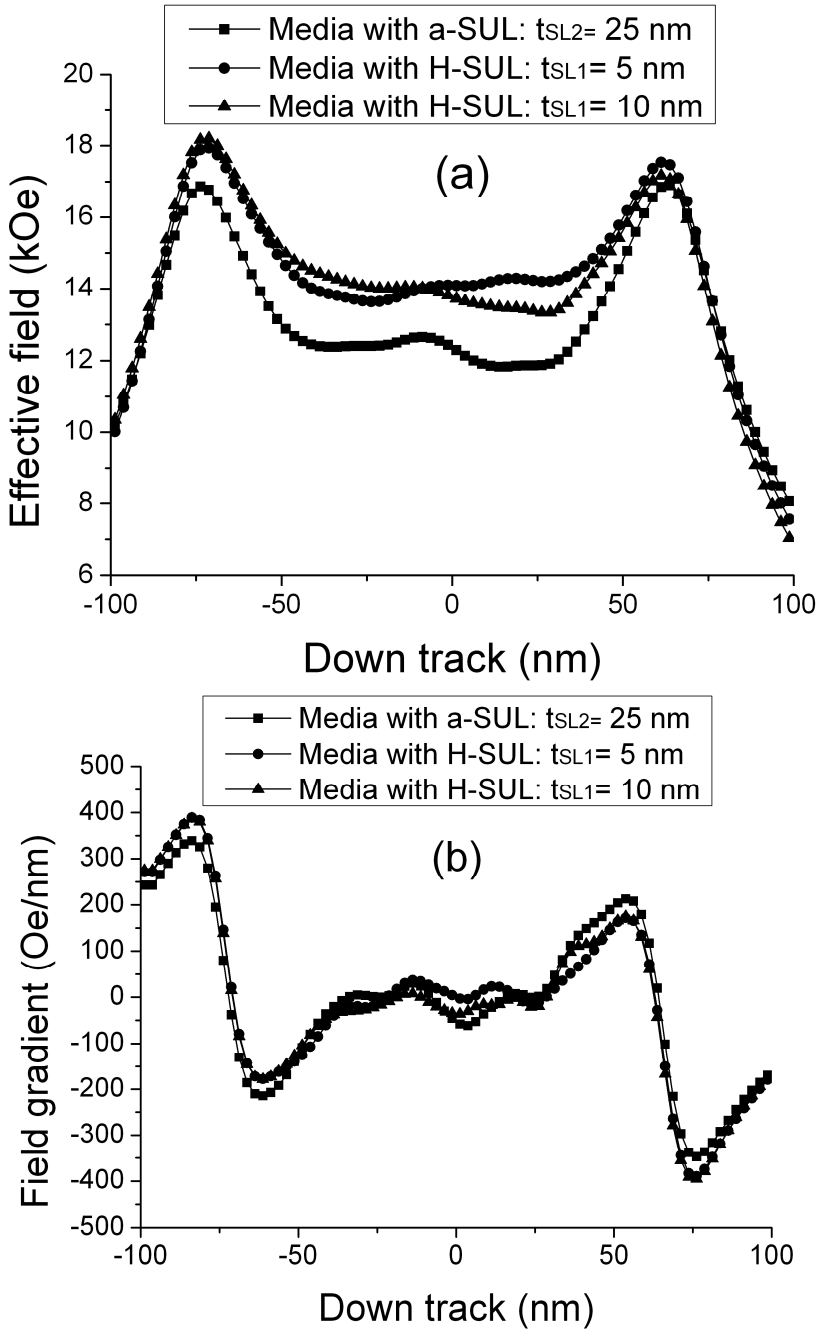

Figure 3. 4 (a) Comparison of effective field and (b) effective field gradient in down track direction for conventional media using a-SUL and non-magnetic seed layer thickness of 25 nm and the media with H-SUL using non-magnetic seed layer thickness of either 5 nm or 10 nm.

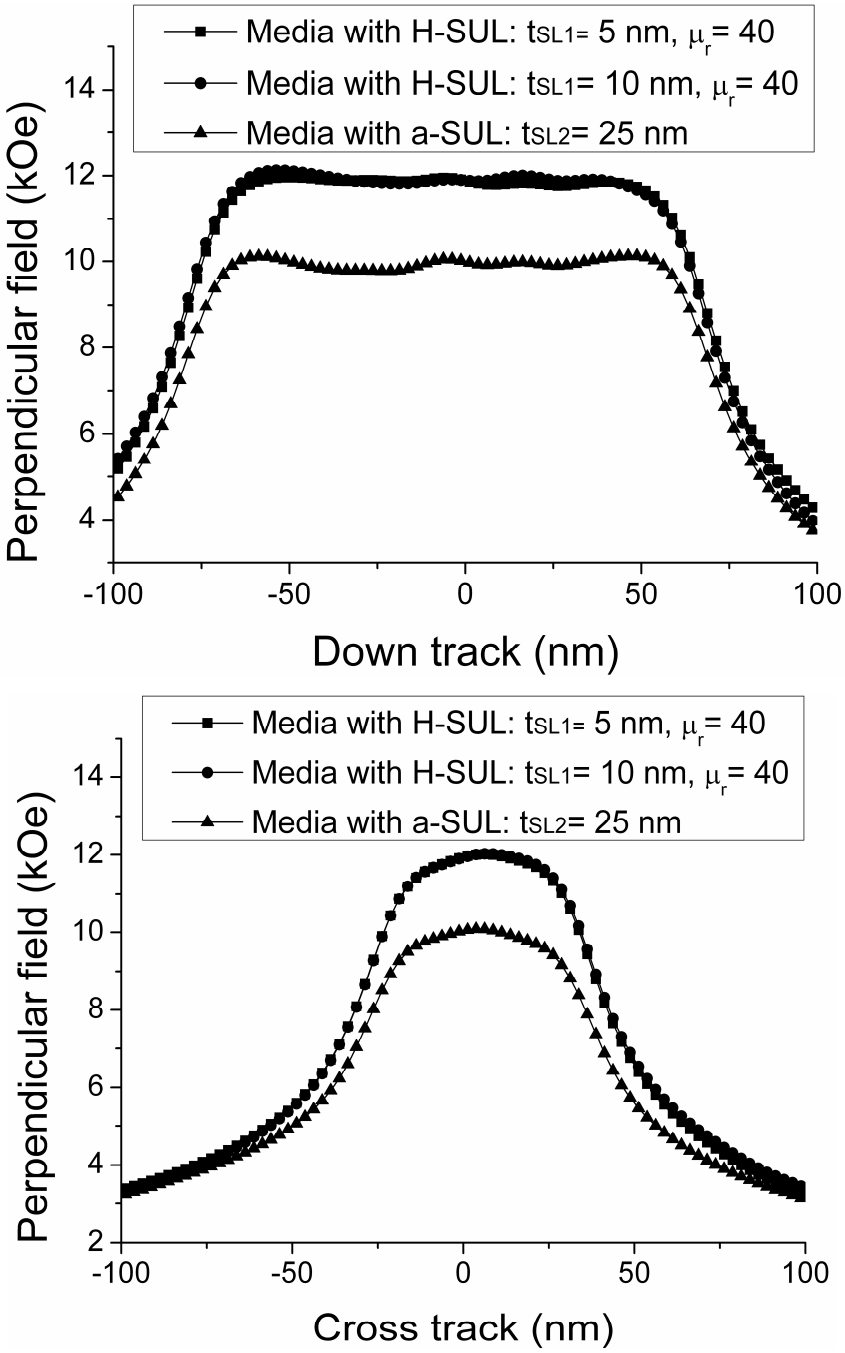

Figure 3. 5 Comparison of perpendicular field along (a) down track and (b) cross track direction for conventional media using a-SUL and non-magnetic seed layer thickness of 25 nm and the media with H-SUL using non-magnetic seed layer thickness of either 5 nm or 10 nm.

Media with a-SUL	Media with H-SUL	
SL thickness t_{SL2} (nm)	μ_r of crystalline SUL	Seed layer thickness t_{SL1} (nm)
10	30	6
11	26	
13	24	
15	10	
10	34	12
11	36	
13	30	
15	28	
10	38	18
11	36	
13	34	
15	28	

Table 2. 1 A variety of media structures using a-SUL and H-SUL with equivalent effective fields and field gradients

Media with a-SUL	Media with H-SUL	
SL thickness t_{SL2} (nm)	μ_r of crystalline SUL	Seed layer thickness t_{SL1} (nm)
10	24	6
11	20	
13	6	
15	5	
10	40	12
11	36	
13	6	
15	6	
10	40	18
11	38	
13	8	
15	6	

Table 2. 2 A variety of media structures using a-SUL and H-SUL with equivalent Perpendicular fields and field gradients

3.3 Conclusion

In this chapter, micromagnetic simulation studies were performed to verify the writability improvement in the media using H-SUL and compare to conventional media with an a-SUL. Simulation results show that a suitable combination of crystalline SUL permeability and seed layer thickness in H-SUL structure can generate equivalent or better effective fields and gradients over those in conventional media, by reducing the effective magnetic spacing between SUL and recording head. Alternatively, H-SUL can support a thicker seed layer to maintain equivalent field and field gradient by replacing a part of the non-magnetic intermediate layer with a magnetic material to improve writability and texture growth.

Chapter 4 Micromagnetic Study of Noise Plateau

Noise in magnetic recording arises from three predominant sources: the playback amplifier, the playback head and the recording medium. Amplifier noise depends on current or voltage noise sources. Head noise arises from the loss impedance of the head due to the complex part of the permeability. In this chapter, the discussion will focus on the medium noise. Calculations of the power spectral density, the predominant medium noise mechanism and a puzzling medium noise phenomenon will be presented.

In perpendicular magnetic recording, medium noise is one of the crucial impediments to obtaining high areal density. Medium noise at a given location in the magnetic recording system depends strongly on the local granular structure of the medium [4.1]. Medium noise can be considered a statistically random variable associated with the random component of the magnetization pattern recorded on the medium as caused by a spatially random property of the medium [4.2]. Medium noise is known as a key factor in degrading the bit-error rate (BER) performance of the recording systems in both longitudinal and perpendicular magnetic recording. It has been experimentally demonstrated by Belk, et al. that [4.3] noise power in longitudinal magnetic recording increases linearly for low recording density and increases superlinearly at higher recording density. Madrid, et al. proposed that [4.4] the linear increase was due to the uncorrelated transition shift at low linear densities and argued that the superlinear increase corresponds to the negative correlation between adjacent transitions. Negative correlation occurs when adjacent transitions shift in opposite direction.

4.1 The puzzling phenomenon of medium noise

This chapter focuses on the transition noise characteristics in a perpendicular magnetic recording system using micromagnetic simulation. In contrast to longitudinal recording, the direction of the transition location shift is different: proximity of the previous transition has the effect of shifting the current transition towards the previous transition for longitudinal recording, while in perpendicular recording the shift is away

from the previous transition [4.5][4.6][4.7]. As shown in Fig. 4.1, there is a noise plateau phenomena in perpendicular recording: for low to moderate recording density the noise power increases linearly, but as the density continues to increase the noise power tends to saturate over a range of intermediate recording densities.

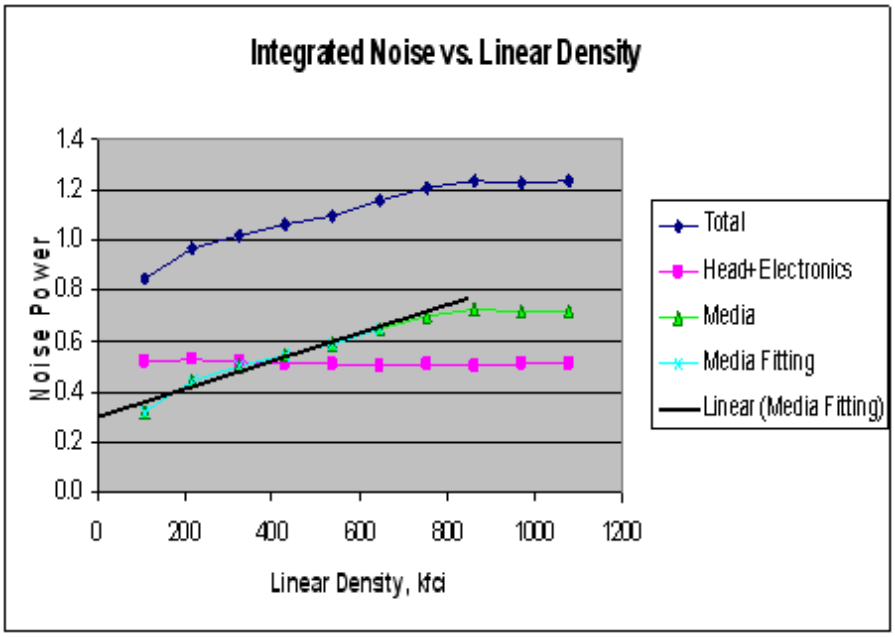

Figure 4. 1 Experimental results show that integrated media noise power saturates beyond a breakpoint. (Figure courtesy T. Arnoldussen)

For the purpose of understanding this puzzling noise plateau and its relation to the correlation of position jitter, this chapter calculates the integrated total noise power and the corresponding transition jitters at a variety of linear densities, using a scheme of single-pole head and perpendicular medium with soft underlayer. In the following sections, micromagnetic simulation details are described including a read back process using the reciprocity principle. A discussion of the relationship between jitter correlation, noise, and Non-Linear Transition Shift (NLTS) is provided in Section 4.4. In Section 4.5, results from micromagnetic simulations of the noise and jitter are presented.

4.2 Magnetic writing process and readback simulation

In order to establish the relationship between the position jitter and the granular structure of the medium, as well as the magnetostatic interaction from the neighboring transitions, numerical micromagnetic simulation is utilized based on the Laudau-Lifshitz-Gilbert (LLG) equation. Using frequency-domain analysis, the noise characteristics of the read back voltage from a combined perpendicular recording layer, soft underlayer, and shielded MR read head are investigated.

A realistic grain configuration formed by planar Voronoi cells that represent actual grain shapes was utilized to simulate the perpendicular recording medium with soft underlayer. Each grain is assumed to be a single domain with uniaxial anisotropy. The orientation dispersion of the easy axis in the medium was assumed to have a Gaussian distribution with a standard deviation of 5º. The K_u of the recording layer was 3.6×10^6 erg/cm^3. Voronoi cells with average grain diameter of 9 nm, grain boundary of 0.5 nm, and standard deviation of 1.8 nm were used. The intergranular exchange coupling constant was set to be zero. The total field consists of anisotropy field, magnetostatic interaction field, exchange coupling field and the write head field. The magnetostatic interaction tensor between two grains was calculated by using a geometric mapping technique [4.8]. A periodic boundary condition was used in the Voronoi cells to avoid spurious boundary effects. The LLG equation was solving using the fourth-order Runge-Kutta method. In our simulation, a damping constant α of 0.1 and a time step of 1.0×10^{-13} s were employed. For the single-pole head (SPH), the write down-track and cross-track width were 100 nm and 80 nm, respectively. Magnetic separation between the single-pole head and the recording layer was set to be 10 nm. For the recording layer, the thickness was fixed at 20 nm. Saturation magnetization M_s is 600 emu/cm^3. The thickness of the nonmagnetic interlayer (seed layer) is set to be 20 nm. The simulated region of the recording layer is 700 nm in the down track direction and 120 nm in the cross track direction. For the shielded magnetoresistive (MR) head, the shield-to-shield spacing is 53 nm, and the element thickness is 5 nm. The head/disk velocity is set to be 12m/s. Read head widths of 60-80 nm were considered. The soft underlayer is assumed to have infinite permeability with perfect imaging.

Here, we present the results of recording simulations. Fig. 4.2 shows the magnetization pattern obtained when square waves were recorded at a linear density of 725 kfci (bitlength of 35 nm). Twenty transitions are shown in this sample: the simulation was repeated on an identical medium, but at different starting points to obtain the approximately 200 transitions necessary for statistical accuracy. A reasonable estimate of the signal was obtained by averaging the noise contaminated waveforms. Then, the noisy waveform fluctuations can be obtained by subtracting this ensemble-averaged signal from the individual noise-contaminated waveforms. Significant track curvature and ac-erased noise at the track edge are observed, but results were analyzed over a width of 60 nm to determine the average magnetization pattern and thus standard deviation of position jitter σ_x^2.

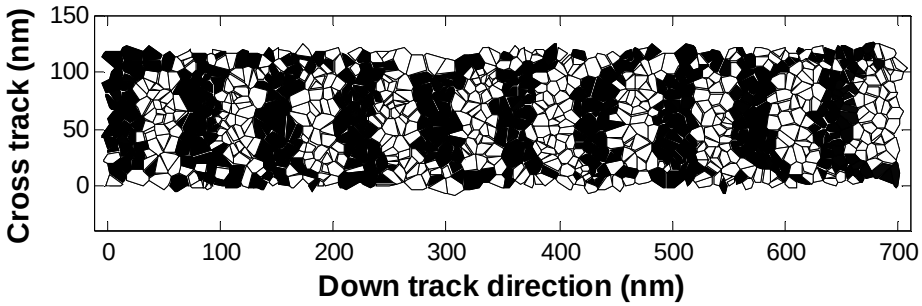

Figure 4. 2 Simulated square-wave magnetization pattern at a linear density of 725kfci.

The reciprocity principle [4.9] was used to calculate the read back voltage. Therefore the imaginary head field generated by the read head is required. The three-dimensional Laplace equation with boundary conditions of zero potential in the SUL and shields, and unit potential in the MR element, is solved. The three-dimensional finite difference (3-D FD) method is used to calculate the magnetic potential distribution around the head/ medium space, which is essential for obtaining the two-dimensional read back voltage distribution. Figure 4.3 shows the magnetic potential calculated at the center of recording layer.

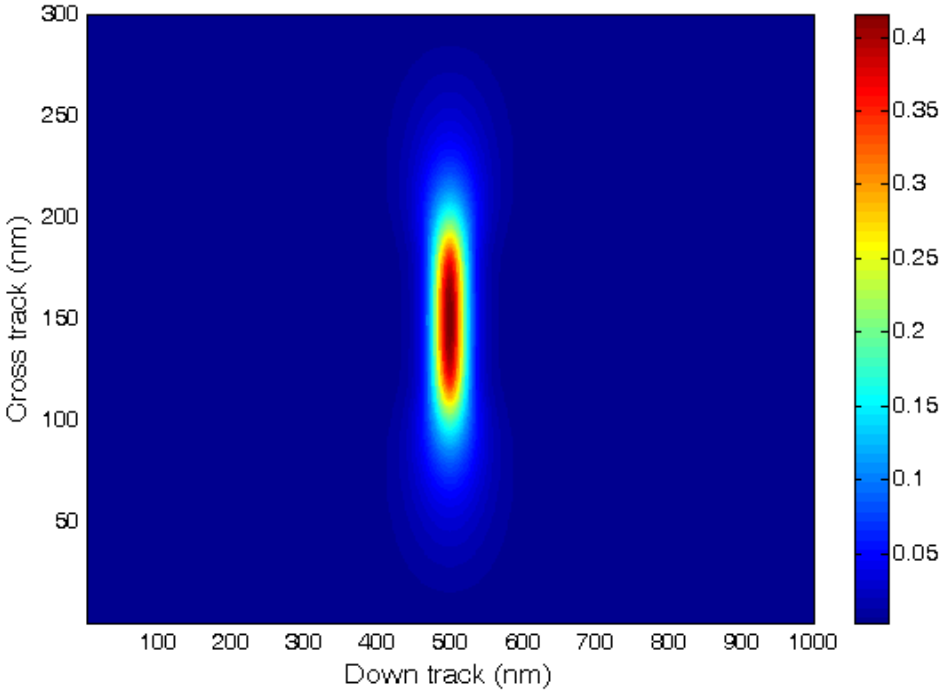

Figure 4. 3 Magnetic potential at the center of recording layer.

The imaginary head field can be written in terms of the gradient of a scalar magnetic head potential: $\overrightarrow{H} = -\nabla \Phi_{MR}$. The read back voltage can be expressed as [4.9]:

$$V_{MR} = \frac{2\Delta\rho J E_{MR} \langle \sin\theta_0 \rangle}{tM_s} \int_{vol} \Phi_{MR}\left(\vec{r}' + x\vec{x}\right) \rho^{rec}\left(\vec{r}'\right) d^3 r' \qquad (1)$$

Where J is the current density, E_{MR} is the efficiency of the head, $\Delta\rho$ is the element resistance change between the parallel and perpendicular directions, $\langle \sin\theta_0 \rangle$ is the average bias orientation distribution of the MR element magnetization, M_s is the MR element magnetization, ρ is the surface charge density given by the dot product of the medium magnetization with its surface normal, and t is MR thickness. From Eqn. (1), the MR read back voltage thus depends on the magnetization variations or "poles" in the recorded medium.

4.3 Medium noise mechanisms and calculation

The playback noise arises from the medium magnetization variation and the electronic noise in the MR sensor and the preamp circuits. While the electronic noise with a white noise spectrum can be neglected, in high density recording, the transition and the DC remanent noises are dominant. Medium noise arises from fluctuations in the medium magnetization. Transition noise refers, in general, to fluctuations that are concentrated near the recorded transition centers. The track-width averaged magnetization pattern is considered as playback signal. The average magnetization is obtained by summing M(x,z) at every recording wavelength λ. SNR is defined as a ratio of peak to peak signal amplitude and root mean square (RMS) noise voltage at each density. The average magnetization and the playback voltage can be expressed as:

$$\begin{aligned}
\left\langle \overset{\rho}{M}(x,y,z) \right\rangle &= \frac{1}{2N+1} \sum_{n=-N}^{N} \overset{\rho}{M}(x+n\lambda, y, z), \quad 0 \le x \le \lambda \\
V_y(x,y) &= \frac{V_0}{WL} \int_{-W/2}^{W/2} \int_{-L/2}^{L/2} h_y(x+x_1, y, z) \left\langle M_y(x_1, y, z) \right\rangle dx_1 dz \\
&= \frac{V_0}{WLt} \int_{-t/2}^{t/2} dy \int_{-W/2}^{W/2} dz \int_{-L/2}^{L/2} h_y(x+x_1, y, z) \left\langle M_y(x_1, y, z) \right\rangle dx_1 \\
&= \frac{V_0}{WLt} \iiint_{medium} d^3 r_1 \; h_y(x+x_1, y, z) \left\langle M_y(x_1, y, z) \right\rangle
\end{aligned}$$

(4.1)

where x is downtrack direction, y is perpendicular direction and z is crosstrack direction, respectively. W is the cross track width, L is the medium length and t is the medium thickness.

The root mean square (RMS) noise voltage can be expressed as:

$$\begin{aligned}
\Delta V^2(x) = \left\langle V^2(x) \right\rangle - \left\langle V(x) \right\rangle^2 &= {V_0}^2 \iint h_y(x+x_1, y) h_y(x+x_2, y) \times \\
&\sum_{z_1, z_2} \left\{ \left\langle M_y(x_1, z_1) M_y(x_2, z_2) \right\rangle - \left\langle M_y(x_1, z_1) \right\rangle \left\langle M_y(x_2, z_2) \right\rangle \right\} dx_1 dx_2
\end{aligned}$$

(4.2)

4.4 Analysis of transition jitter and Non-linear Transition Shift

Eqn. (12.12) of [4.9] shows that, when neglecting the correlations between jitter in different transitions as usually considered in the isolated transition or linear superposition assumption, both power spectra density and total noise power increase linearly with the jitter variance and the recorded density (1/B). In high density recording, however, nonlinearities from interbit magnetostatic interactions can cause jitter correlations and therefore violate the linear superposition assumption. Recall that [4.9], nonlinear transition shift (NLTS) is the change in transition position caused by magnetostatic field from previously written transition. Fig. 4.4 shows a sketch of the writing of a current transition in the presence of a previous transition separated by bit spacing B. The transition location center of the current transition is given by: $H_c(x)= H_d(x)+ H_{head}(x)$ where H_d is the demagnetizing field from the previous transition, H_{head} is head field and H_c is medium coercivity. Assuming no transitions before 1, transition 1 will experience larger demagnetizing field and thus cause a larger shift than transition 2, i.e. $\Delta 1'1 > \Delta 2'2$. NLTS effect occurs when proximity of the previous transition tends to shift the current transition away from transitions, i.e. B'>B.

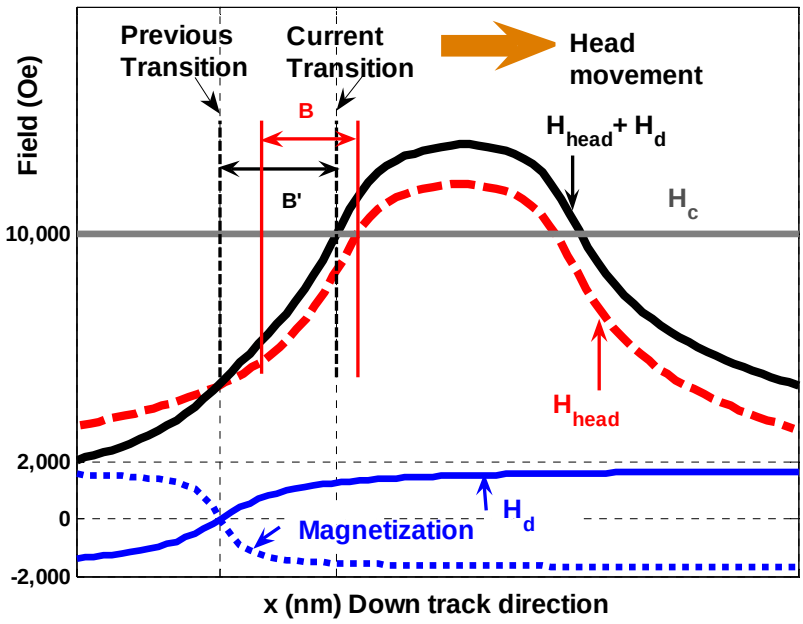

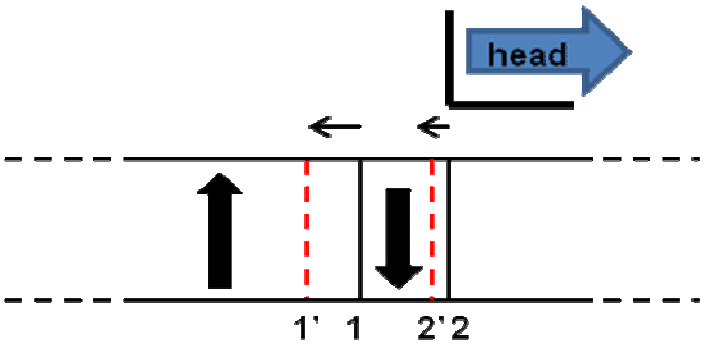

Figure 4. 4 Schematic illustration of non-linear transition shift.

A similar analytical argument is provided for both longitudinal and perpendicular recording. For the case of two transitions in the presence of magnetostatic interactions, the transition center location of the second transition is given by

$$\begin{aligned} H_c &= H_d\left(\left(x_2+\Delta x_2\right)-\left(x_1+\Delta x_1\right)\right)+H^h\left(x_2+\Delta x_2\right) \\ &\approx H_d\left(x_2-x_1\right)+\Delta H_d+H^h\left(x_2\right)+\frac{\partial H^h\left(x_2\right)}{\partial x}\Delta x_2 \end{aligned} \tag{4.3}$$

where x_1 and x_2 are the intended position of current and previous transitions, and Δx_1, Δx_2 are the transition position jitters for the current and previous transitions, respectively. In eqn. (4.3), H_c is the medium coercivity. The first term on the right hand side of equation is the demagnetizing field in a recording layer with a single transition located at $x_1' = \left(x_1+\Delta x_1\right)$ evaluated at the current transition position $x_2' = \left(x_2+\Delta x_2\right)$. The second term is the head field evaluated at the current transition position $x_2' = \left(x_2+\Delta x_2\right)$. Considering a small jitter ($|\Delta x/x| << 1$), and that $H_c = H_d\left(x_2-x_1\right)+H^h\left(x_2\right)$, solution of eqn. (4.3) produces Δx_2:

$$\Delta x_2 = -\frac{\Delta H_d}{\frac{\partial H^h\left(x_2\right)}{\partial x}} \tag{4.4}$$

ΔH_d is the change of demagnetizing field associated only with position jitter and

$\frac{\partial H^h(x_2)}{\partial x}$ is the head field gradient evaluated at the current intended transition. Using a charge sheet model [4.9] and a perfect arctangent magnetization transition, the demagnetizing field in longitudinal and perpendicular media can be shown in Figure 4.5 and Figure 4.6, respectively. Detailed discussion can be found in [4.9]. The plots show that both demagnetizing fields vanish at the transition center. The longitudinal field peaks in the vicinity of the transition before vanishing far from the previous transition. The perpendicular field, however, increases to a maximum $\pm M_r$ far from the transition, which is opposite to the case of longitudinal field. A similar type of argument has been previously employed [4.5] to explain the Non-Linear Transition Shift of the recorded signal in perpendicular recording.

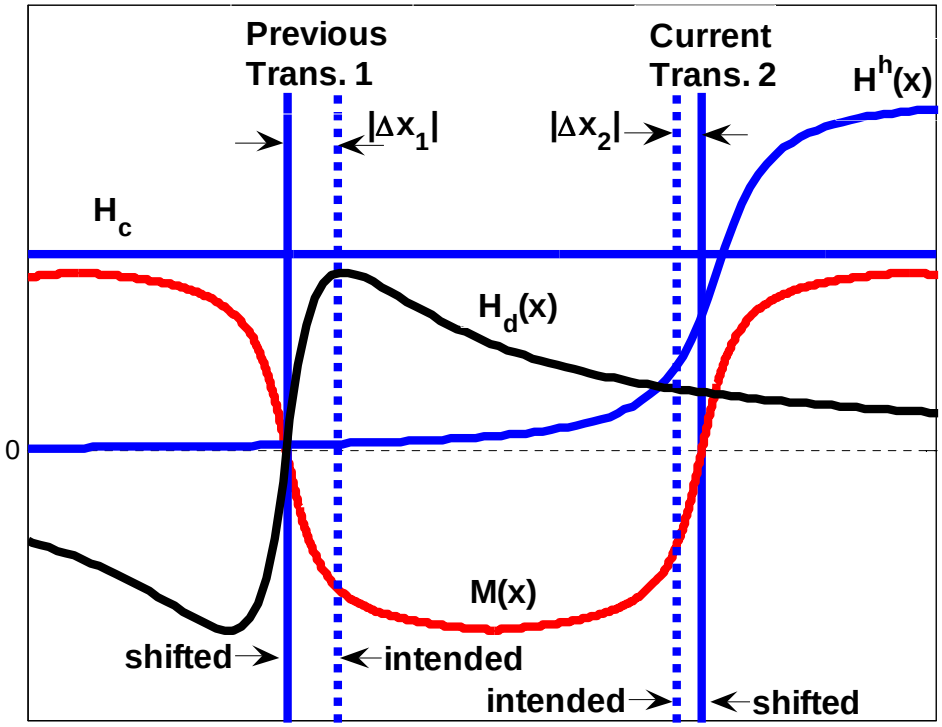

Figure 4. 5 Effect of adjacent transition on longitudinal recording.

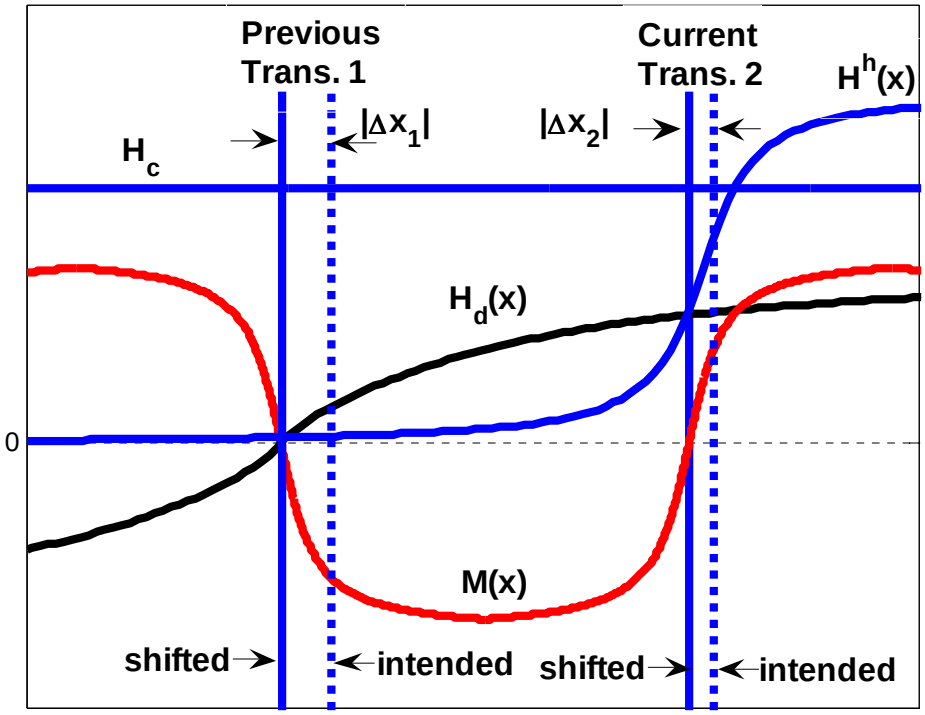

Figure 4. 6 Effect of adjacent transition on perpendicular recording.

Fig. 4.7 shows the effect of the demagnetizing field of a previous transition on the position of the intended transition in longitudinal and perpendicular recording. Since the medium has been recorded with square wave of bitlength B, if there is no jitter in the present transitions, the next transition will be pulled towards the previous transition by the proper amount. In other word, demagnetization fields will not contribute to jitter in the position of the next transition.

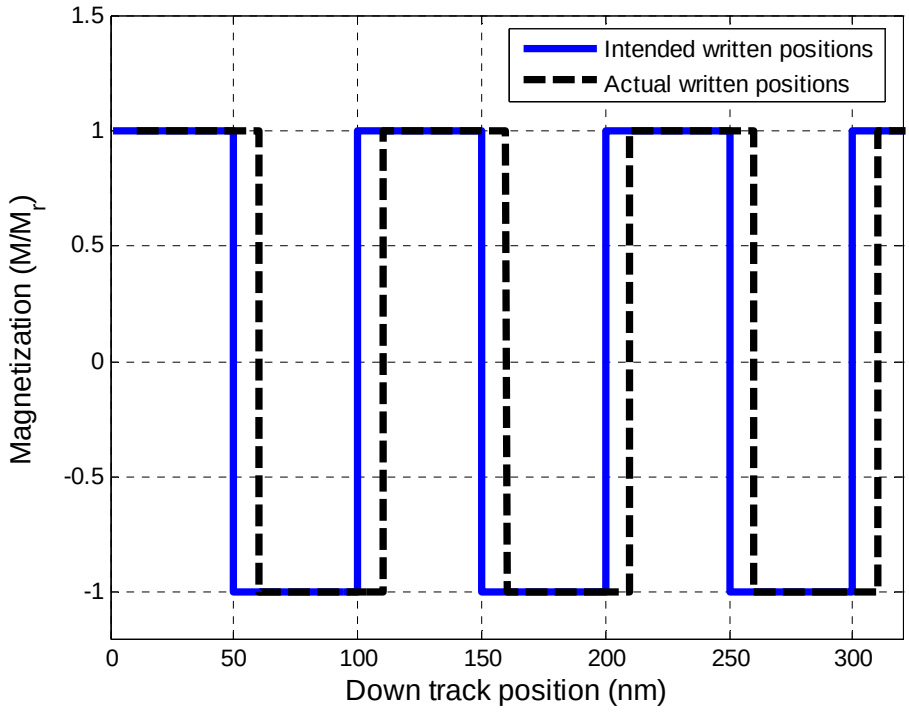

Figure 4. 7 Consider a square wave recording with very weak head field: each transition will be pulled in the same direction by approximately the same amount.

For the longitudinal case, assume that there is a jitter, Δx_n at the n_{th} transition. If this transition has been recorded before its nominal position, i.e., $\Delta x_n < 0$, the strength of the demagnetizing field at the subsequent nominal position would be weaker than if the first transition had been written in the proper location. Therefore, the subsequent transition is pulled a smaller distance towards the previous transition. Thus, as shown in Fig. 4.5, $\Delta x_n < 0$ usually results in $\Delta x_{n+1} > 0$, i.e., an opposite sign from the previous jitter, indicating a negative correlation between the neighboring transitions in square wave recording. This negative correlation between the jitter on adjacent transitions leads to additional medium noise at higher recording densities. This means that the negative jitter correlation in longitudinal recording leads to a superlinear noise performance as observed by early experimental measurement [4.3][4.4].

For the perpendicular case, however, the jitter correlation is quite different. If the

n_{th} transition has been recorded before its nominal position, i.e., $\Delta x_n < 0$, the field strength in the presence of this transition, as observed at the subsequent nominal position, is larger than it would be if the transition had been written at its nominal position. Therefore, the subsequent transition is pulled a larger distance towards the previous transition. Thus, as shown in Fig. 4.6, if $\Delta x_n < 0$, then it is likely that $\Delta x_{n+1} < 0$, and also likely that $|\Delta x_{n+1} - \Delta x_n| < |\Delta x_n|$. In other words, the adjacent jitters have the same sign, which implies that the variance of their difference is reduced. A positive jitter correlation and reduced variance in jitter between adjacent transitions in perpendicular media lead to a negative noise correlation. Accordingly, some interesting noise behavior at high density occurs such as the noise plateau phenomena that we report in this paper.

4.5 Analysis of media noise power vs. Linear Density

Fig. 4.8 shows the calculated noise power versus linear density for zero intergranular exchange coupling and medium magnetization of 600 emu/cm^3, using a read head width of 80 nm. Three additional samplings are included at bit lengths of 30, 32, and 25 nm to show that the reported noise plateau result is statistically significant. For low (~254 kfci) to moderate linear density (~635 kfci), the noise increases linearly, as expected if transition noise is the dominant component of the total medium noise. The noise then saturates between 800 and 1100 kfci, thus forming the noise plateau. In this region, the magnetostatic effect of the neighboring transition varies strongly with bit length and thus positively correlates the jitter of neighboring transitions. This implies a negative correlation in the noise, which is observed as a reduction in noise per transition. Finally, at very high density, percolation through the bit causes a large increase in noise.

Fig. 4.8 also shows the comparison of noise power versus linear density with two different values of intergranular exchange coupling constant J_{ex}. Using the same definition of J_{ex} as in Ref. [4.10], the exchange coupling energy across a grain boundary is proportional to the area between the two adjacent grains. Note that the noise level increases for increased J_{ex} but the noise plateau remains.

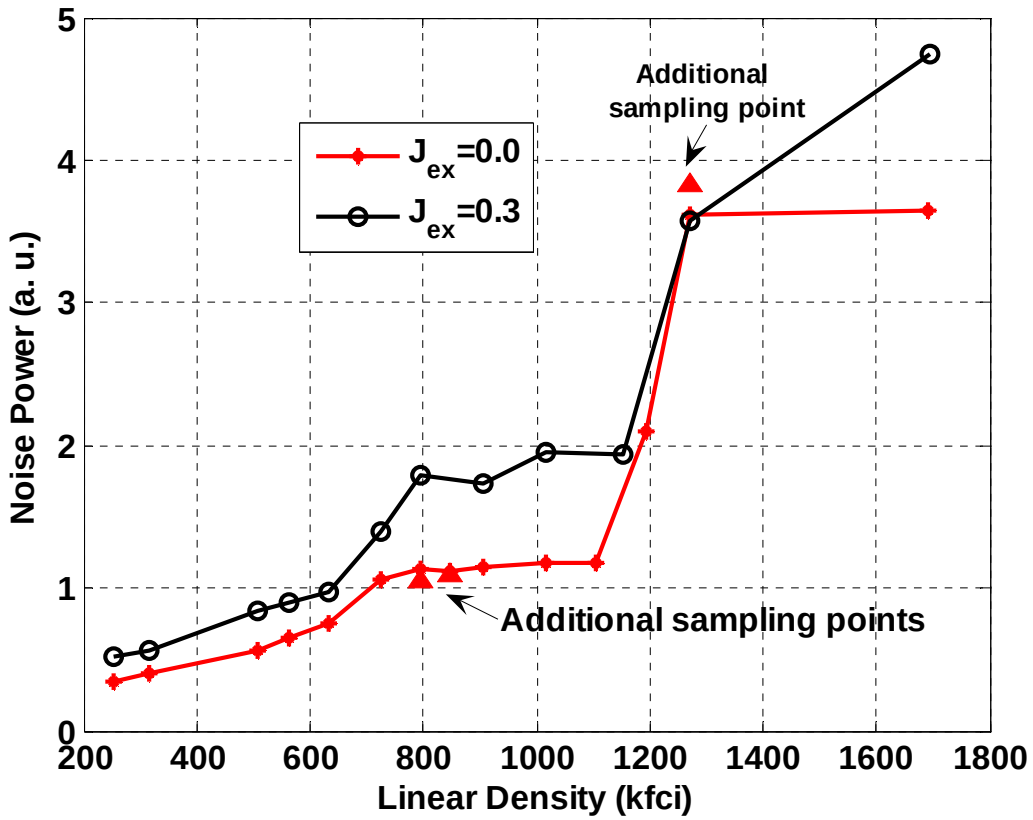

Figure 4. 8 The total integrated noise power versus linear density using an 80 nm-width read head with intergranular exchange coupling J_{ex}=0 and J_{ex}=0.3. Additional sampling points (marked by Δ) are provided at bit lengths of 20, 30, and 32 nm.

Our argument implies that the standard deviation of bit lengths, σ_B, as opposed to jitter of transition positions, should decrease as the plateau is traversed. Note that σ_B reflects the correlation in jitter. Table 4.1 shows σ_B for bit lengths of 40 nm (low density side of plateau) to 25 nm (high density side of plateau). Clearly, from 40 nm to 25 nm, σ_B^2 decreases by about 12% as the density increases for the case of high magnetization. In contrast, the low magnetization medium shows a much smaller effect of 3% that is comparable to our estimated error for predictions of variance. This low value would be expected based on arguments presented in the previous section. Note that the overall decrease in σ_B for the low magnetization case relative to the normal magnetization case is caused by the reduction in magnetostatic fields generated by the medium outside the

written track.

B (nm)	$\sigma_B^2\ (\mathrm{nm}^2)$ M_r=600emu/cm^3	$\sigma_B^2\ (\mathrm{nm}^2)$ M_r=50emu/cm^3
40	4.97	3.94
35	4.70	4.08
25	4.36	3.81

Table 4. 1 Dependence of Bitlength Variance on Bitlength and Magnetization

Fig. 4.9 shows the comparison of noise power versus linear density for medium magnetizations of 600 emu/cm^3 (left y-axis) and 50 emu/cm^3 (right y-axis) using a 60nm-width read back. The anisotropy field H_k remains the same for both medium magnetizations. The noise plateau over the range of 635 kfci to 1016 kfci can also be observed for the 600 emu/cm^3 case. For the 50 emu/cm^3 case, however, noise tends to increase linearly over a range of 317 kfci to 1270 kfci without appearance of a plateau. (Due to the reduced M_r, the noise power is reduced by a factor of 144.) The reduced magnetostatic interaction from the decreased medium magnetization makes the jitter from adjacent transitions essentially uncorrelated, thus producing a linear noise region. Finally, the observation of similar noise plateaus at different read widths (60 and 80 nm) is interpreted as evidence that side reading of the guard band is not responsible for the observed effects.

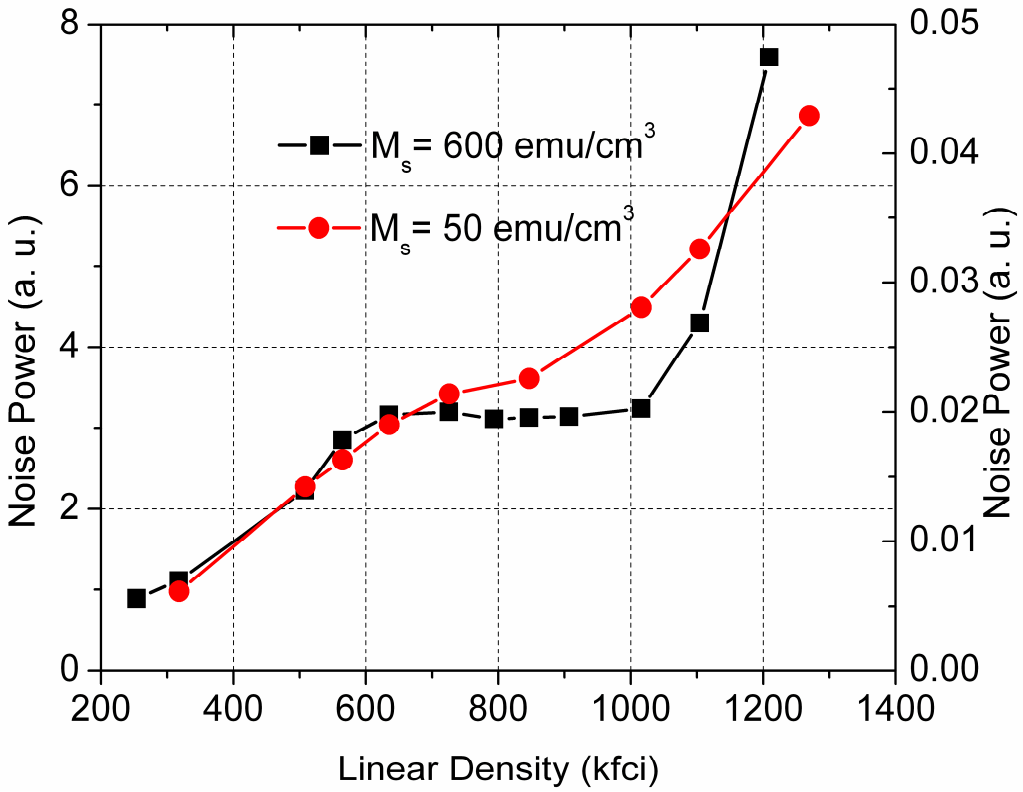

Figure 4. 9 The total integrated noise power versus linear density for two medium magnetizations 600 emu/cm3 and 50 emu/cm3 using a 60 nm-width read head.

4.6 Conclusion

Micromagnetic simulations have been performed to calculate the transition noise power and position jitter for different medium magnetizations with various linear densities. A notable result is that, in perpendicular magnetic recording, medium noise exhibits a noise plateau over a range of intermediate recording densities that is at least partly attributed to non-linear transition shift producing a positive jitter correlation. This is unlike longitudinal recording where a negative jitter correlation leads to a super-linear noise region. It is further shown that the noise plateau is not caused by a particular value of intergranular exchange or by excessive side read of noise from the guard band. Instead, an analytic argument shows that the observed effect is consistent with expected magnetostatic interactions.

Chapter 5 Extracting Intergranular Exchange Coupling for Perpendicular Recording Media

5. 1 Methods for characterization of perpendicular media

The quality of perpendicular magnetic media depends crucially on several magnetic properties, including an optimal value of magnetic exchange interaction between grains comprising the medium and a narrow intrinsic magnetic anisotropy field dispersion. While introducing a proper value of intergranular exchange interaction can increase recording resolution by increasing perpendicular M-H loop slope, media noise may also increase, which indicates increased magnetic cluster size associated with non-zero exchange coupling. It is believed that significant intergranular exchange coupling exists in the CoCrPt-oxide layer of the present perpendicular thin film media, especially for media with very small grain sizes. Intrinsic anisotropy field dispersion influences switching field distribution of magnetic clusters and the overall performance of perpendicular media. Larger anisotropy field deviation will adversely impact the transition jitter noise and attainable recording density. Therefore, a reliable method for extracting exchange coupling and anisotropy field dispersion is crucial for developing high quality perpendicular media. Several different methods have been proposed for characterization of anisotropy field dispersion both theoretically and experimentally [5.1]-[5.6]. These include the magnetic remanence measurement method, the M-H loop methods, ΔH (M, ΔM) method, the First Order Reversal Curve (FORC) technique, the transverse susceptibility method and the torque method. This chapter employs numerical micromagnetics to show how intergranular exchange interaction and anisotropy field dispersion can be extracted from measured easy and hard-axis M-H curves. The correlation of both intergranular exchange coupling and anisotropy field distribution with slopes of M-H curves is investigated. The effects of thin film thickness, grain shape and thermal fluctuation are considered in our micromagnetic model. This characterization method allows for an experimental measurement employing a vibrating sample magnetometer (VSM).

5. 2 Simulation model

In order to extract anisotropy field dispersion and intergranular exchange coupling, numerical micromagnetic simulation based on the Laudau-Lifshitz-Gilbert (LLG) equation is utilized to study two types of M-H curves. The easy-axis M-H curve is obtained by measuring the sample magnetization along the easy-axis field direction, where the initial state is fully magnetized. The hard-axis M-H curve is obtained in a similar way but starting from a fully demagnetized state. The two types of M-H curves are distinguished by initial state, magnetization reversal mode and demagnetizing field influence. The slope of the curve is directly obtained from differentiated curves. To study media properties under thermal fluctuation, we used a scaling technique [5.7] that exploits the equivalence of time and temperature to predict the micromagnetic behavior of the granular system over a long time scale.

A thermal micromagnetic model is developed based on the micromagnetic theory and the fluctuation dissipation theorem described in Chapter 2 for a thermally agitated system that consists of magnetostatic interactions between grains. In the model, a realistic grain configuration formed by planar Voronoi cells that represent actual grain shapes was utilized to simulate the perpendicular recording media with a soft underlayer. Each grain is assumed to be a single domain with uniaxial anisotropy. Voronoi cells with average grain diameter of 8.0 nm and standard deviation of 1.8 nm were used. Grain magnetization M_s is 600 emu/cm^3. The grain boundary is set to 1.0 nm so that the packing density is about 80%: this reduces the thin film magnetization. To take account of anisotropy field dispersion, $\langle H_k \rangle$ and σ_{Hk} are introduced as the average anisotropy field and standard deviation of a Gaussian distributed field, respectively. The exchange energy is expressed as $E_{ex} = -J_{ex} \Sigma M_i \bullet M_j (a_{ij}/a_{AVE})$, where a_{ij} is the interfacial area between grain i and j, and a_{AVE} is average side area used to normalize the interfacial area. J_{ex} is the intergranular exchange coupling constant, which is to be quantitatively extracted. It can be shown that due to the Voronoi cell configuration for the media, the intergranular exchange energy or field is dispersed. The summation is taken over all the nearest neighboring grains. The orientation dispersion of the easy axis

in the media is assumed to have a Gaussian distribution with a standard deviation of 5º. The total field consists of anisotropy field, magnetostatic interaction field, exchange coupling field and the external applied field. The medium thickness is 15 nm or 20 nm. The soft underlayer is assumed to have infinite permeability with perfect imaging.

As mentioned in Chapter 2, thermal fluctuations can be taken into account by adding a random field into the total effective field for each grain. The fluctuation field is expressed by a white noise process that has Gaussian distributed components with zero mean value and standard deviation of $\sigma=(2k_BT\alpha/\gamma VM_s\Delta t)^{1/2}$, where α is the material damping constant (approximately equals 0.1 for the recording media), $\gamma=1.759\times10^7$ (Gs^{-1}) is the gyromagnetic ratio, V is grain's volume and Δt is the integration time step when solving the stochastic Landau-Lifshitz-Gilbert equation by the fourth order Runge-Kutta scheme.

A scaling technique is developed to predict magnetic properties of magnetic materials subjected to thermal fluctuations based on the equivalence of time and temperature for thermally activated processes [5.7]. The basic consideration of the technique is that, a system that elapses over a long time at low temperature may be replaced by a system subjected to a larger thermal excitation over short time. The validity of this idea has been demonstrated for time scales longer than 10 nsec [5.9]. The Arrhenius-Neel law [5.10] implies that the energy barrier preventing switching is given by:

$$\Delta E = k_B T \ln(2 f_0 \tau) \tag{5.1}$$

where k_B is Boltzmann constant, T is absolute temperature, τ is measurement time, and f_0 is the attempt frequency. In principle, f_0 can depend on T as shown by Brown for the case of an isolated particle with anisotropy axis aligned with the applied field. However, when the energy barrier is higher in comparison with k_BT, the dependence of f_0 on temperature will become weak and can be neglected. Therefore, we assume f_0 is temperature independent.

The derivation of an expression for time and temperature equivalence is described in detailed in [5.7]. Assuming that micromagnetics allows the energy barriers to be taken as identical regardless of temperature, we have equations:

$$\begin{aligned} k_B T_{s-l} \ln(2A\tau_s) &= k_B T_l \ln(2 f_0 \tau_l) \\ k_B T_{s-r} \ln(2A\tau_s) &= k_B T_r \ln(2 f_0 \tau_r) \end{aligned} \tag{5.2}$$

where τ_l is defined as the long time scale of interest, τ_s is typically the shortest time scale not affected by dynamics, e.g., 10 nsec, and a reference time scale τ_r is longer than τ_s, but still computationally feasible. $T_{s\text{-}l}$ (or $T_{s\text{-}r}$) is defined as the equivalent temperature scaled to short time τ_s with respect to T_l and τ_l (or T_r and τ_r). By eliminating f_0 from the (5.2), a convenient form may be found in terms of the sweep rate R. If we take room temperature for both the long time scale and reference time scale, we then have:

$$T_{s-l} = 300 + (T_{s-r} - 300)\frac{\ln(R_s/R_l)}{\ln(R_s/R_r)} \tag{5.3}$$

The scaled temperature, $T_{s\text{-}r}$, can be obtained by varying $T_{s\text{-}r}$ until the hysteresis loop calculated for ($T_{s\text{-}r}$, R_s) matches the hysteresis loop calculated at (300,R_r). The resulting value of $T_{s\text{-}l}$ is then used to calculate the desired micromagnetic properties at the long time scale R_l. An example of directed calculated and predicted hysteresis loops for a magnetic thin film with anisotropy field dispersion of 5% and intergranular exchange coupling of 0.5 is shown is Fig. 5.1. It can be shown in Fig. 5.1 that the hysteresis loop calculated at the scaled temperature, $T_{s\text{-}r}$= 400 K, matches that calculated at T_r= 300 K. According to eqn. (5.3), we will use $T_{s\text{-}l}$ =1200 K at short time scale to calculate the desired micromagnetic properties of the perpendicular thin film at long time scale τ_l (or R_l).

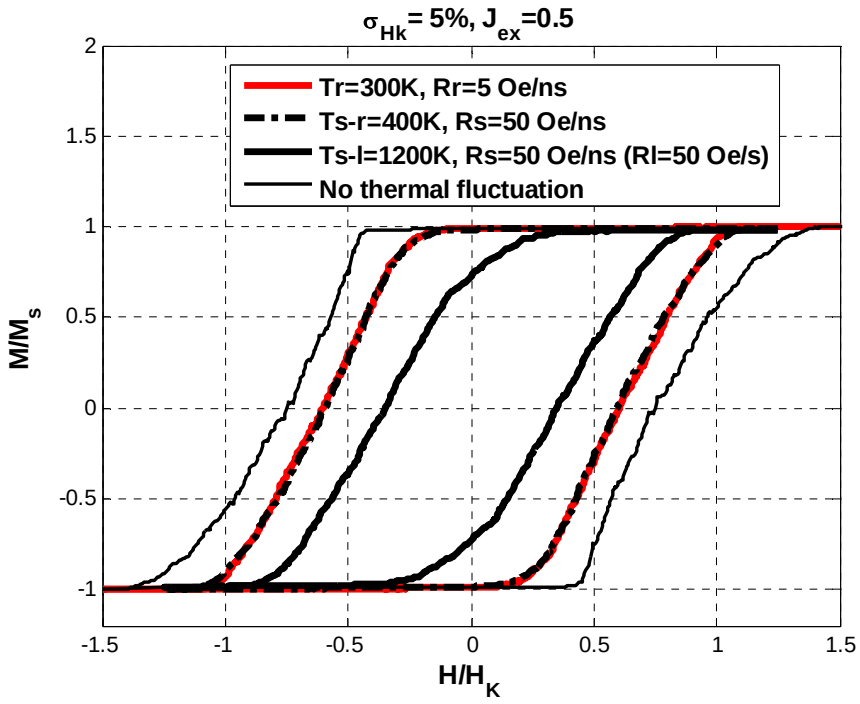

Figure 5. 1 Directly calculated and predicted hysteresis loops of a perpendicular thin film with σ_{Hk}= 5% and J_{ex}=0.5.

5. 3 Differentiated M-H curves of conventional media with variable σHk and Jex

To study how intergranular exchange interaction and anisotropy dispersion can affect two types of M-H curve, we define k_{EA} (or k_{HA}) = d(M/M_S)/d(H/‹H_k›) as the normalized slope of easy-axis (or hard-axis) M-H curve, respectively. Uniform and Gaussian distributed anisotropy fields with a series of standard deviations σ_{Hk} are considered, while the average K_u of the recording layer grain is fixed as 3.6×10^6 erg/cm^3. Meanwhile, a series of J_{ex} from 0.0 to 1.0 are used to calculate the effective exchange field of grain i as $H_{ex}= -2J_{ex}\,\Sigma M_j\,(a_{ij}/a_{AVE})$. The media thickness is initially set to 15 nm. To simulate the thermal activated recording media, assuming the VSM

sweep rate to be 50 Oe/s at T= 300K, we find the scaled temperature at VSM sweep rate (long time scale) to be 1200 K at 50 Oe/ns sweep rate (short time scale).

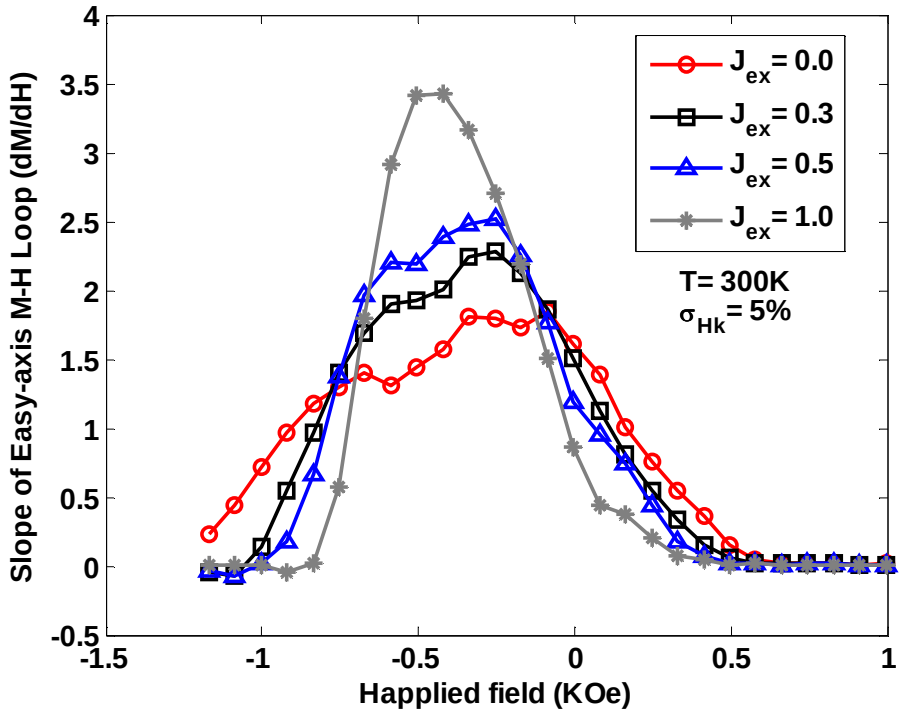

(a)

Fig. 5.2 (a) and (b) show calculated easy-axis M-H curve slope k_{EA} for media with a perfect soft underlayer at T=300 K with various exchange coupling constants and anisotropy field dispersions, respectively. The average anisotropy field ‹H_k› is 12 KOe. In Fig. 5.2 (a), the maximum value of k_{EA} increases as the exchange coupling increases from 0 to 1.0. The variation of exchange coupling from 0.0 to 1.0 yields an increase of coercive squareness. The nucleation field increases with stronger exchange coupling that increases the resistance of magnetization to switching. This corresponds to a change in magnetization reversal mode from individual grain to collective reversal by magnetic clusters. On the other hand, the maximum value of k_{EA} decreases as anisotropy field dispersion σ_{Hk} increases as shown in Fig. 5.2 (b). For a thin film with non-uniform anisotropy field, nucleation of magnetization reversal occurs at grains with a smaller H_k.

With a larger σ_{Hk}, nucleation occurs in a larger range of applied field, yielding a flatter M-H curve.

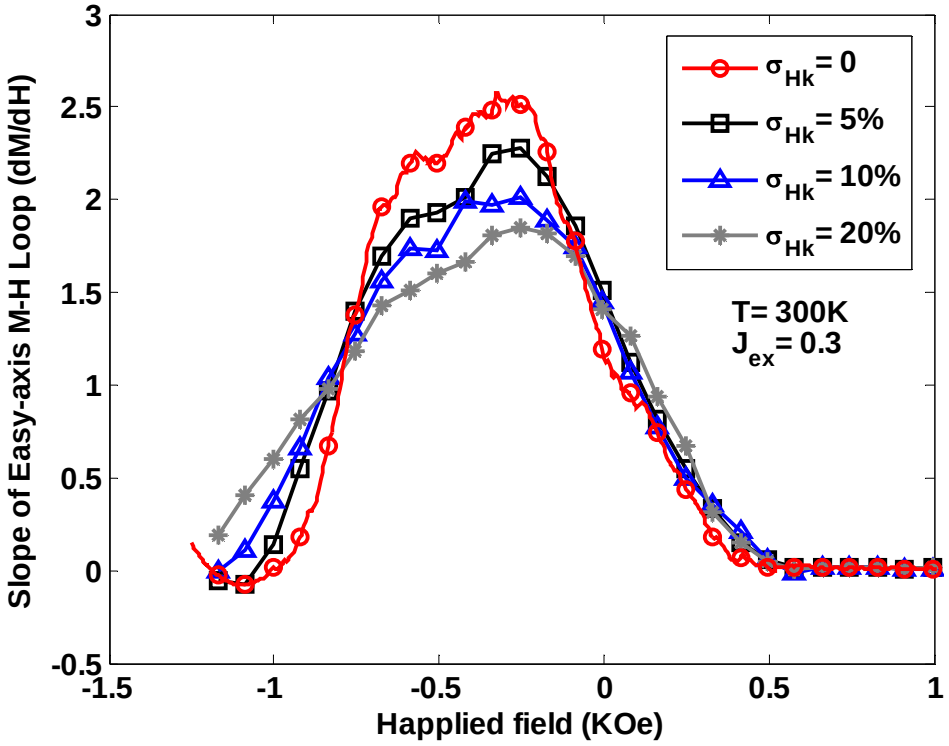

(b)

Figure 5. 2 Easy-axis curve slop at T= 300K with media thickness of 15 nm: (a) σHk =5%, variable Jex; (b) Jex= 0.3, variable σHk.

We can also obtain the hard-axis differentiated M-H curve starting from the fully demagnetized state for a series of J_{ex} with σ_{Hk} set to 10%, as shown in Fig. 5.3, where the hard-axis curve is obtained by applying a longitudinal field to the fully demagnetized media. An example of the resulting demagnetized state for different J_{ex} from 0.0 to 1.0 is given in Fig. 5.4, where the medium is 15 nm thick with 10% anisotropy field dispersion. As J_{ex} increases, the magnetic cluster size or magnetization reversal region increases as shown in the fully demagnetized samples. Larger magnetization reversal regions for increased J_{ex} values can explain the larger initial M-H slope in Fig. 5.3.

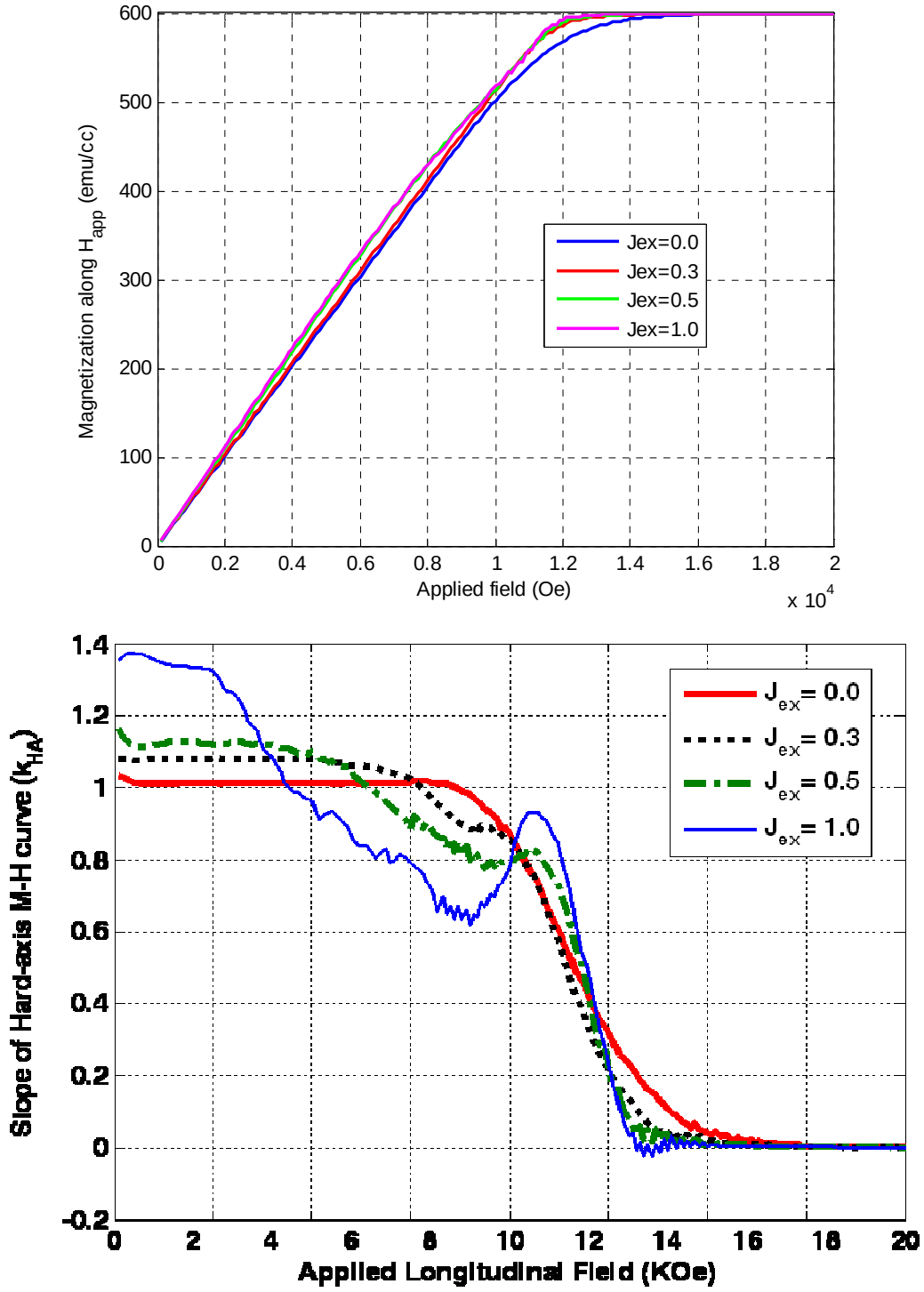

Figure 5. 3 Hard-axis M-H curves and their differentiated curves for 15 nm thick media with J_{ex} from 0.0 to 1.0 and σ_{Hk} set to 10% at T=0 K.

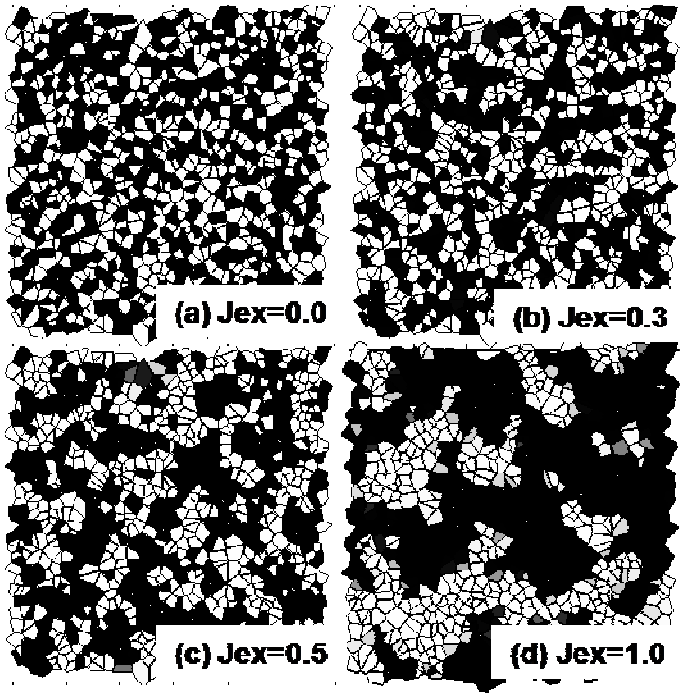

Figure 5. 4 An example of fully demagnetized media for various Jex from 0.0 to 1.0, σ_{Hk} is 10% and T=0K.

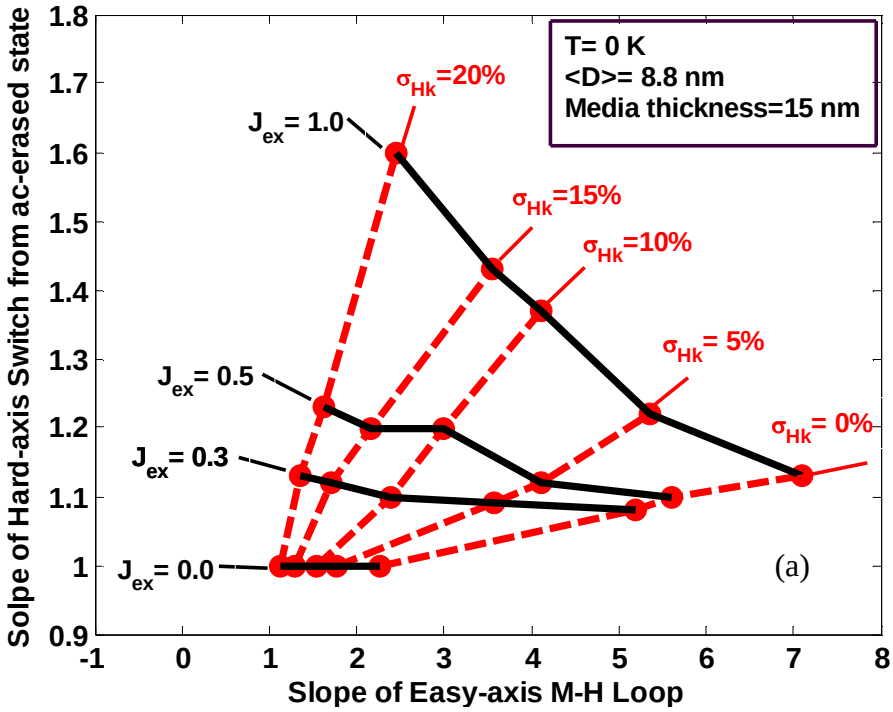

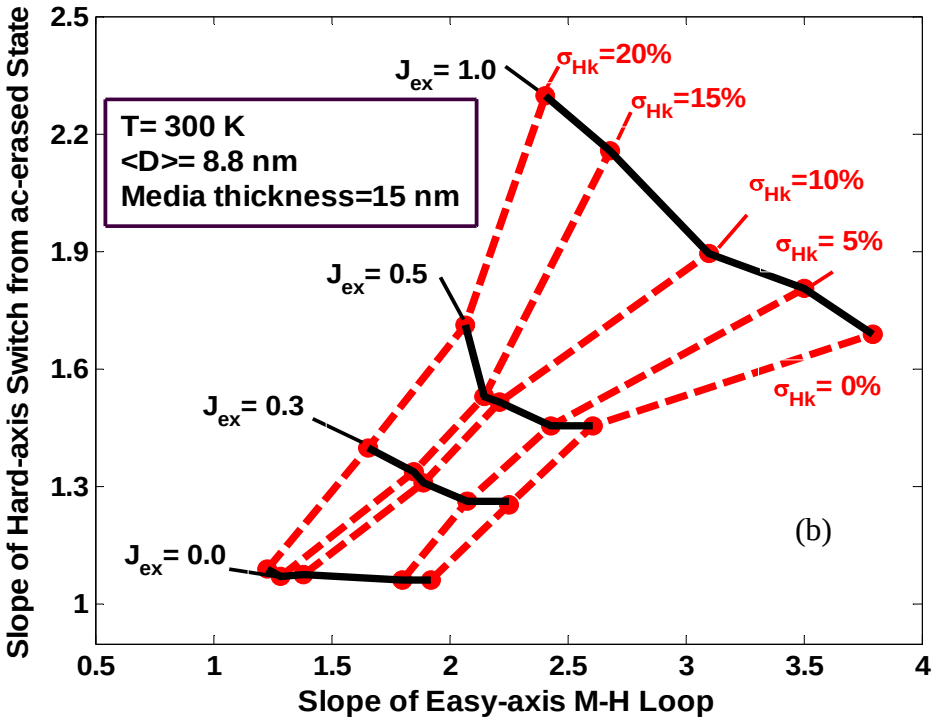

Figure 5. 5 (k_{EA}, k_{HA}) plots for various J_{ex} and σ_{Hk} with media thickness of 15 nm at: (a) T=0 K; (b) T= 300K.

Fig. 5.5 (a) and (b) show the effect of J_{ex} and σ_{Hk} on the easy-axis curve slope k_{EA} and hard-axis curve slope k_{HA} at T= 0K and 300 K, respectively. It is shown in Fig. 5 (a) and (b) that larger J_{ex} increases both k_{EA} and k_{HA} when σ_{Hk} is held constant, since larger J_{ex} tends to form larger cluster size and thus produce steeper M-H curves. On the other hand, the effect of σ_{Hk} is different when J_{ex} is fixed: for hard-axis switch, larger σ_{Hk} produces steeper M-H curves, whereas for easy-axis switch, larger σ_{Hk} produces flatter curves. In fully demagnetized media with a large J_{ex} and therefore larger cluster size, exchange field will assist rotating the grains within clusters, yielding a steeper slope. With larger σ_{Hk} and thus more anisotropy inhomogeneities, however, the film breaks up into smaller clusters, producing a flatter M-H curve along easy-axis. Fig. 5.5 (a) also shows that effect of σ_{Hk} on hard-axis slope becomes more significant as J_{ex} increases. Without intergranular exchange, k_{HA} remains at the same value even for a large σ_{Hk}

since all grains tend to rotate individually and k_{HA} is equal to 1.0. With non-zero J_{ex}, some grains having smaller H_k will rotate first, assisting the neighboring grains to rotate collectively via intergranular exchange coupling. As σ_{Hk} is increased, more grains are involved in this collective rotation, producing a larger k_{HA} over a range of applied field. Similar results can be obtained at T=300 K, as shown in Fig. 5.5 (b), except with a different scale and deviation since an uncorrelated random thermal field is considered.

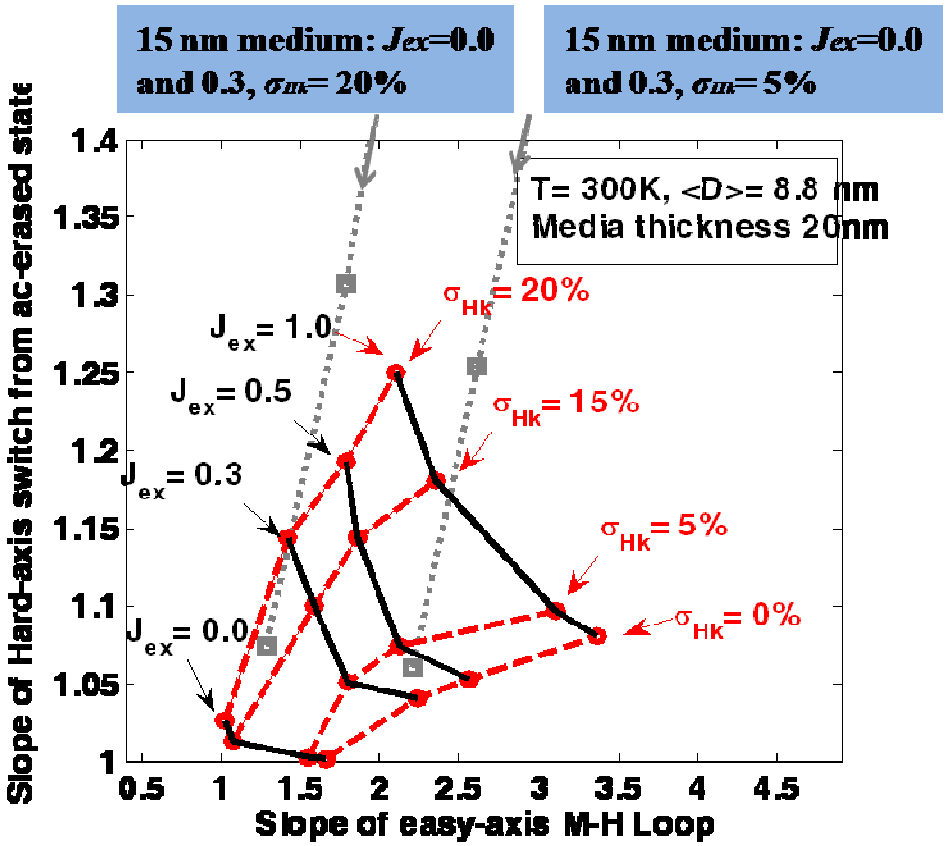

Figure 5. 6 (k_{EA}, k_{HA}) plots for various J_{ex} and σ_{Hk} with media thickness of 20 nm at T = 300 K; the grey lines are results from Fig. 4 (b) for J_{ex}=0.0 and 0.3, σ_{Hk} =5% and 20%.

In order to illustrate the effect of demagnetization and media thickness on extracting J_{ex} and σ_{Hk}, we increase the medium thickness to 20 nm and compared the new (k_{EA}, k_{HA}) plot in Fig. 5.6 with the previous one in Fig. 5.5 (b) for 15 nm thick medium at T=300K. The easy-axis M-H curve has a shallower slope, and thus smaller k_{EA}, because the grains are elongated within the film and thus interact more strongly which can be viewed as an enhanced demagnetizing field along the perpendicular

direction. In addition, k_{HA} is reduced for both zero and non-zero exchange coupling regardless of anisotropy field dispersion. In weak intergranular exchange coupling recording media, the magnetostatic energy tends to increase with the increase of J_{ex} but this effect is less important for thicker media. The reduction of k_{HA} results from reduced demagnetizing field of ac-erased magnetic clusters for increasing medium thickness.

5. 4 Magnetization auto-correlation function analysis

In conventional media, a non-magnetic grain boundary thickness distribution can yield a distribution in intergranular exchange coupling, which could affect the switching field distribution. To investigate the effect of dispersed intergranular exchange coupling, J_{ex} is assumed to follow a uniform distribution ranging from 0 to 2•‹J_{ex}›, with a mean value of ‹J_{ex}› and standard deviation of ‹J_{ex}›/√3. Then, the magnetic cluster size of various ac-erased magnetization distributions are quantitatively analyzed for different J_{ex} average values. We calculated the auto-correlation function directly from the ac-erased magnetization distribution and found a correlation between the shape of the auto-correlation function and the exchange deviation. Fig. 5.7 shows the normalized auto-correlation function of ac-erased magnetization distributions obtained at T =300K and σ_{Hk} =10%, for a series of J_{ex} values. For both types of J_{ex} distributions, as the value of J_{ex} increases, the zero-cross point of the auto-correlation function increases, as expected because the zero-cross point is proportional to the correlation length and thus the average magnetic cluster size ‹D›. In addition, the undershoot value of the auto-correlation function decreases as the cluster size deviation σ_D /‹D› increases. From Figs. 5.8(a) and (b), we find that the domains in the highly dispersed sample tend to be less connected and slightly narrower, although equally long, than the domains in the mono-dispersed samples. This may account for the small decrease in correlation length. Although these trends are interesting, the measurement of auto-correlation functions is more difficult than M-H loops and the differentiations less substantial.

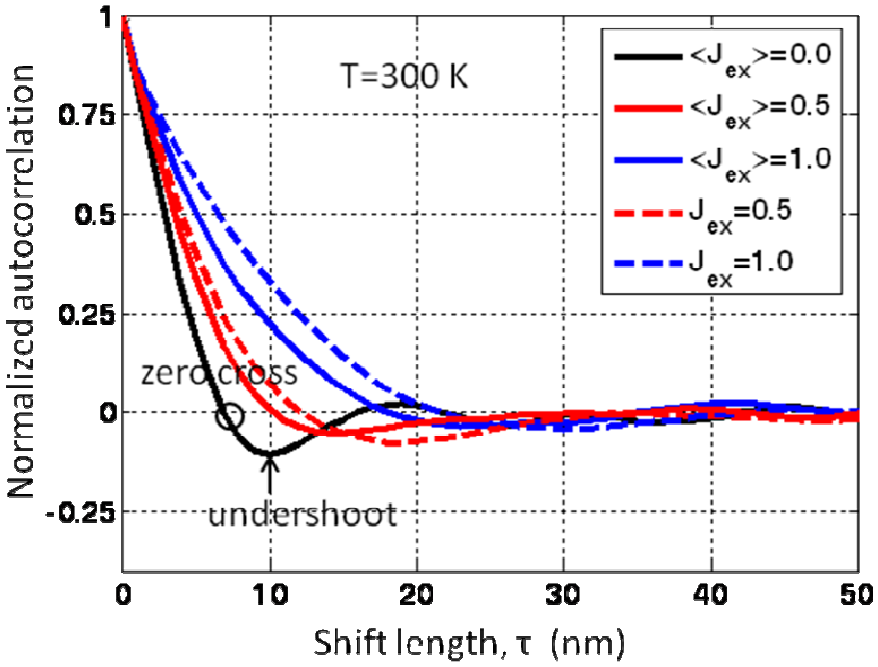

Figure 5. 7 Comparison of auto-correlation functions of ac-erased magnetization distribution for both uniform and dispersed J_{ex}. Solid lines are the results of dispersed J_{ex} with an average value from 0.0 to 1.0. Dash lines are the results of uniform J_{ex} values. The zero-cross point and the undershoot value are labeled in the figure.

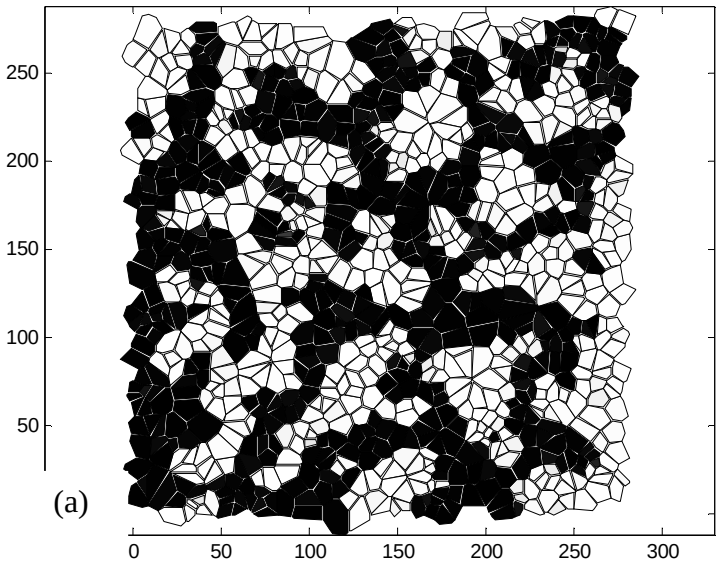

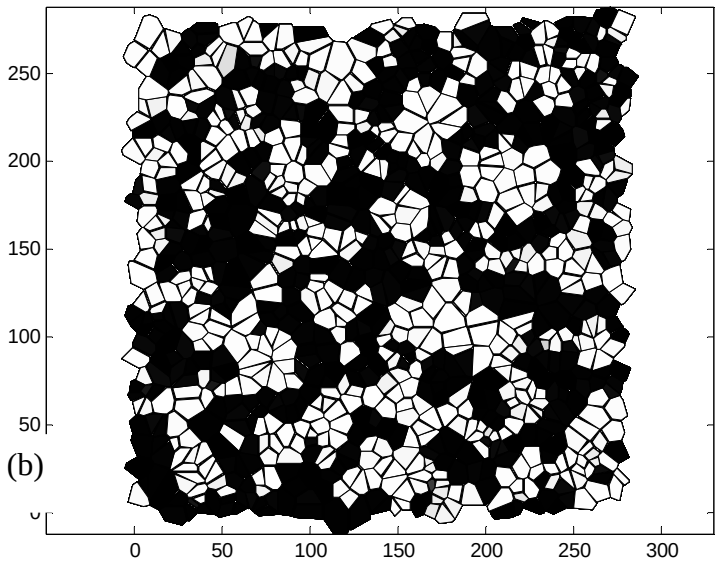

Figure 5. 8 An example of fully demagnetized media for (a) Jex is a constant value of 1.0 and (b) Jex has uniform distribution from 0.0 to 2.0 with an average value of 1.0. σHk is 10% and T=0 K.

5. 5 Conclusion

A micromagnetic numerical technique has been used to demonstrate how intergranular exchange coupling and intrinsic anisotropy field dispersion can be extracted from measuring two types of M-H curves. A realistic grain configuration formed by planar Voronoi cells is used to simulate perpendicular magnetic media. This technique effectively separates the effects of intergranular exchange coupling and anisotropy dispersion by finding their correlation to differentiated M-H curves with different initial magnetization states, even in the presence of thermal fluctuation. A scaling technique is employed to simulate M-H curves for a VSM sweep rate at room temperature. The effects of grain shape, intrinsic anisotropy field dispersion σ_{Hk}, and media thickness are all considered in extracting intergranular exchange coupling. The validity of this method is investigated with a series of intergranular exchange couplings and anisotropy dispersions for different media thickness. A relationship between the

auto-correlation function of an ac-erased sample and dispersion of the exchange interaction is demonstrated. Utilizing magnetization auto-correlation functions, the magnetic intergranular exchange coupling statistics show a correlation with the auto-correlation function shape in terms of zero-cross and undershoot values.

This characterization method is simple and effective for VSM measurement. By differentiating easy-axis and hard-axis M-H curves to obtain the maximum values of slope k_{EA} and k_{HA}, we find that the effects of exchange J_{ex} and σ_{Hk} on k_{EA} and k_{HA} are different: Increasing J_{ex} increases both k_{EA} and k_{HA}. Larger σ_{Hk} produces larger k_{HA} but smaller k_{EA}. In addition, the effects of J_{ex} and σ_{Hk} on k_{EA} and k_{HA} are correlated: effect of σ_{Hk} on hard-axis slope becomes more significant as J_{ex} increases. The effect of dispersed J_{ex} can be studied from the magnetization auto-correlation functions by utilizing correlation length and the undershoot value.

Chapter 6 Micromagnetic Specification for Bit-patterned Recording at 4 Tbits/in^2

It has been argued that the difficulty of extending the magnetic recording areal density up to 1 Tbit/in^2 is due to the limitations of perpendicular recording media itself. In conventional media, the magnetic thin film is composed of small and single-domain grains which neither have an ordered pattern, nor identical sizes. The irregularity and the strong interaction of the grains cause transition noise and thus deteriorates the signal-to-noise ratio at ultra high areal densities. Moreover, grain size cannot be shrunk significantly without the magnetization becoming unstable or superparamagnetic. Bit patterned media, in which each bit is stored in a single-domain magnetic island, have been suggested to extend areal density beyond 1 Tbit/in^2 [6.1]. Arrays of magnetic dots with 4 Tbit/in^2 areal density imply dot size as small as 4.2 nm× 9.5 nm for a bit aspect ratio (BAR) of 2.3. Fig. 6.1 shows the media configuration and the key parameters that correspond to 4 Tbit/in^2 recording. The lithographically separated islands can reduce or eliminate transition noise and non-linear bit shift, simplify track edges, and provide a solution for thermal instability because the stability criterion refers to the anisotropy and the whole volume of a single island, not to the individual grain mentioned above.

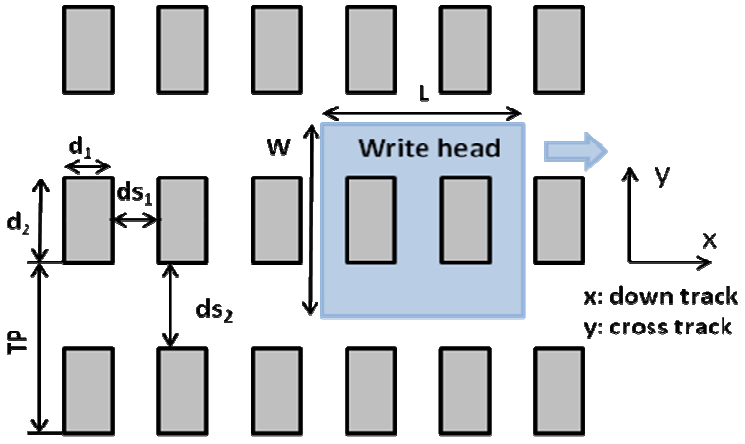

Figure 6. 1 Key dimensions of 4 Tbits/in2 bit patterned media with a bit aspect ratio (BAR) of 2.3. The track pitch is 19.0 nm and the bit-to-bit spacing is 8.4 nm.

The problems associated with the bit patterned media recording arise from the fluctuations of the dots. Specifically, variations in island size and island spacing, statistical fluctuations in switching field and variance in writing synchronization and magnetic fly height can deteriorate the recording performance and lead to writing errors. The write head field strength and field gradient becomes very important for achieving satisfactory bit error rate performance. In this paper, we propose micromagnetically optimized specifications for the write head and exchange coupled composite (ECC) based patterned media with a bit aspect ratio (BAR) of 2.3 or higher, assuming several key and realistic constraints suitable for 4 Tbit/in^2 recording. To achieve this, we firstly design a write head capable of producing sufficiently large perpendicular field and field gradient to ensure thermal stability and alleviate adjacent track erasure. Secondly, we study the shielding effect of side shields on the neighboring side tracks and derive the demagnetizing field distribution. Finally, utilizing the optimized write head, comprehensive analysis including the combined field distribution is presented to evaluate the bit error rate based on the statistical properties of the ECC bit pattern media and a set of head-to-media combinations.

6. 1 Optimum multi-pole tapered write head design

Our 3-D write head model consists of a main pole, side shields, a return pole and soft underlayer (SUL) assumed to offer perfect imaging. A saturation input flux is applied uniformly at the top surface of the main pole. The flux is completed by applying an equal but negative flux on the top surface of the return pole. Fig. 6.2 (a) and (b) show the geometries of the down track (DT) and cross track (CT) views of the write head model. The pole length and pole width are both 20 nm at the air bearing surface (ABS). ΔW is the writing window where the head is able to switch a dot that is currently being written. We use a fly height of 4 nm or 5 nm and a 2 nm non-magnetic interlayer between the SUL and the recording media. The write pole, side shields and the return pole are discretized into 10 nm × 10 nm × 10 nm cubic cells. Each cell is assumed uniformly magnetized with exchange stiffness of 1.0×10^{-6} erg/cm. The simulation uses

the Landau-Lifshitz-Gilbert (LLG) equation to model the magnetization reversal and to obtain the equilibrium state. The integration time step for solving the LLG equation is set to 10^{-13} s. The exchange coupled composite based bit patterned media consist of magnetic soft (top) and hard (bottom) regions with a volume averaged media magnetization of 900 emu/cm^3. The thicknesses of two regions are the same and the total thickness is 10 nm. The perpendicular component of the head fields are evaluated at the center of the soft region in the media.

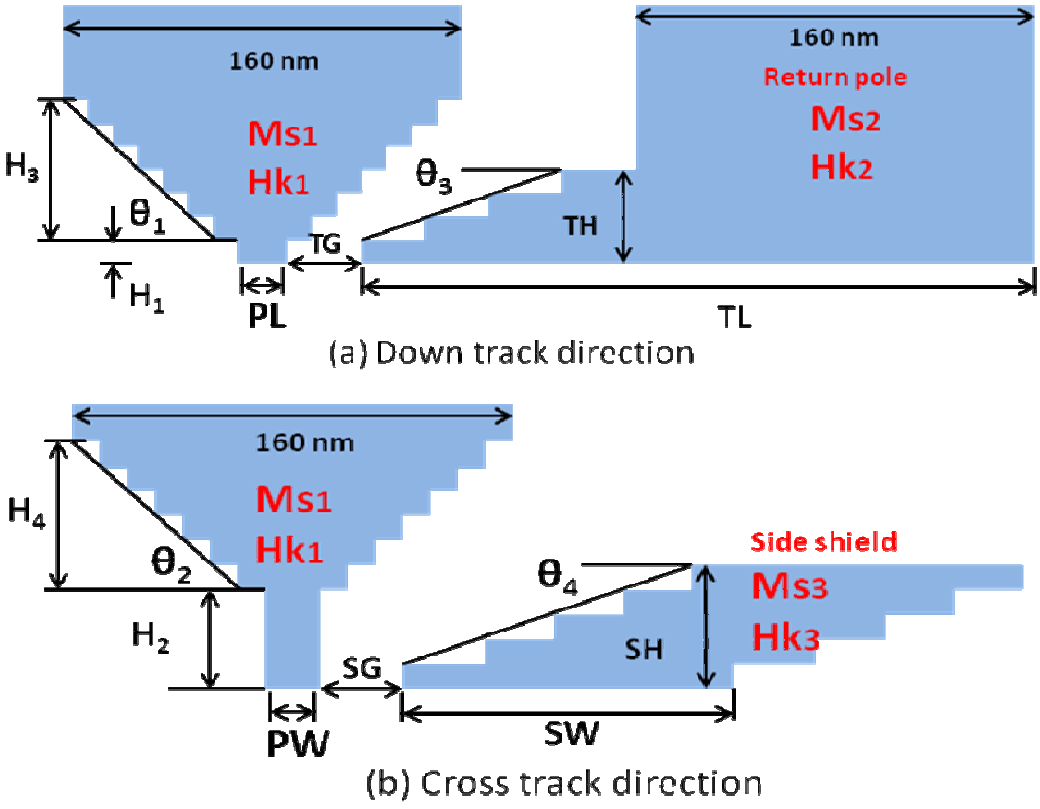

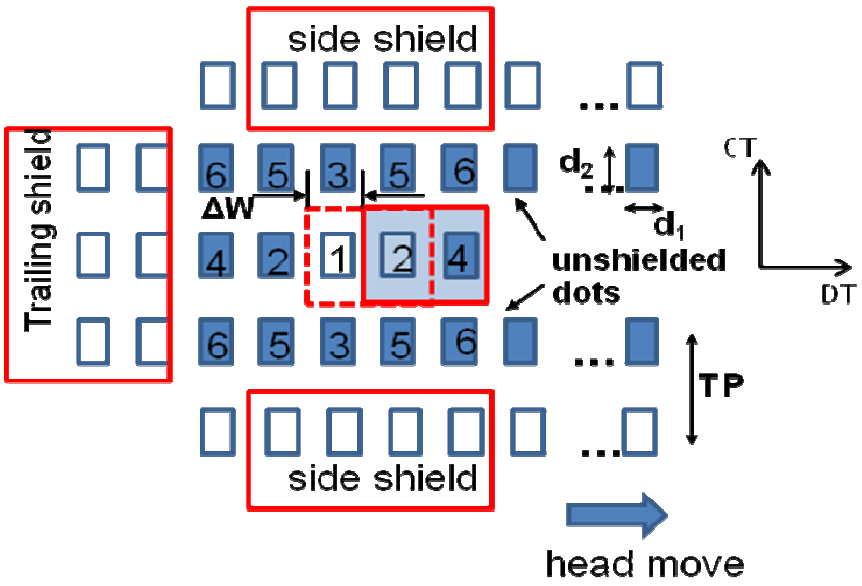

Figure 6. 2 3-D write head structure at (a) down track view, (b) cross track view and (c) bit patterned media configuration with several key parameters.

To study the effect of main pole shape on the field strength, the tapered-neck angle θ_1 and θ_2 and the throat heights H_1 and H_2 are varied and optimized in terms of field strength and field gradient. Simultaneously, the side shield gap SG and its tapered angle θ_3 are optimized to increase the cross track gradient thereby decreasing the cross track pitch. It is worth noting that the trailing shield gap TG and its tapered angle θ_4 can affect the field strength where the down track field gradient peaks. In the optimized design that meets the requirement of 4 Tbit/in^2 recording, $\theta_1=\theta_2=45°$, $\theta_3=\theta_4=23°$. H_1=10 nm, H_2=40 nm, H_3=50 nm, H_4=70 nm, SG=18 nm, TG=20 nm, TL=300 nm, SW=120 nm, SH=50nm and TH=40 nm. Fig. 2 shows the down track and cross track perpendicular field evaluated at the center of the top soft region of the media. Owing to the unique angular dependence of the ECC media [6.2], the optimization focuses on the perpendicular field component. As shown in Fig.6.3, the maximum field strength is 12.5 kOe, and the down track field tends to have larger gradient than that along the cross track since larger values of BAR require much steeper field along the down track to reduce writing errors. Fig. 6.4 shows the perpendicular field gradient profile for 4 nm fly height. The down track perpendicular field gradient peaks at 539 Oe/nm with 9.2

kOe field amplitude while the maximum cross track perpendicular field gradient is 525 Oe/nm at 9.9 kOe. Since achieving the highest areal density depends crucially on the maximum field gradient, the average switching field H_{sw0} is therefore chosen as 9.2 kOe.

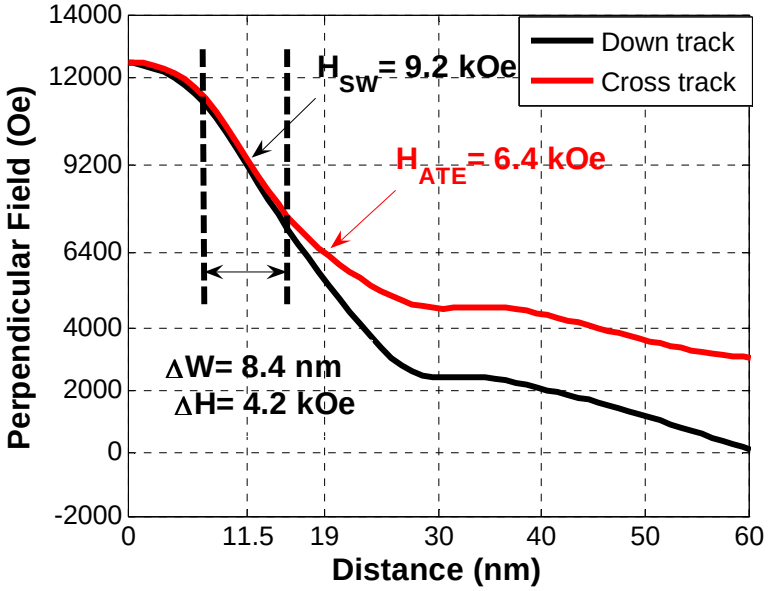

Figure 6. 3 Perpendicular field profiles along the down track and cross track directions.

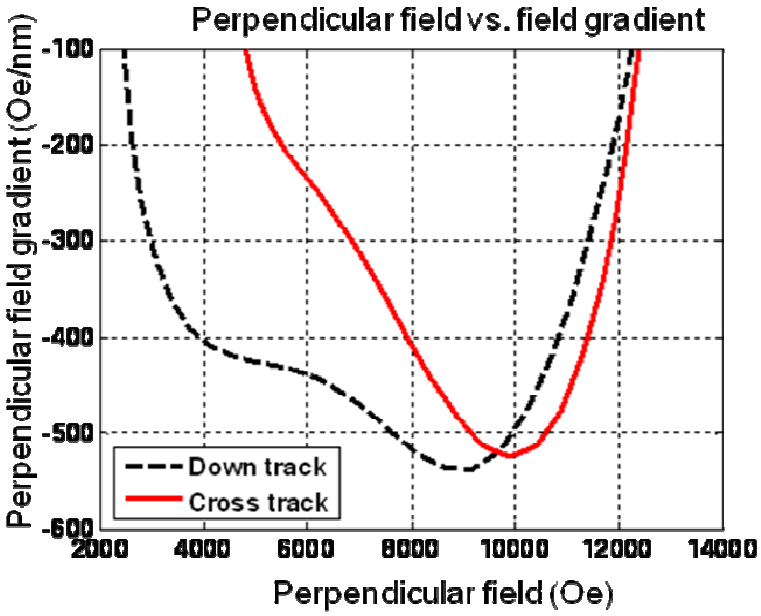

Figure 6. 4 Perpendicular field gradient profiles along the down track and cross track directions.

With the knowledge of average switching field, the average anisotropy energy of a single ECC based magnetic dot can be calculated as [6.2]: $K_{ave}=0.5\times M_s\times H_{sw0}\times 1.12\times \xi$. The factor ξ accounts for the benefit of ECC media in switching field compared to the conventional media at the same level of thermal stability and is calculated as $\xi \equiv 2\Delta E/(H_{sw}\times M_s\times V)$. We calculated that 1.12 accounts for the effect of thermally assisted switching a $9.5\times 4.2\times 10$ nm^3 magnetic dot at room temperature [6.3]. M_s is the average magnetization of the magnetic dot, set to 900 emu/cm^3. H_{sw0} is selected from Fig. 6.3 as 9.2 kOe. The thermal stability ($K_{ave}V/k_BT$) for the magnetic dot is 123 at 4 Tbit/in^2 areal density.

Once the coercivity field is determined, the adjacent track erasure field H_{ATE} can be evaluated using

$$H_{ATE} = H_{sw0}\times\left[1-\left(\ln(\eta f_0\tau)\bullet\frac{K_{ave}V}{k_BT}\right)^{2/3}\right] \qquad (6.1)$$

where η^{-1} is the acceptable magnetization decay ratio per bit, set to 10^{-3}. τ is the time determined by 10^3 writer passes with a writer speed of 30 m/s, calculated as 6.67×10^{-7} s, f_0 is the thermal fluctuation frequency set to 10^{12} Hz [6.3]. We also need to make sure that H_{ATE} is greater than the maximum side field induced by the side shields. The fringe field that will cause adjacent track erasure (ATE) is $0.70\times H_{sw}$. The fringe field therefore can be found from Fig. 6.3 as 6.4 kOe, with a distance of 19.0 nm from the track center, i.e., the minimum track pitch (TP). Therefore, 4 Tbit/in^2 recording will have a bit size of 9.5 nm× 4.2 nm (BAR of 2.3).

6. 2 Shielding effects on the neighboring tracks

As discussed in Section 6.1, using a trailing shield and side shields can generate a steeper field without substantially degrading the field strength. The optimized side gap is 18 nm and the trailing shield gap is 20 nm. Compared to the 9.5 nm× 4.2 nm bit configuration, however, the nearest side tracks and a few islands previously written on

the current track are not shielded at all, as can be observed in Fig. 6.2(c). The stray field from these bits, which should be considered random, will disturb the head field applied to the currently written bit and therefore should be countered to reduce the nonlinear bit shift effect. The effectiveness of the side shields is analyzed in terms of the stray field from the side tracks as well as their effect on the magnetization pattern in the shields and the tip.

Table 6.1 shows the stray field from the neighboring bits to the currently written bit. Note that the fields are only applied to the perpendicular component and show strong distance dependence. Assume that the unshielded bits on the current track, i.e., bit #2 and #4 as shown in Fig.1(c), are both dc-erased. The stray field to the currently written bit #1 is $H_z = 0.055\times M_{s4} + 0.24\times M_{s2} = 265$Oe. Although the trailing shield is found to be ineffective in reducing the stray field and therefore cause non-linear transition shift, it is deterministic and therefore can be compensated.

Pair-wise interaction	Stray field H_z
1-1	$-2.53\times M_s$
1-2	$-0.24\times M_s$
1-3	$-0.065\times M_s$
1-4	$-0.055\times M_s$
1-5	$-0.045\times M_s$
1-6	$-0.028\times M_s$

Table 6. 1 Perpendicular component of demagnetizing field from the neighboring dots on the currently written dots.

On the other hand, assuming that the side tracks are dc-erased to simulate the worst case scenario, the maximum stray field difference between dc-erasing the nearest side tracks in the up and down direction is about $2\times 0.3\times M_s = 540$ Oe. Similarly, the stray field difference from the second nearest side track between dc-erased up and down

direction is $2\times0.09\times M_s$= 162 Oe. These stray fields should be considered random and contribute to the demagnetizing field distribution acting on the currently written dot.

To study the shielding effect of the side shields on the neighboring tracks, we consider the worst case scenario: the side tracks are all dc-magnetized to produce the maximum interaction field causing an increase or decrease of the perpendicular field component of the head field. Micromagnetic simulation is modified to include an array of magnetostatically interacting bit patterned media and the optimized 3D write head. Note that for the currently written dot: $H_{total}=H_{head}+H_{stray}$, where H_{head} is the field from the write head evaluated at the center of the top layer. When the side track magnetization is in the same direction as the magnetization in the tip, the stray field from the side track tries to misalign the magnetization along the perpendicular direction, and weakens the head field to H_{head1}. When the side track magnetization is in the opposite direction to the magnetization in the tip, the head field will increase to H_{head2}.The change in the perpendicular head field due to the change of side track magnetization is $H_{head1} - H_{head2} \approx -160$ Oe. The shielding of the second nearest side tracks by the side shields is efficient, since only (162-160=) 2 Oe stray field is not cancelled out and ultimately disturbs recording in the current track. Therefore, the stray field from the nearest side tracks is the dominant part that produces the demagnetizing field distribution.

6. 3 Variance and error rate analysis

As already discussed in the literature [6.4] and [6.5], imperfections of the bit patterned media can deteriorate the system performance and result in a bit error rate that is analogous to the signal-to-noise ratio in conventional recording system. In our paper, we confine ourselves to four different sources of noise that are assumed random and uncorrelated: timing error $\sigma_{x,time}$ due to the writing synchronization variance, jitter error $\sigma_{x,jitter}$ due to the dot spacing and dot size variance, intrinsic switching field distribution σ_{Hsw} and demagnetizing field distribution σ_{Hd}. All these disturbances are applied to the currently written dot and can be considered as Gaussian distributed, with a variance of

σ^2. Note that the demagnetizing field from the previously written dots in the current track should not be considered as random and are excluded from calculating $\sigma_{Hd.}$

The maximum magnetostatic interaction field occurs if all contributing dots are magnetized in the same direction causing an increase or a decrease of the perpendicular component of the head field. The maximum demagnetizing field produced by the nearest side tracks and the on-track dots further away is about 620 Oe and the standard deviation σ_{Hd} is about 180 Oe. An example for a histogram for the distribution of the demagnetizing fields is given in Fig. 6.5. It is found that it is justified to approximate the demagnetizing field distribution as a Gaussian.

In addition, the variance of the writing position due to the timing and jitter error can also lead to a field variance acting on the writing dot from the chain law:

$$\sigma_{H,t} = avg\left(\frac{d\mathbf{H}_{head}}{dx}\right)\bullet\boldsymbol{\sigma}_{x,time}$$
$$\sigma_{H,j} = avg\left(\frac{d\mathbf{H}_{head}}{dx}\right)\bullet\boldsymbol{\sigma}_{x,jitter} \qquad (6.2)$$

where $avg\left(\frac{d\mathbf{H}_{head}}{dx}\right)$ is the average down track field gradient evaluated within the writing window.

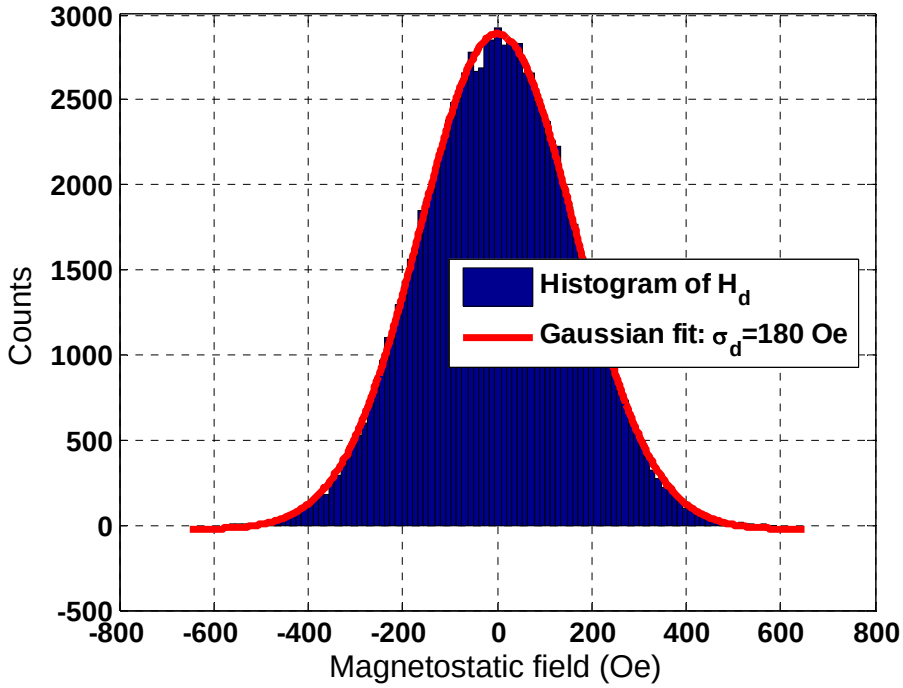

Figure 6. 5 Example for the distribution of demagnetizing fields acting on the currently written rectangular dot for 4 Tbits/in^2 recording density.

Summing up the variances due to timing error, jitter error, and anisotropy field and demagnetizing field distribution, the combined field variance can be expressed as:

$$\sigma_H^2 = \sigma_{H,t}^2 + \sigma_{H,j}^2 + \sigma_{Hsw}^2 + \sigma_{Hd}^2 \tag{6.3}$$

Since the switching field is distributed, there is a finite probability that the maximum available field is not sufficiently large to switch all dots. Assuming a Gaussian distribution for the statistical fluctuations, the probability that the dots are not switched at all is given by

$$P_{w1} = 0.5 \times \left(1 - \mathrm{erf}\left(\frac{H_{max} - H_{sw0}}{\sqrt{2}\sigma_H} \right) \right) \tag{6.4}$$

where H_{max} is the maximum head field within the writing window ΔW and H_{sw0} is the average switching field located at the center of the writing window. The factor 0.5 represents a one-sided integration of the Gaussian function since the low end of the switching field distribution can always be switched by the head field.

As the head moves down-track across the writing window for the currently written dot and instantly switches polarity, there is a region where the head field can potentially reverse the previously written dot and result in error. Similarly, the probability of reversing the previously written dot is given by

$$P_{w2} = 0.5 \times \left(1 - \mathrm{erf}\left(\frac{H_{sw0} - H_{min}}{\sqrt{2}\sigma_H} \right) \right) \tag{6.5}$$

where H_{min} is the minimum head field within the writing window ΔW. The factor 0.5 represents a one-sided integration of the Gaussian function since the higher end of the switching field distribution cannot be switched by the head field. Summing up both error events, the writing bit error rate is given by

$$P_w = P_{w1} + P_{w2} \tag{6.6}$$

6. 4 Bit error rate and areal density estimation

In this section, the areal density, the values of bit aspect ratio and the corresponding bit error rate P_W are estimated based on our optimized 3D write head design of Section 6.2. The media thickness is 10 nm. Note that ξ of the media is set to 2.7 or 2.4 and the magnetic fly height is varied from 4 nm to 5 nm. The non-magnetic seed layer thickness is set to 2 nm. The writing window is selected as 8.4 nm where the down track field gradient is sufficiently large to generate the head field ranging from 7.1 kOe to 11.3 kOe. The average field gradient is calculated around 500 Oe/nm. The timing error $\sigma_{H,t}$ /ΔW is set to 5% and the jitter error $\sigma_{H,j}$ /ΔW is 5%. With these constraints, the corresponding field variance can be calculated from (3) as 210 Oe and the combined field variance is σ_H= 576 Oe. The combined bit error rate from (4)-(6) can be as small as 2.7×10^{-4} for 4 Tbit/in^2 recording with a BAR of 2.3.

Table 6.2 shows the dependence of bit error rate on the intrinsic switching field distribution and the resulting combined field variance. It shows that to achieve a BER no larger than 1.0×10^{-3} with a BAR of 2.3 and 4 nm fly height, the intrinsic switching

field distribution can be as large as 6% and combined field distribution σ_H/H_{sw0} can be 7%.

σ_H (Oe)	506	540	576	614	652
σ_{Hsw} (Oe)	4%	4.5%	5%	5.5%	6%
BER	3.3×10^{-5}	1.0×10^{-4}	2.7×10^{-4}	6.3×10^{-4}	1.0×10^{-3}

Table 6. 2 Dependence of BER on the switching field distribution with 4 nm fly height and 2.3 BAR.

Table 6.3 shows the dependence of areal density on fly height, media thickness and thermal stability ratio ξ. Among these specifications, the optimized areal density is 4.5 Tbit/in^2 with 4 nm fly height, bit error rate of 7.2×10^{-4} and bit aspect ratio of 2.5. As the fly height increases to 5 nm, the optimized areal density is reduced to 4.0 Tbit/in^2 with a slightly degraded BER performance of 8.2×10^{-4} and a larger BAR of 2.7. For 4 Tbit/in^2 recording, the increase of fly height from 4 nm to 5 nm will degrade the BER by 200% with 17% BAR increment, although 10% reduction in BAR and thus 3% in areal density can improve the BER for 5 nm fly height. Use of thicker media (12 nm) is found to degrade performance because it increases the magnetic spacing, thus decreasing the field amplitude and gradient. It is worth noting that when the media thermal stability ratio decreases from 2.7 to 2.4 due to the limited thickness, the BERs are further degraded while BARs are increased to achieve the same areal density. This results from a decrease in adjacent track erasure field amplitude thereby increasing the guard band and the minimum track pitch.

FL (nm)	T (nm)	H_{sw} (kOe)	ξ	σ_H (Oe)	ΔW (nm)	BER	BAR	AD (Tbits/in^2)
4	10	9.2	2.7	562	7.6	7.2×10^{-4}	2.5	4.5
4	10	9.2	2.7	576	8.4	2.7×10^{-4}	2.3	4.0
5	10	8.5	2.7	523	7.8	8.2×10^{-4}	2.7	4.0
5	10	8.5	2.7	527	8.0	6.4×10^{-4}	2.5	3.9
5	12	8.0	2.7	497	8.2	9.0×10^{-4}	2.4	3.9
5	12	8.0	2.7	494	8.0	1.1×10^{-3}	2.5	4.0
4	10	9.2	2.4	574	8.3	4.8×10^{-4}	2.4	4.0
5	10	8.5	2.4	517	7.5	1.4×10^{-3}	2.8	4.0

Table 6. 3 Dependence of areal density (AD) and BER on fly height, media thickness and thermal stability ratio.

6. 5 Hexagonal Array Bit-patterned Recording at 2.9 Tbits/in^2

One challenge of achieving 2.5 BAR rectangular arrays of bit patterned media is the fabrication process that requires essentially defect-free patterns [6.6], and precise control over pattern feature and placement. Compared to rectangular arrays, hexagonal arrays can be formed spontaneously by directed block copolymer self-assembly [6.7] and other self assembly techniques that are considered to be a promising cost-effective approach to achieving higher density and dimensional uniformity.

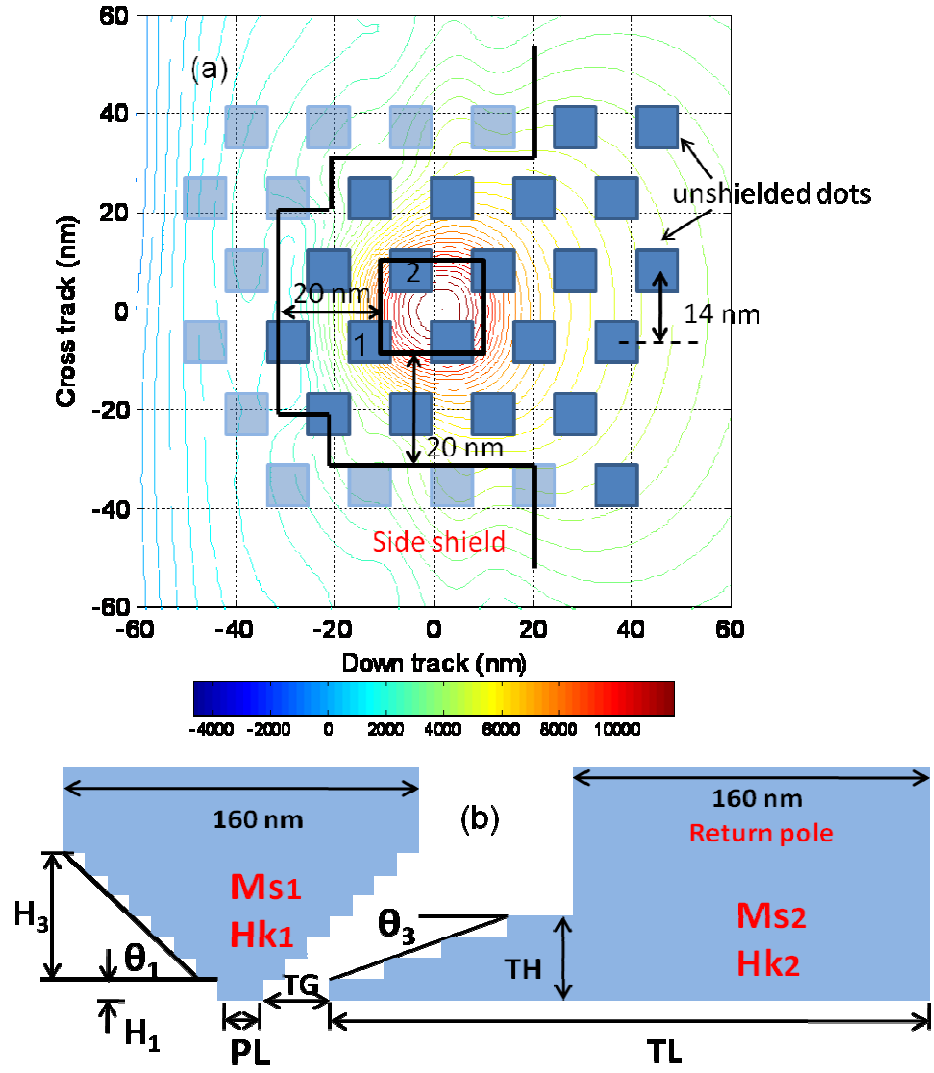

Figure 6. 6 (a) The head writes two staggered tracks in a single pass in hexagonal array BPM with 8.1nm dot size. Bit #2 is the currently written dot and bit #1 is the previously written dot. (b) The side profile of the head in the downtrack direction.

Fig. 6.6 shows the staggered track BPM with a track pitch of 28nm. It can be shown by comparing with non staggered track BPMR, that the writing window is significantly reduced due to the presence of neighboring dots. The condition for correct writing requires switching of the central region of individual bits without overwriting the adjacent tracks and the previously written bits. This leads to constraints on the head

field, i.e., the field should be large enough to switch the central region of the currently written bit, but it also should be weak enough to avoid switching any previously written dots.

For the purpose of recording the staggered track BPM, it is preferable to design a write head capable of generating a high field gradient within the writing window, as well as avoiding ATE due to the fringing field. Fig.6.6 (b) shows our head design consisting of a main pole and a wrap-around shield with pole-trailing shield gap (TG) of 20 nm and pole-side shield gap of 20nm. The pole size (PL) at the air bearing surface is 20 nm by 20nm, the tapered-neck angle along the down track (θ_3) and cross track directions are both 45˚. The throat heights of the pole are set to 10 nm along the down track direction (H_1) and 40 nm along the cross track. The nominal magnetic fly height is set to 4 nm and the interlayer between the recording media and the soft underlayer is 2 nm.

The write pole, side shields and the return pole are discretized into 10 nm × 10 nm × 10 nm cubic cells. Each cell is assumed uniformly magnetized with exchange stiffness of 1.0×10^{-6} erg/cm. The simulation uses the Landau-Lifshitz-Gilbert (LLG) equation to model the magnetization reversal and to obtain the equilibrium state. The integration time step for solving the LLG equation is set to 10^{-13} s. The exchange coupled composite (ECC) bit patterned media consists of magnetic soft (top) and hard (bottom) regions with a total thickness of 10 nm. The head field is evaluated 6.5 nm below the ABS, i.e., at the center of the soft region of the media.

Fig. 6.7 shows the perpendicular component of the head field along the center of the staggered track where the maximum field strength is calculated as 12.0 kOe. Owing to the unusual angular dependence of the ECC media [6.2], the optimization focuses on the perpendicular field component. It is worth noting that the down track field has significantly larger gradient than that along the cross track since the staggered writing requires much steeper field along the down track to reduce writing errors. Fig. 6.8 shows the perpendicular field gradient profile for 4 nm fly height. The down track

perpendicular field gradient peaks at 596 Oe/nm with 8.5 kOe field amplitude while the maximum cross track perpendicular field gradient is 460 Oe/nm at 9.7 kOe.

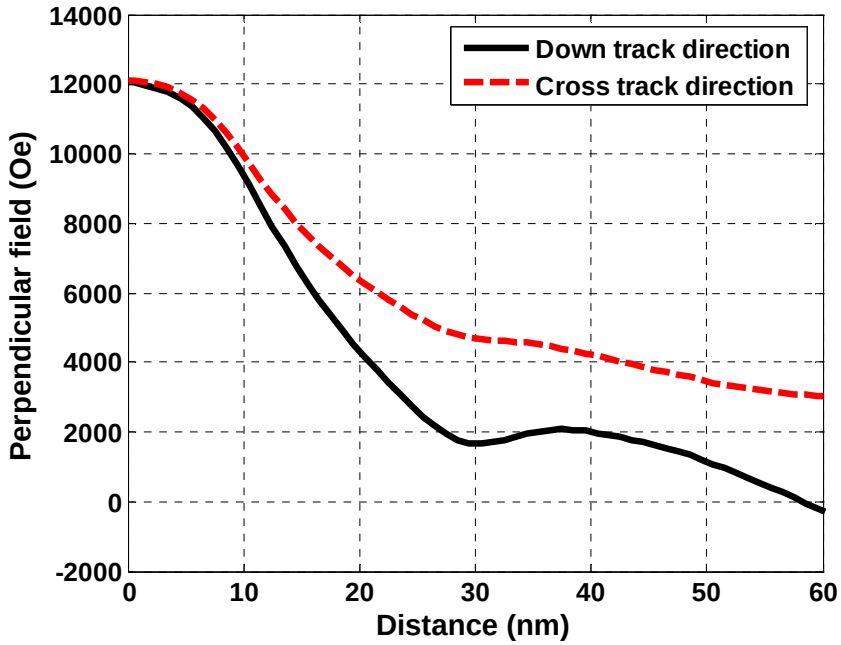

Figure 6. 7 Perpendicular field profiles along the staggered track and cross track directions.

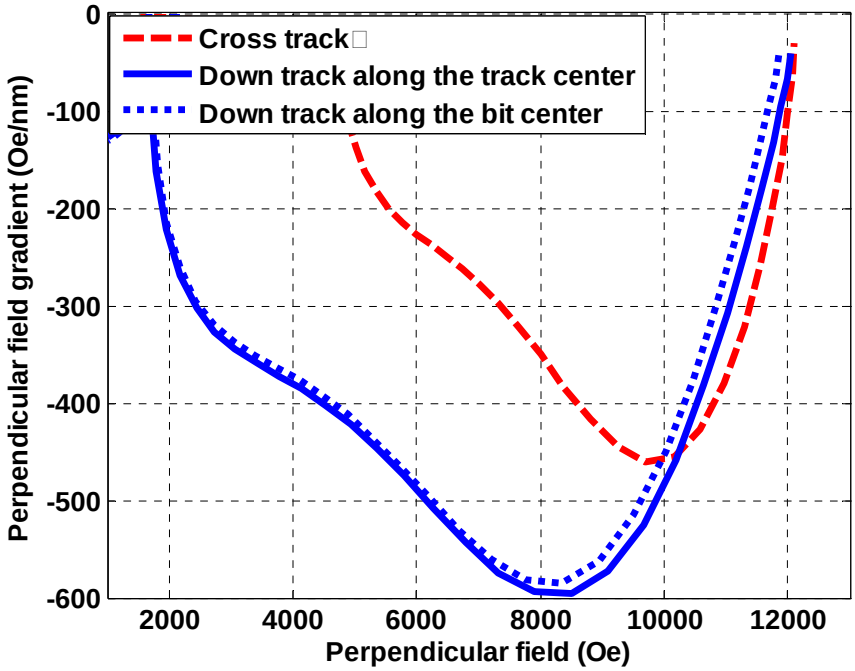

Figure 6. 8 Perpendicular field gradient profiles along the down track and cross track directions.

Fig. 6.6 shows single-domain islands of 8.1 nm× 8.1 nm× 10 nm are located on a hexagonal lattice of 16.2 nm period with 28% filling factor and with film saturation magnetization of 260 emu/cm^3. It also shows the geometry of the head design (in solid and dashed lines) at the air bearing surface. Following the same method as introduced in Section III of ref. 2, the effectiveness of the side shields is analyzed in terms of the stray field from the side tracks and their effect on the magnetization pattern in the shields and the tip. Considering dot #2 to be currently written and dot #1 as previously written, the nearest side tracks and a few islands on the current track are not effectively shielded. The stray field from these bits, which should be considered random, will disturb the head field applied to the currently written bit and be the dominant contribution to the demagnetizing field distribution.

Fig. 6.9 shows the histogram for the demagnetizing field acting on a dot. The maximum demagnetizing field produced by the nearest side tracks and the on-track dots further away is about 750 Oe and the standard deviation σ_{Hd} is about 264 Oe. It is found that it is justified to approximate the demagnetizing field distribution as a Gaussian.

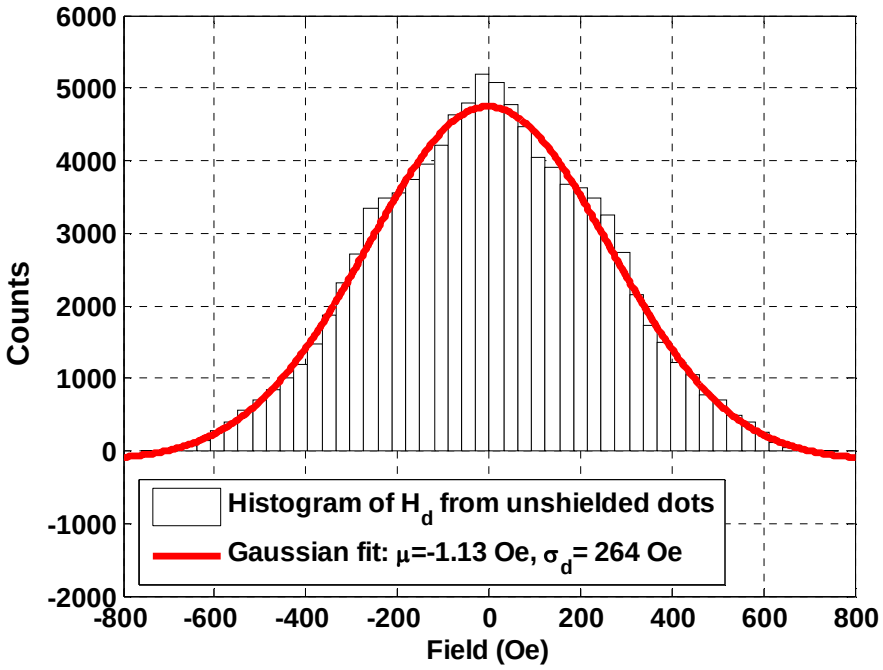

Figure 6. 9 An example for a histogram for the distribution of the demagnetizing fields acting on an 8.1 nm×8.1 nm bit.

Given the same head field distribution, it is necessary to define the average switching field as well as the location of writing window, and estimate the achievable areal density. We confine ourselves to four different sources of noise that are assumed random and uncorrelated: ΔW is defined as the width of writing window, the timing error $\sigma_{x,t}/\Delta W$ due to writing synchronization error is set to 5%, $\sigma_{x,j}/\Delta W$ the jitter error due to the down track dot spacing and dot size variance is 5% and the switching field distribution (σ_{Hsw}/H_{sw}) is 5%. The dot M_s is set to 900 emu/cm^3, implying film Ms of 260 emu/cm^3. The demagnetizing field distribution is about 264 Oe. All these disturbances can be considered as uncorrelated Gaussian distributed, with a variance of σ^2. In addition, the variance of the writing position due to the timing and jitter error can also lead to a field variance acting on the targeted dot from the chain law as shown in eqn. (6.2).

From the average value and variance of the applied field within the writing window zone, one can find the writing error by integration via

$$P_W = P_{W1} + \sum_{i=1,\ldots,n} P_{OWi} = erf\left(\frac{\Delta H_1}{\sqrt{2}\sigma_{H1}}\right) + \sum_{i=1,\ldots,n} erf\left(\frac{\Delta H_i}{\sqrt{2}\sigma_{Hi}}\right) \qquad (6.7)$$

where *erf* is the error function, ΔH_1 is the field range acting on the currently written dot #1 with a combined field variance of σ_{H1} and ΔH_i is the field range acting on the nearest neighboring dot #i with a combined field variance of σ_{Hi}. Here, the writing errors include failure of writing the current bit with P_{w1} probability, as well as overwriting of any nearest neighboring dots from the adjacent tracks and previously written bit from the current track with probability P_{owi}.

In addition to writing error, we also need to make sure that ATE field is greater than the maximum side field induced by the side shields. The fringe field that will cause adjacent track erasure (ATE) is determined by eqn. (6.1) based on the criteria that, the acceptable magnetization decay ratio per bit is 10^{-3} after 10^3 writer passes with a writer

speed of 30 m/s. Using a thermal stability ratio of 2.61 for the average switching field of 8.3 kOe, the calculated adjacent track erasure field is about 6.3 kOe which defines the minimum dot size of 8.1 nm from the head field profile. Solving eqn. (6.7) for this dot size yields 2.9 Tbits/in^2 with BER of 9.7×10^{-4}.

6. 6 Conclusion

Micromagnetically optimized specifications including 3D write head and ECC based bit pattern media are proposed for 4 Tbit/in^2 recording. We utilize a tapered neck main pole, side shields and trailing shield that have optimized tapered angles, sizes and gaps in order to generate a sufficiently large field and gradient to obtain acceptable BER. We summarize the dependence of bit error rate and bit aspect ratio on fly height, media thickness and thermal stability ratio of the media. We achieve 4 Tbit/in^2 areal density with a fly height of 4 nm or 5 nm, 10 nm media thickness and 2 nm seed layer thickness. Assuming 5% anisotropy field distribution, 5% timing error and 5% jitter error, the lowest estimated BER is 2.7×10^{-4}. A new design including exchange coupled composite (ECC) in hexagonal arrays and a multi-pole write head is proposed to meet the requirement of 9.7×10^{-4} bit error rate, 4 nm fly height, 5% switching field distribution, 5% synchronization error, and 5% jitter error to achieve 2.9 Tbits/in^2 bit-patterned recording. For recording self-assembled bit-patterned media, the head design writes two staggered tracks in a single pass and has maximum perpendicular field gradients of 580 Oe/nm along the down-track direction and 476 Oe/nm along the cross-track direction. The geometry demanded by self-assembly reduces recording density to 2.9 Tbits/in^2.

Summary

In this thesis, micromagnetic models are deployed to study the magnetic properties of perpendicular recording media. Micromagnetic studies are performed to verify the writability improvement in the media with hybrid soft underlayer, to understand the media noise plateau, to develop a technique for extracting intergranular exchange, and to optimize head-and-media design for 4 Tbit/in^2 bit patterned magnetic recording. In these models, statistical fluctuations of intrinsic anisotropy field, exchange interaction and magnetostatic interaction, as well as dimensional non-uniformities of the media are taken into realistic consideration.

Perpendicular recording media with a hybrid soft underlayer are particularly suitable for composite media and have potential use in the future. Micromagnetic simulation demonstrated that the hybrid soft underlayer scheme helps to improve writing field effectiveness and to increase field gradients. The media structure provides flexibility to improve texture growth and writability simultaneously.

A notable result from studying media noise is that, in perpendicular magnetic recording, the puzzling medium noise plateau over a range of intermediate recording densities is at least partly attributed to non-linear transition shift producing a positive jitter correlation. This is unlike longitudinal recording where a negative jitter correlation leads to a super-linear noise region. It is further shown that the observed effect is consistent with expected magnetostatic interactions.

Intergranular exchange coupling and intrinsic anisotropy field dispersion can be extracted from measuring two types of M-H curves. This characterization method is simple and effective for VSM measurement. It is found that the effects of exchange J_{ex} and σ_{Hk} on the slopes of two types of M-H curves are different but more importantly, correlated.

For rectangular array bit patterned media recording, we achieve 4 Tbit/in^2 areal density with a fly height of 4 nm or 5 nm, 10 nm media thickness and 2 nm seed layer thickness. Assuming 5% anisotropy field distribution, 5% timing error and 5% jitter error, the lowest estimated BER is 2.7×10^{-4}. For hexagonal arrays where two staggered

tracks are written in a single head pass, 2.9 Tbit/in^2 recording density can be achieved to meet the requirement of 1.0×10^{-3} BER, 5% anisotropy field distribution, 5% timing error and 5% jitter error.

References

[1.1] Source: http://rondennison.com/services.htm

[1.2] Source: http://en.wikipedia.org/wiki/hard_disk_drive

[1.3] G. Choe et al., "Highly in-plane oriented CoCrPtB longitudinal media for 130 Gb/in^2 recording", *IEEE Trans. Magn*. **39**, 633 (2003).

[1.4] B. R. Acharya et al., "Anti-parallel coupled soft under layers for high-density perpendicular recroding", *IEEE Trans. Magn*. **40**, 2383 (2004).

[1.5] M. Mallary, A. Torabi and M. Benakli, "One terabit per square inch perpendicular recording concept design", *IEEE Trans. Magn*. 38, 1719 (2002).

[1.6] H. Yamane, S. Watanabe, J. Ariake, N. Honda, K. Ouchi, and S. Iwasaki," Effect of oxygen on magnetic properties of Co–Pt–Cr–SiO2 thin films for perpendicular recording media", *J. Magn. Magn. Mater*. 287, 153 (2004).

[1.7] M. Zheng et al., "SNR improvement of granular perpendicular recording media", *IEEE Trans. Magn*. 39, 1919 (2003).

[1.8] H, J. Richter et al., "Recording on Bit-patterned media at densities of 1 Tb/in2 and beyond", *IEEE Trans. Magn*. 42, 2255 (2006).

[1.9] R. H. Victora and X. Shen, "Exchange coupled composite media for perpendicular magnetic recording", *IEEE Trans. Magn*., 41, 2828 (2005).

[1.10] R. E. Rottmayer et al., "Heat-assisted magnetic recording", IEEE Trans. Magn., 42, 2417 (2006).

[1.11] Jian-Gang Zhu, X. Zhu and Y. Tang, "Microwave assisted magnetic recording", *IEEE Trans. Magn*., 44, 125 (2008).

[1.12] R. Wood , M. Williams , J. Kavcic and J. Miles "The feasibility of magnetic recording at 10 terabits per square inch on conventional media", *IEEE Trans. Magn.*, 44, 917 (2009).

[1.13] Roger Wood, "The feasibility of magnetic recording at 1 Terabit per square inch", IEEE Trans. Magn., 36, 26 (2001).

[1.14] X. Shen, S. Hernandez and R.H. Victora, "Feasibility of recording 1Tb/in^2 areal density", *IEEE Trans. Magn.*, 44, 163 (2008).

[1.15] Y. Dong and R. H. Victora, "Micromagnetic Specifications for bit patterned recording at 4Tbit/in^2", to appear in *IEEE Trans. Magn*. 2011.

[1.16] M. A. Seigler et al., "Integrated head assisted magnetic recording head: design and recording demonstration", *IEEE Trans. Magn*., 44, 119 (2008).

[1.17] B. C. Stipe et al., "Magnetic recording at 1.5 Pbm^{-2} using an integrated plasmonic antenna", *Nature Photonics* 4, 484 (2010).

[1.18] S. Greaves et al., "Shingled recording for 2-3 Tbit/in^2", *IEEE Trans. Magn*., 45, 3823 (2009).

[1.19] J. Mallinson, "On extremely high density magnetic recording," *IEEE Trans. Magn.*, MAG-10, 368 (1974).

[1.20] J. Hoinville, R. Indeck, and M. Muller, "Spatial noise phenomena of longitudinal magnetic recording media," *IEEE Trans. Magn*., 28, 3398 (1992).

[1.21] B. Slutsky and H. N. Bertram, "Transition noise analysis of thin film magnetic recording media," *IEEE Trans. Magn*., 36, 2808 (1994).

[1.22] H. N. Bertram, Theory of Magnetic Recording. Cambridge, U.K.: Cambridge Univ. Press, 1994.

[1.23] S.Iwasaki and Y.Nakamura, "An analysis for the Magnetization Mode for High Density Magnetic Recording", *IEEE. Trans. Magn.*, 13 , 1272 (1977).

[1.24] S.Iwasaki, K.Ouchi and N.Honda, "Studies of the Perpendicular Magnetization Mode in Co-Cr Sputtered Films", *IEEE Trans. Magn*., 16, 1111 (1980).

[1.25] T. Shimatsu et al., "Thermal agitation of magnetization in CoCrPt perpendicular recording media", *IEEE Trans. Magn*., 37, 1567 (2001).

[1.26] T. Oikawa et al., "Microstructure and magnetic properties of CoPtCr-SiO_2 perpendicular recording media", *IEEE Trans. Magn*., 38, 1976 (2002).

[1.27] D. Welle et al., "High K materials approach to 100 Gbits/in^2", *IEEE Trans. Magn*. 36, 10 (2000).

[1.28] S. H. Liou et al., "Enhancement of coercivity in nanometer-size CoPt crystallites", *J. Appl. Phys*. 85, 4334 (1999).

[1.29] S. N. Piramanayagam et al., "Grain size reduction in CoCrPt:SiO_2 perpendicular recording media with oxide-based intermediate layers", *Appl. Phys. Lett*., 89, 162504 (2006).

[1.30] C. Chang et al., "CoCrPt-oxide based perpendicular recording media with hybrid soft magnetic underlayers", *J. Appl. Phys.*, 104, 103905 (2008).

[1.31] B. R. Acharya et al., "Anti-parallel coupled soft under layers for high-density perpendicular recording", *IEEE Tran. Magn.*, 40, 2383 (2004).

[1.32] J. Z. Shi et al., "Influence of dual-Ru intermediate layers on magnetic properties and recording performance of CoCrPt–SiO_2 perpendicular recording media," *Appl. Phys. Lett.*, vol. 87, 222503 (2005).

[1.33] Y. Uesaka et al., "Noise from underlayer of perpendicular magnetic recording medium", *J. Appl. Phys.* 57, 3925 (1985).

[1.34] Yukio Honda et al., "Effect of soft magnetic underlayer on magnetization microstructure of perpendicular thin film media", *IEEE Trans. Magn*., 36, 2399 (2000).

[1.35] T. Hikosaka et al., "Low noise FeAlSi soft magnetic under-Layer for CoPtCrO double-layered perpendicular recording media", *IEEE Trans. Magn*., 37, 1586 (2001).

[1.36] T. Ando et al., "Exchanged-coupled CoZrNb/CoSm underlayer for perpendicular recording media", *IEEE Trans. Magn*., 37, 1228 (2001).

[1.37] H. S. Jung and W. D. Doyle., "High-moment FeCo-IrMn exchange-coupled soft underlayers for perpendicular media", *IEEE Trans. Magn*., 39, 679 (2003).

[1.38] Kai-Zhong Gao and H. Neal Bertram, "Write field analysis and write pole deisgn in perpendicular recording", *IEEE Trans. Magn*., 38, 3521 (2002).

[1.39] M. S. Patwari and R. H. Victora, "Simulation of erasure after write on 2.4 T FeCo solid pole writer", IEEE Trans. Magn., 46, 1212 (2010).

[1.40] Baibich et al., "Giant magnetoresistance of (001) Fe/(001) Cr magnetic superlattices", *Phys. Rev. Lett*. 61, 2472 (1988).

[1.41] H. Oshima et al., “Current-perpendicular spin valves with partially oxidized magnetic layers for ultrahigh-density magnetic recording”, *IEEE Trans. Magn*. 39, 2377 (2003).

[1.42] R. Rottmayer and J. Zhu, “A new design for an ultra-high density magnetic recording head using a GMR sensor in the CPP mode”, *IEEE Trans. Magn*. 31, No. 6, 2597 (1995).

[1.43] Julliere, M. “Tunneling between ferromagnetic films”, *Phys. Lett. A* 54, 225 (1975).

[1.44] Moodera, J. S., Kinder, L. R., Wong, T. M. and Meservey, R. “large magnetoresistance at room temperature in ferromagnetic thin film tunnel junctions”, *Phys. Rev. Lett*. 74, 3274 (1995).

[1.45] Stuart S. P. Parkin et al., “Giant tunneling magnetoresistance at room temperature with MgO(001) tunnel barriers, Nature Materials, Vol. 3, 862 (2004).

[1.46] S. Mao et al., “Commercial TMR heads for hard disk drives: characterization and extendibility at 300 Gbit/in^2”, *IEEE Trans. Magn*., 42, 97 (2006).

[1.47] S.N. Piramanayagam, J.Z. Shi, H.B. Zhao, C.S. Mah, J.R. Shi, J.M. Zhao, J. Zhang and Y.S. Kay, “Novel approaches to high-density perpendicular recording media,” *J. Magn. Magn. Mater.* 303, 287 (2006).

[1.48] S. N. Piramanayagam, C. K. Pock, L. Li, C. Y. Ong, C. S. Mah, and J. Z. Shi, “Advanced perpendicular recording media structure with a magnetic intermediate layer,” *Appl. Phys. Lett.,* 89, 162504 (2006).

[1.49] J.Z. Shi, S.N. Piramanayagam, S.Y. Chow, J.M. Zhao and C.S. Mah, “CoCrPt-SiO_2 perpendicular recording media with a crystalline soft underlayer,” *IEEE Trans. Magn.,* 42, 2369 (2006).

[1.50] S. N. Piramanayagam et al., “CoCrPt-oxide based perpendicular recording media with hybrid soft magnetic underlayers”, J. App. Phys., 104, 103905 (2008).

[1.51] R. H. Victora and X. Shen, “Composite media for perpendicular magnetic recording”, *IEEE Trans. Magn*., 41, 537 (2005).

[1.52] J. Wang et al., “Exchange coupled composite media for perpendicular magnetic recording”, IEEE Trans. Magn., 41, 3181 (2005).

[1.53] Stephanie Hernandez, Manish Kapoor and R. H. Victora, *Appl. Phys. Lett.* 90, 132505 (2007).

[1.54] X. Shen et al., “Feasibility of recording 1 Tb/in2 areal density”, *IEEE Trans. Magn.*, 44, 163 (2008).

[1.55] M. A. Siegler et al., “Integrated head assisted magnetic recording head: densign and recording demonstration”, IEEE Trans. Magn., 44, 119 (2008).

[1.56] W. A. Challener et al., “Heat-assisted magnetic recording by a near-field transducer with efficient optical energy transfer”, Nature Photonics, 3, 220 (2009).

[1.57] T. Rausch et al., “Near field heat assisted magnetic recording with a planar solid immersion lens”, *Jpn. J. Appl. Phys*., 45, 1314 (2006).

[1.58] H. J. Richter et. al., “Recording in Bit-Patterned Media at Densities of 1Tb/in2 and Beyond,” *IEEE Trans. Magn*., 42, 2255 (2006).

[1.59] S. O. Lim et al., “Epitaxial self-assembly of block copolymers on lithographically defined nanopatterned substrates”, Nature 424, 411 (2003).

[1.60] R. Rui et al., “Density multiplication and improved lithography by directed block copolymer assembly”, Science 321, 936 (2008).

[2.1] William Fuller Brown, Micromagnetics, John Wiley & Sons, Inc. 1963

[2.2] R. H. Victora, Jianhua Xue, and Mohammed Patwari, IEEE Trans. Magn., 38, No.5, 2002.

[2.3] Y. Peng, J. Zhu and D. E. Laughlin, J. Appl. Phys. 99, 08F907, 2006.

[2.4] R.W. Chantrell, K.M. Tako, M. Wongsam, N. Walmsley, and T. Schrefl, J. Magn. Magn. Mater. 175 (1997) 137-147.

[2.5] Robert C. O’Handley, Modern Magnetic Materials – Principles and Applications, John Wiley & Sons, Inc. 2000

[2.6] G.A. Mohr, Finite Elements for Solids, Fluids and Optimization, Oxford University Press, 1992

[2.7] B. Bradie, A Friendly Introduction to Numerical Analysis, Pearson Prentice Hall, 2006.

[2.8] M. E. Schabes and A. Aharoni, IEEE Tran. Magn., Vol, Mag-23, No. 6, 1987.

[2.9] B.D. Cullity, Introduction to magnetic materials, Addison-Wesley Publishing Company, Inc. 1972.

[2.10] A. Aharoni, Introduction to the theory of ferromagnetism, 2nd ed., Oxford University Press Inc., New York, 2000

[2.11] W. F. Brown, JR., "Thermal fluctuations of a single-domain particle", Phys. Rev. Vol. 130, No.5, 1677-1686, 1963.

[3.1] D. Litvinov, M.H Kryder and S. Khizroev, "Recording physics of perpendicular media: hard layers," *J. Magn. Magn. Mater.*, 241, pp. 453-465, 2001.

[3.2] C. Chang, M. Plumer, and et al., "Measurements and modeling of soft underlayer materials for perpendicular magnetic recording," *IEEE Trans. Magn.*, vol. 38, pp. 1637-1642, 2002.

[3.3] S. Khizroev, D. Litvinov, "Perpendicular magnetic recording: Writing process," *J. Appl. Phys.* vol. 95, pp. 4521-4537, 2004.

[3.4] S. Khizroev, Y. Liu, K. Mountfield, M. Kryder, D. Litvinov, "Physics of perpendicular magnetic recording: writing process," *J. Magn. Magn. Mater.*, vol. 246, pp. 335-344, 2002.

[3.5] S.N. Piramanayagam, J.Z. Shi, H.B. Zhao, C.S. Mah, J.R. Shi, J.M. Zhao, J. Zhang and Y.S. Kay, "Novel approaches to high-density perpendicular recording media," *J. Magn. Magn. Mater.* vol. 303, pp. 287 -291, 2006.

[3.6] S. N. Piramanayagam, H.B. Zhao, J. Z. Shi and C.S. Mah, "Advanced perpendicular recording media structure with a magnetic intermediate layer," *Appl. Phys. Lett.* vol. 88, *092501*, 2006.

[3.7] J.Z. Shi, S.N. Piramanayagam, S.Y. Chow, J.M. Zhao and C.S. Mah, "CoCrPt-SiO_2 perpendicular recording media with a crystalline soft underlayer," *IEEE Trans. Magn.* vol. 42, pp. 2369-2371, 2006.

[3.8] S. N. Piramanayagam, "Perpendicular recording media for hard disk drives," *J. Appl. Phys.*, vol. 102, 011301, 2007.

[3.9] T. Keitoku, J. Ariake, N. Honda, “Preparation condition of Co-Pt-Cr-SiO2 films with high coercivity,” *J. Magn. Magn. Mater.*, vol. 287, pp. 172-175, 2005.

[3.10] Y. Honda, K, Tanahashi, Y. Hirayama, A. Kikukawa, and M. Futamoto, “Observation of magnetic interaction between the soft magnetic and the recording layers in double-layer perpendicular media,” *IEEE Trans. Magn.*, vol. 37, pp. 1315-1318, 2001.

[3.11] J. Z. Shi, S. N. Piramanayagam, C. S. Mah, H. B. Zhao, J. M. Zhao, Y. S. Kay, and C. K. Pock, “Influence of dual-Ru intermediate layers on magnetic properties and recording performance of CoCrPt–SiO perpendicular recording media,” *Appl. Phys. Lett.*, vol. 87, 222503, 2005.

[4.1] J. Hoinville, R. Indeck, and M. Muller, “Spatial noise phenomena of longitudinal magnetic recording media,” *IEEE Trans. Magn.*, vol. 28, no. 6, pp. 3398–3406, Nov. 1992.

[4.2] B. Slutsky and H. N. Bertram, “Transition noise analysis of thin film magnetic recording media,” *IEEE Trans. Magn.*, vol. 36, no. 5, pp. 2808–2817, Sep. 1994.

[4.3] N. Belk, P. George, and G. Mowry, “Noise in high performance thin-film longitudinal magnetic recording media,” *IEEE Trans. Magn.*, vol. MAG-21, pp. 1350-1355, May. 1985.

[4.4] M. Madrid and R. Wood, “Transition noise in thin-film media,” *IEEE Trans. Magn.*, vol. MAG-22, pp. 892-894, Sep. 1986.

[4.5] K. Senanan and R. H. Victora, “Theoretical study of nonlinear transition shift in double-layer perpendicular recording,” *IEEE Trans. Magn.*, vol. 38, no. 4, pp. 1664-1669, Jul. 2002.

[4.6] J. Chen et al., “Effect of reader saturation on the measurement of NLTS in perpendicular recording”, *J. Appl. Phys.*, vol. 93, no. 10, 6534-6536, May. 2003.

[4.7] H. Muraoka et al., “Nonlinear transition shift measurement in perpendicular magnetic recording,” *IEEE Trans. Magn.*, vol. 32, no. 4, pp. 3926-3928, Sep. 1996.

[4.8] J. Xue and R. H. Victora, “Micromagnetic calculation for superlattice magnetic recording media,” *Appl. Phys. Lett.* 77, vol. 87, no. 9, pp. 6361-6363, May. 2000.

[4.9] H. N. Bertram, Theory of Magnetic Recording. Cambridge, U.K.: Cambridge Univ. Press, 1994.

[4.10] R. H. Victora, W. Peng, J. Xue and J. H. Judy, “Superlattice magnetic recording media: Experiment and simulation,” *J. Magn. Magn. Mater.* , vol. 235, pp. 305-311, Oct. 2001.

[5.1] R. Araki, Y. Takahashi, I. Takekuma, and S. Narishige, IEEE Trans. Magn. **44**, 3496, 2008.

[5.2] Tamai, R. Araki, and K. Tanahashi, IEEE Trans. Magn. 44, 3492, 2008.

[5.3] Tagawa and Y. Nakamura, “Relationship between high density recording performance and particle coercivity distribution”, *IEEE Trans. Magn*., 27, 4975-4977, (1991).

[5.4] A. Berger et. al., “ΔH (M, ΔM) method for the determination of intrinsic switching field distributions in perpendicular media”, *IEEE Trans. Magn*., 41, 3178-3180, (2005).

[5.5] M. Winklhofer and G.T. Zimanyi, “Extracting the intrinsic switching field distribution in perpendicular media: A comparative analysis”, *J. Appl. Phys*. 99, 08E710, (2006).

[5.6] E. Yuan and R.H. Victora, “Characterization of anisotropy field dispersion in perpendicular media”, *IEEE Trans. Magn*., 40, 2452-2454, (2004).

[5.7] J. Xue and R. H. Victora, “Micromagnetic predictions for thermally assisted reversal over long time scales”, Appl. Phys. Lett, 77, 3432-3434, (2000).

[5.8] R. H. Victora, W. Peng, J. Xue and J. H. Judy, “Superlattice magnetic recording media: Experiment and simulation”, *J. Magn. Magn. Mater.* , vol. 235, 305-311, (2001).

[5.9] D. Weller and A. Moser, “Thermal effect limits in ultrahigh density magnetic recording”, *IEEE Tran. Mag.*, Vol. 35, No. 6, 4423-4439, 1999.

[5.10] L. Néel, “Theorie du trainage magnetique des ferromagnetiques en grains fins avec applications aux terres cuites,” *Ann. Geophys.*, vol. 5, pp. 99-136, 1949.

[6.1] H. J. Richter et. al., “Recording in Bit-Patterned Media at Densities of 1 Tb/in^2 and Beyond,” *IEEE Trans. Magn.*, vol. 42, no. 10, pp. 2255-2260, Oct. 2006.

[6.2] X. Shen, S. Hernandez and R. H. Victora, “Feasibility of Recording 1 Tb/in^2 Areal Density,” *IEEE Trans. Magn.*, vol. 44, no. 1, pp. 163-168, Jan. 2008.

[6.3] X. Shen, M. Kapoor, R. Field and R. H. Victora, “Issues in Recording exchang coupled composite media”, *IEEE Trans. Magn.*, vol. 43, no. 2, pp. 676-681, Feb. 2007.

[6.4] M. Albrecht, A. Moser, C. T. Rettner, A. Anders, T. Thomson, and B. D. Terris, “Recording performance on high-density patterned perpendicular media,” *Appl. Phys. Lett*., vol. 80, pp. 3409–3411, May 2002.

[6.5] P. W. Nutter, I. T. Ntokas, and B. K. Middleton, “An investigation of the effects of media characteristics on read channel performance for patterned media storage,” *IEEE Trans. Magn*., vol. 41, no. 11, pp. 4327–4334, Nov. 2005.

[6.6] X. Yang, S. Xiao, W. Wu, Y. Xu, K. Mountfield, R. Rottmayer, K. Lee, D. Kuo and D. Weller, J. Vac. Sci. Technol. B, 25, 2202 (2007).

[6.7] R. Ruiz, H. Kang, F. A. Detcheverry, E. Dobisz, D. S. Kercher, T. R. Albrecht, J. J. de Pablo, and P. F. Nealey, Science **321**, 2008.

[6.8] O. Hellwig and et. al., Appl. Phys. Lett. **96**, 052511 (2010).